Optoelectronic Phenomena Induced by Terahertz/Infrared Laser Radiation in Topological Insulators and Graphene

Dissertation

zur Erlangung des Doktorgrades
der Naturwissenschaften (Dr. rer. nat.)
der Fakultät Physik
der Universität Regensburg

vorgelegt von

Helene Plank

aus Burghausen

im Jahr 2018

Promotionsgesuch eingereicht am: 17.01.2018

Die Arbeit wurde angeleitet von: Prof. Dr. Sergey D. Ganichev

Prüfungsauschuss

Vorsitzender: Prof. Dr. Klaus Richter
1. Gutachter: Prof. Dr. Sergey D. Ganichev
2. Gutachter: Prof. Dr. Tobias Korn
weiterer Prüfer: Prof. Dr. Josef Zweck

Contents

1 Introduction

The realization of graphene [1] was the starting point for a new 'era' in condensed matter physics. This first truly two dimensional material hosts massless relativistic particles [2, 3]. Not only its unique and novel properties created a stir, also its easy in comparison to conventional semiconductors fabrication technique allowed many scientists to manufacture it on their own. Graphene inspired the realization of other two dimensional materials and the possibility of stacking different monolayers provides a new toolbox to design and modify material properties [4]. Furthermore, graphene was the first material proposed to demonstrate the quantum spin Hall effect (QSHE) [5]. Although this non-trivial property of graphene is, due to a too weak spin orbit interaction (SOI), effectively not observable, the work by Kane and Mele lead to a second avalanche in the condensed matter community and was the starting point for the physics of topological insulators [6–9].

Topology, as a class to characterize various systems, was already used in 1988 by Haldane [10] for the quantum Hall effect (QHE) [11]. The QHE describes insulating 2D system with conducting edge channels for broken time reversal symmetry and is classified by the $\mathbb{Z}$ invariant [6]. In the QHE the bulk dispersion is quantized and for the Fermi energy lying between two Landau levels, all conducting carriers reside in *chiral* edge channels [12]. These channels are unidirectional and perfectly quantized in conductance values $2e^2/h$ and their transport is dissipationless since no state for backscattering is present [6].

Another class of topology in condensed matter is described by the $\mathbb{Z}_2$ invariant. To this class belongs, e.g. the quantum spin Hall effect [13, 14]. It describes bound states with linear dispersion at the interface between regions with trivial and non-trivial band structure, i.e. an inverted band ordering described by a negative energy band gap [8, 15]. In these bound states counter propagating carriers along the edge have opposite spin and are called *helical* [6]. Systems which exhibit these states are called two dimensional topological insulators (2D TIs) and the first materials where the QSHE was observed were mercury telluride quantum wells [16, 17]. This concept can be extended to three dimensions, still classified by the $\mathbb{Z}_2$ invariant [18]. In 3D TIs conducting surface states with linear dispersion enclose the insulating non-trivial bulk. In the surface states, single spin states are locked to the momentum and the spin rotates its direction when moving around the Fermi surface [19]. Soon after their prediction, possible materials were proposed [20] and one prominent

family that has been realized is Bi_2Te_3, Sb_2Te_3 and Bi_2Se_3 3D TIs [21].

Both graphene and 3D TIs host relativistic 2D Dirac fermions, which are described by the zero mass Dirac equation [22]. They are often probed by transport experiments [3], with which one can studied the quantum Hall effect [1, 23, 24] or quantum interference experiments like weak localization or anti-localization [2, 25] or the Aharonov-Bohm effect [26, 27]. Furthermore, they are investigated with optical methods, e.g. with photoemission spectroscopy. One can gain insight in the band structure below the Fermi level with angle resolved photoemission spectroscopy (ARPES) [28–34] or above it with two-photon photoelectron (2PPE) spectroscopy [35–37].

It has been demonstrated that the combination of both techniques, summarized under the term nonlinear optoelectronic phenomena, allows insight into microscopic processes [38], and that with it an access to TIs [39] and graphene [40] is possible. This thesis concentrates on terahertz radiation induced photocurrents in graphene and Bi_2Te_3- and Sb_2Te_3-based 3D TIs.

It was shown, that photocurrents in Bi_2Se_3 are induced with near infrared, circularly polarized radiation [41–43]. Here it is demonstrated, that in Bi_2Te_3- and Sb_2Te_3-based 3D TIs such an access is also possible with linear polarized radiation and frequencies in the terahertz range. Furthermore, the study shows, that the photogalvanic effect is used to overcome a well-known problem of systems, namely the presence of a conducting bulk parallel to the surface states, which complicates classical transport. Due to a symmetry filtration between the centrosymmetric bulk and the non-centrosymmetric surface state, the selective excitation of Dirac fermions at room temperature and the study of their high frequency transport is possible [44]. Measuring the terahertz radiation induced photocurrents in a wide range of frequencies has major advantages. First, it allows the estimation of room temperature scattering times and mobilities, and second, it gives insight in optical transitions [45]. In the frequency range in which the photoionization of surface carriers into the bulk bands is possible, photocurrent being sensitive to the radiation helicity are detected [45]. A spatially selective excitation allows a characterization of the material properties by mapping the high frequency transport locally. Furthermore, the local domain orientation and presence of twisted domains can be found out [46]. Besides this, it is shown that a trigonal photon drag effect can be observed under certain experimental conditions [47].

The study of systems with linear dispersion is extended to high mobility graphene. Nonlinear optoelectronic phenomena in graphene build a solid basis

for this study [40]. In this thesis the focus lies on the excitation of carriers in chiral edge channels for graphene being in the quantum Hall regime. It is shown that the terahertz radiation induced photocurrents are solely determined by the magnetic field. This is demonstrated by comparing them to edge currents at zero magnetic field, which are set by the radiation electric field vector and the carrier type.

The thesis is organized as follows: In Chap. 2 the fundamental principles are introduced. It starts in Sec. 2.1 with the Dirac equation. On the basis of graphene and 3D TIs its implementation in condensed matter for the zero mass limit is shown. For both materials a similar approach is used: First the crystalline structure is shown, and based on this the electronic structure is introduced. At the end of each subsection the focus lies on the region in the band structure where the dispersion is linear. Although, both systems are characterized by a linear dispersion, they have different properties. While the Dirac cone in graphene is spin degenerated and characterized by a pseudospin, which is linked to the K and K' valley, the Dirac cone in 3D TIs is non-degenerated and momentum and spin are locked. In Sec 2.2 nonlinear optoelectronic phenomena are introduced. It is shown that high frequent alternating electric fields, provided here by terahertz radiation, can cause a direct photocurrent. In the first subsection a phenomenological theory is introduced. In the following subsections 2.2.2 and 2.2.3 focus more specifically on the effects studied, namely the photogalvanic and the photon drag, respectively. In both subsections, the effect is introduced with an example and after an introduction of the phenomenological theory specific for the point group symmetry of the material, semi-classical models and theories are introduced, which help to follow the discussion in Chap. 4 and Chap.5. Chapter 3 introduces the methods used, starting in Sec. 3.1 with the investigated Bi_2Te_3- and Sb_2Te_3-based thin films, see Sec. 3.1.1, and high mobility graphene, see Sec. 3.1.2. The description of their fabrication is accompanied by methods for their characterization. Section 3.2 then describes the measurements technique. For the study of Bi_2Te_3- and Sb_2Te_3-based thin films a variety of lasers is used. Their basic concepts and operation modes are shortly described in Sec. 3.2.1. In Sec. 3.2.2 the experimental setup is explained. The experimental results on photocurrents generated in Bi_2Te_3- and Sb_2Te_3-based thin films and their discussion are presented in Chap. 4. Results obtained with linearly polarized terahertz radiation at normal, see Sec 4.1, and oblique, see Sec. 4.2, incidence are discussed first. The photocurrent in these two sections are treated semi-

classically, in contrast to Sec. 4.3, which presents photocurrents excited with the highest frequencies used and with circularly polarized radiation. Results obtained in high mobility graphene are shown and discussed in Chap. 5. The findings obtained ar zero magnetic field are presented and discussed in Sec. 5.1 and the one for graphene being in the quantum Hall regime in Sec. 5.2. The last chapter, Chap. 6 summarizes the work and gives an outlook to the field.

2 Fundamentals

In this chapter the fundamental principles required for this thesis are introduced. In the first section systems with linear dispersion, described by the zero mass Dirac equation, are presented. In the second section the concept of photocurrents is elaborated. It is shown that photocurrents, proportional to the squared electric field, provide understanding of microscopic material properties and are suitable to study Dirac fermion systems like graphene and Bi_2Te_3- and Sb_2Te_3-based thin films.

2.1 Dirac Fermions in Condensed Matter

The Dirac equation, written down in 1928 Paul Dirac [22], is a relativistic wave equation which describes massive particles with spin 1/2. It is a second order partial differential equation in time and space coordinates and is invariant under Lorentz transformation. Although originally constructed for free particles, the zero mass Dirac equation describes also systems in condensed matter with linear dispersion like graphene [1–3] or topological insulators [6, 9, 13].

This sections introduces first the Dirac equation, and given then two examples for systems with linear dispersions, graphene and Bi_2Te_3- and Sb_2Te_3-based three dimensional topological insulators (3D TIs), both being in the focus of this thesis. To understand the remarkable properties of those systems, it is crucial to first describe their crystallographic structure. From the latter the electronic structure is deduced using a tight-binding approach. The region in the band structure in which the dispersion in linear is then analysed in more detail.

2.1.1 The Dirac Equation

The Dirac equation [22, 48]

$$(i\hbar\gamma^\mu\partial_\mu - mc)\psi = 0 \tag{1}$$

contains the wave function ψ, the mass m, the speed of light c, and the momentum operator $\hat{p} = -i\hbar\partial_\mu$, in which $\hbar = h/2\pi$ is the reduced Plancks' constant and ∂_μ is the partial derivative with the summation index $\mu = 0, 1, 2, 3$, given in Einstein notation $\gamma^\mu\partial_\mu = \sum_{\mu=0}^{3}\gamma^\mu\partial_\mu$. The four 4×4 gamma ($\gamma$) matrices were used by Dirac to reduce the problem to a first order differential equation.

Using the Pauli matrices

$$\sigma_x = \begin{pmatrix} 0 & 1 \\ 1 & 0 \end{pmatrix}, \ \sigma_y = \begin{pmatrix} 0 & -i \\ i & 0 \end{pmatrix}, \ \sigma_z = \begin{pmatrix} 1 & 0 \\ 0 & -1 \end{pmatrix}, \tag{2}$$

the γ matrices are given as

$$\begin{aligned} \gamma^0 &= \begin{pmatrix} I & 0 \\ 0 & -I \end{pmatrix}, \ \gamma^1 = \begin{pmatrix} 0 & \sigma_x \\ -\sigma_x & 0 \end{pmatrix}, \\ \gamma^2 &= \begin{pmatrix} 0 & \sigma_y \\ -\sigma_y & 0 \end{pmatrix}, \ \gamma^3 = \begin{pmatrix} 0 & \sigma_z \\ -\sigma_z & 0 \end{pmatrix}, \end{aligned} \tag{3}$$

in which I is the 2×2 identity matrix. The Dirac equation can also be written in the form of a Schrödinger equation $\mathcal{H}\psi = i\frac{\partial\psi}{\partial t}$, where the corresponding Dirac Hamiltonian is given by [8, 49]

$$\mathcal{H} = \beta mc^2 + \alpha_n p_n c. \tag{4}$$

Here $\beta = \gamma^0$ and $\alpha_n = \gamma^n$ with $n = 1, 2, 3$. Solving the eigenvalue equation $\mathcal{H}\psi = \varepsilon\psi$ the solution

$$\varepsilon_\pm = \pm\sqrt{(mc^2)^2 + (pc)^2} \tag{5}$$

is found. The two solutions for positive energy ε_+ describe electrons with spin up respectively spin down. The two solutions for negative energy ε_- had predicted the anti-particle of the electron, the positron, whose existence was experimentally confirmed in 1933 [50]. In vacuum all negative energy states are completely filled (Dirac sea) [22] and for a single electron one state with positive energy is occupied. The positive and negative energy states are separated by an energy gap, given by $2mc^2$. This energy gap closes for the mass term going to zero and the remaining energy dispersion $\varepsilon(m \to 0) = \pm|cp|$ is linear in p and c. In this limit the Dirac equation reduced to $i\hbar\gamma^\mu\partial_\mu\psi = 0$, which is the Weyl equation [51].

This zero mass Dirac equation also describes systems in condensed matter like graphene or topological insulators.

2.1.2 Graphene

Graphene, a two dimensional monolayer of graphite, was experimentally realized in 2004 by Novoselov *et al.,* [1]. Its electronic structure however, was

already described in 1947 by Wallace [52]. In the following the crystalline and electronic structure of graphene is derived, with a focus on the linear dispersion.

Crystalline Structure A carbon atom has six electrons and four of them occupy the 1s and 2s orbitals with two electrons each. The p_x, p_y, and p_z orbitals of the $1p$ orbital are partially filled with the remaining two electrons. In graphene, a carbon monolayer is formed like a honeycomb structure, see Fig. 1 (a), with each carbon atom having three neighbouring atoms. Bonds with the three neighbouring carbon atoms are only possible, if the carbon atoms hybridize into $sp2$. This means that the $2s$ and $1p$ orbitals align in energy and share their four electrons equally, with one electron in each orbital. Then the $1p_x$, $1p_y$, and $2s$ orbitals form equivalent σ-bonds with the neighbouring carbon atoms and the remaining $1p_z$ orbitals form additional π-bonds [53]. These π-bonds form a double bonds with the σ-bonds and since different configurations are equivalent they are delocalised [54]. They stabilise the monolayer and form the π^* conduction and π valence band. A stack of graphene layers is called graphite and single monolayers are bound by van der Waals interaction [2]. The unit cell, see orange shaded region in Fig. 1 (a), has a two-atomic basis, denoted as A and B. The two sublattices are constructed with the lattice vectors [2]

$$\boldsymbol{a}_1 = \frac{a}{2}(\sqrt{3}, 1), \ \boldsymbol{a}_2 = \frac{a}{2}(\sqrt{3}, -1) \tag{6}$$

with a lattice constant $a = d\sqrt{3} = 2.46$ Å and a carbon(A)-carbon(B) distance of $d = 1.42$ Å. In momentum space, the first Brillouin zone (BZ) is hexagonal, see orange shaded region Fig. 1 (b). Points of high symmetry are the Γ point in the BZ centre, the M point in the middle of the BZ edge and the K and K' points at the corners of the BZ. The reciprocal lattices are described with the vectors

$$\boldsymbol{b}_1 = \frac{2\pi}{a}(1/\sqrt{3}, 1), \ \boldsymbol{b}_2 = \frac{2\pi}{a}(1/\sqrt{3}, -1). \tag{7}$$

Electronic Structure To understand the unique properties of graphene, the electronic structure is important. Since valence and conduction bands are

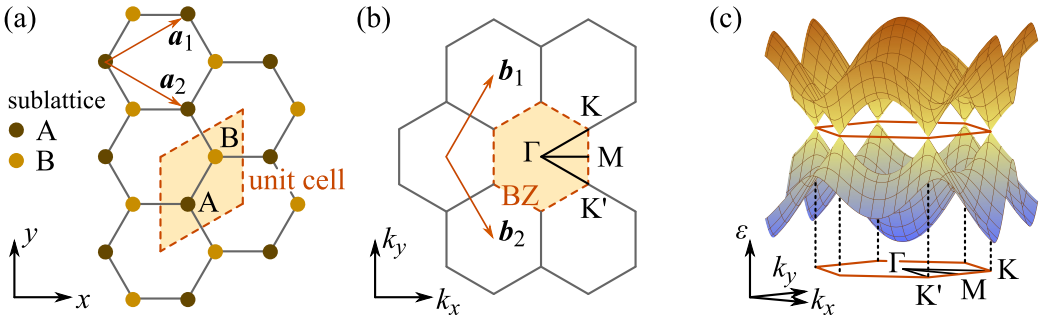

Figure 1: Crystallographic and electronic structure of graphene: (a) Honeycomb lattice in real space with two-atomic basis, A and B. The unit cell is shown as orange shaded area and lattice vectors are given by $\boldsymbol{a}_1$ and $\boldsymbol{a}_2$. (b) In momentum space, Brillouin zone is shown as orange shaded area, containing points of high symmetry Γ, M, K, and K'. The reciprocal lattice is constructed by vectors $\boldsymbol{b}_1$ and $\boldsymbol{b}_2$. (c) The electronic dispersion in first Brillouin zone is formed by delocalised π orbitals. At K and K' points conduction and valence bands touch. Adapted from Ref. [53].

formed by π-bonds, while the remaining electrons are tightly bound in the σ-bonds, a tight binding approach is suitable.

For a tight binding approach, Bloch's theorem is used to find a wave function ψ, which fulfils the Schrödinger equation with the tight binding Hamiltonian $\mathcal{H}$. The i-th eigenvalue [53, 55] is given for the wave vector $\boldsymbol{k}$ by

$$\varepsilon_i(\boldsymbol{k}) = \frac{\langle\psi_i|\mathcal{H}|\psi_i'\rangle}{\langle\psi_i|\psi_i'\rangle} \tag{8}$$

This contains the transfer matrix element $\mathcal{T} = \langle\psi_i|\mathcal{H}|\psi_i'\rangle$, which is a measure for the probability of electrons to hop from atom to atom, and the overlap matrix element $\mathcal{S} = \langle\psi_i|\psi_i'\rangle$, which is a measure for the overlap of Bloch wave functions in the π orbitals. For graphene the total number of possible matrix elements is restricted and the transfer $\mathcal{T}_{ss'}$ and overlap matrix elements $\mathcal{S}_{ss'}$ are given for the two sublattices s = A,B for the initial s and the final state s' [53, 55, 56]. The eigenvalues for a given $\boldsymbol{k}$ can be found by solving the secular equation $\det[\mathcal{T} - \varepsilon\mathcal{S}] = 0$, resulting in

$$\varepsilon_i^{\pm} = \Delta\varepsilon \pm \sqrt{(\Delta\varepsilon)^2 - (|\mathcal{T}_{AA}|^2 - |\mathcal{T}_{AB}|^2)}, \tag{9}$$

with

$$\Delta\varepsilon = \frac{Re[\mathcal{T}_{AB}\mathcal{S}_{AB}^*] - \mathcal{T}_{AA}\mathcal{S}_{AA}}{|\mathcal{S}_{AA}|^2 - |\mathcal{S}_{AB}|^2}.$$

$\mathcal{T}_{AB}^{*} = \mathcal{T}_{BA}$ defines nearest neighbour interaction (hopping between sublattices) and $\mathcal{T}_{AA} = \mathcal{T}_{BB}$ next-nearest neighbour interaction (hopping within one sublattice). Accordingly $\mathcal{S}_{AB}^{*} = \mathcal{S}_{BA}$ defines the wave function overlap between nearest neighbours and $\mathcal{S}_{AA} = \mathcal{S}_{BB}$ between next-nearest neighbours. The plus and minus sign in Eq.(9) corresponds to the bonding π valence band and anti-bonding π^* conduction band, respectively. To find an analytical solution, further approximations are necessary. Using only nearest neighbour interaction, the transfer and overlap matrix elements reduce to

$$\mathcal{T}_{AB} = \mathcal{T}_0 \varepsilon(\boldsymbol{k}),\ \mathcal{S}_{AB} = \mathcal{S}_0 \varepsilon(\boldsymbol{k}), \tag{10}$$

in which $\mathcal{T}_0$ is the carbon-carbon interaction energy and $\mathcal{S}_0$ is the overlap integral. Typical values obtained from experimental data are -2.5 to -3.3 eV for $\mathcal{T}_0$, and -0.07 to -0.13 for $\mathcal{S}_0$ [55, 56]. As $\mathcal{S}_0$ is small it can be neglected. For both assumptions, considering only nearest neighbour interaction and neglecting $\mathcal{S}_0$, the eigenvalues in Eq.(9) simplify to $\varepsilon_i(\boldsymbol{k})^{\pm} = \pm\mathcal{T}_0|\varepsilon(\boldsymbol{k})|$. The established result is [53]

$$\varepsilon^{\pm}(\boldsymbol{k}) = \pm\sqrt{3 + 2\cos(ak_y) + 4\cos(\frac{\sqrt{3}}{2}ak_x)\cos(\frac{1}{2}ak_y)} \tag{11}$$

plotted in Fig. 1 (c) in the first BZ. At the K and K' points the band gap closes and the dispersion becomes linear for small energies.

Linear Dispersion At the K and K' points, the dispersion can be expanded for small wave vectors $\boldsymbol{k}' = \boldsymbol{K}+\boldsymbol{k}$, with $|\boldsymbol{k}| \ll |\boldsymbol{K}|$ [2, 55]. The resulting energy dispersion is given by

$$\varepsilon^{\pm}(\boldsymbol{k}) = \pm\hbar v_{\mathrm{F}}|\boldsymbol{k}|. \tag{12}$$

In this equation the Fermi velocity is given by $v_{\mathrm{F}} = \mathcal{T}_0\sqrt{3}a/(2\hbar)$. For typical values of $\mathcal{T}_0$ the Fermi velocity is in the range of $v_{\mathrm{F}} \approx 10^6$ m/s, which is 300 times smaller than the speed of light [55, 56]. Again, the plus and minus sign corresponds to the bonding π valence band and anti-bonding π^* conduction band, respectively.

The band structure close to the K and K' points can also be described with

the two Dirac Hamiltonians [2]

$$\begin{aligned} \mathcal{H}_{\mathrm{K}} &= v_{\mathrm{F}}\sigma \cdot k \\ \mathcal{H}_{\mathrm{K}'} &= v_F\sigma^* \cdot k, \end{aligned} \tag{13}$$

where $\sigma = (\sigma_x, \sigma_y)$ and $\sigma^* = (\sigma_x, -\sigma_y)$ are the Pauli matrices. The carriers have a well-defined chirality, called pseudospin, near the Dirac point. As a distinction from the Dirac equation, the two components spinor wave function represents the two sublattices A and B.

2.1.3 Bi_2Te_3- and Sb_2Te_3-based Topological Insulators

Topological insulators are characterized by an insulating bulk and conducting surface states, which are described by a linear dispersion [6]. In these bound states spin and momentum are locked and they are robust against disorder. Such bound states are formed at the interface between regions with trivial and non-trival band structure [8, 49]. The materials Bi_2Te_3, Sb_2Te_3 and Bi_2Se_3 relevant for this thesis, were experimentally confirmed [28] soon after they were proposed to be 3D TIs [21].

In the following section, the crystallographic and electronic structure of Bi_2Te_3- and Sb_2Te_3-based three dimensional topological insulators is presented. Then their two dimensional surface states are discussed.

Crystalline Structure Bismuth (Bi), Antimony (Sb), Selenium (Se) and Tellurium (Te) are heavy V and VI group elements, with partially filled *s* and *p* orbitals[1]. From these elements the four stoichiometric compounds Bi_2Se_3, Bi_2Te_3, Sb_2Te_3, and Sb_2Se_3 can be formed. As it will be shown later, the lightest of all four, Sb_2Se_3, has a trivial band structure and is neglected in the following discussion. The crystal structures of Bi_2Se_3, Bi_2Te_3, and Sb_2Te_3 are shown in Fig. 2 (a)-(c). The rhombohedral unit cell has a five-atomic basis and the crystal is described by three primitive lattice vectors $t_{1,2,3}$. The materials are formed by atomic layers, each consisting of the same chemical element, which are bound in two different ways. Five layers of alternating elements, e.g. Te-Bi-Te-Bi-Te, form a so called quintuple layer, see Fig. 2 (a). The coupling between two different atomic layers is strong, while two quintuple layers (Te-Te interface) are weakly bound by van der Waals forces, see Fig. 2 (b). The

[1] Partially filled orbitals in italic: Bi 4f14 5d10 *6s2 6p3*, Se 3d10 *4s2 4p4*, Te 4d10 *5s2 5p4*, Sb 4d10 *5s2 5p3*

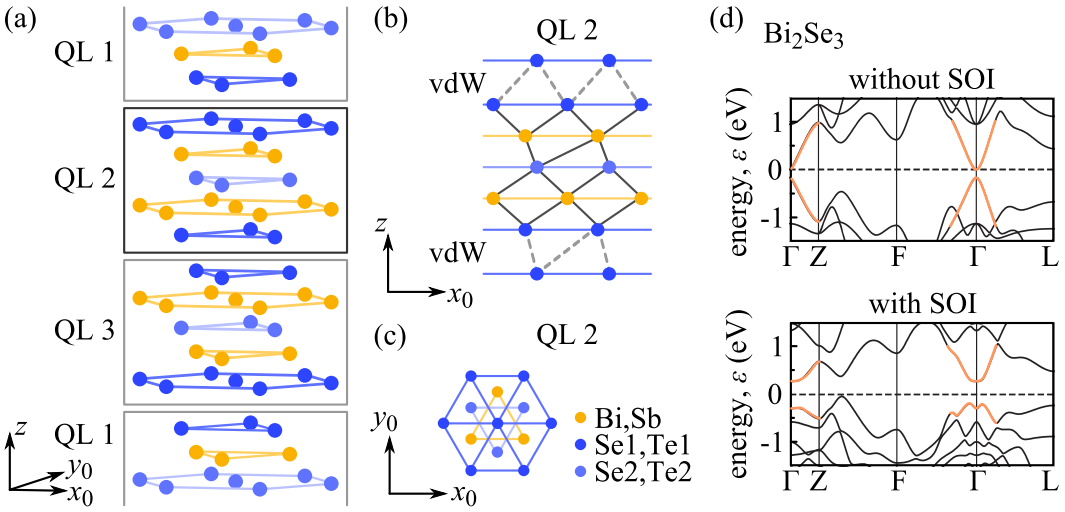

Figure 2: Crystalline and electronic structure of Bi_2Se_3, Bi_2Te_3, and Sb_2Te_3. (a) Side view shows atomic layers, with quintuple layer ordering. (b) Quintuple layers are bound by van der Waals forces, atomic layers strong. (c) Top view shows three-fold rotational symmetry. (d) Electronic structure obtained with tight binding approach taking into account chemical bonds between atoms and crystal field splitting. In lower panel spin orbit interaction is additionally taken into account and anti-crossing of bands around Γ point is visible. Adapted from Ref. [21].

materials five atoms in the unit cell [21] and belong to the D_{3d} symmetry point group, i.e. they are centrosymmetric and have a three-fold rotational symmetry around z. This three-fold symmetry can be seen, e.g., in the top view of the crystal structure in the Bi layer, see Fig. 2 (c).

Electronic Structure The first band structure calculations of Bi_2Te_3 were performed by Lee and Pincherle in 1963 [57]. At that time the material was still treated as narrow gap semiconductor. The latest and for this work most relevant approach was done by Zhang *et. al.* in 2009 [21], considering spin orbit interaction. Besides the bulk band structure, they calculated the surface bands and predicted that Bi_2Se_3, Bi_2Te_3, and Sb_2Te_3 are topological insulators. In their calculations they neglect the s orbitals, since mainly the p orbitals conduct near the Fermi energy. Focusing on Bi_2Se_3, they first determine the relevant bonds between Bi and Se. The formation of chemical bonds and the hybridisation of the atomic states pushed Se energetically down while Bi is lifted. In a second step the crystal field splitting between different p orbitals is taken into account. The resulting bulk band structure is shown in Fig. 2 (d) in the top panel. In the bottom panel the influence of spin orbit interaction (SOI), considered in a last step, is shown. For large energies the band structure

remains unchanged. Close to the Fermi energy at the Γ points, however, the band gap becomes tunable depending on the spin orbit interaction parameter. Above a certain value, conduction and valence band start to invert. This band inversion is indicated in Fig. 2 (d) by the anti-crossing feature around the Γ point. The same calculations were performed for the other three compounds, showing that in Sb_2Se_3 the spin orbit interaction is not strong enough to invert the bands.

Inverted Band Structure and Bound State at Interface The anti-crossing feature in Fig. 2 (d) indicates the inversion of bands, and hence that the energy gap can be characterized by a negative mass. In 1979 Jackiw and Rebbi found, that at the interface between regions with negative mass (inverted band structure) and positive mass (trivial band structure) a bound state is formed [15]. In the following a similar approach is used to derive the properties of the surface states of 3D TIs. To find this solution, the problem is first reduced to the one dimensional case, afterwards the example is expanded to two and three dimensions. By adding a quadratic correction to the mass term, which break the symmetry in the mass term, it is possible to distinguish systems with trivial or non-trivial topology. The derivation follows Refs. [8, 49].

For the one dimensional case, a mass $m(x) = -m_1, m_1 > 0$, which is negative at $x < 0$ and $m(x) = m_2, m_2 > 0$ positive at $x > 0$, is defined. The Hamiltonian for the interface at $x = 0$ is given for one dimension x by [8, 49]

$$\mathcal{H}(x) = -iv\hbar\partial_x\sigma_x + m(x)v^2\sigma_z. \tag{14}$$

where $\sigma_{x,y}$ are the Pauli matrices and v is the velocity.

One can find a solution at zero energy with the corresponding wave function

$$\psi(x) = \sqrt{\frac{v}{\hbar}\frac{m_1 m_2}{(m_1 + m_2)}} \begin{pmatrix} 1 \\ i \end{pmatrix} e^{-|m(x)\,vx|/\hbar}. \tag{15}$$

This wave function does not vanish at $x = 0$ and a bound state (end state) is found at the interface, which decays exponentially. This is true even for $m_2 \to \infty$, i.e. for vacuum. Note that for the case of $m_1 = m_2$, the solution describes the soliton, calculated by Jackiw and Rebbi in 1976 [15]. The one dimensional case already shows that bound states exist at the interface between

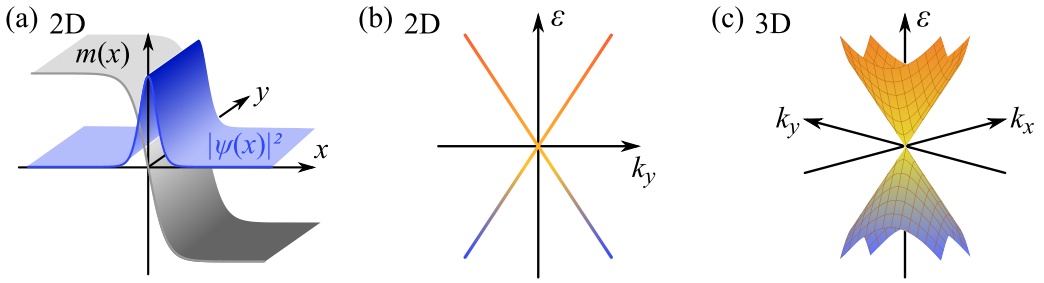

Figure 3: (a) Probability density $|\psi(x)|^2$ of bound states at interface between regions with negative and positive mass $m(x)$ and (b) resulting dispersion. (c) For three dimensional case dispersion is a Dirac cone along k_x and k_y directions. Adapted from Refs. [8, 49].

regions with negative and positive mass.

The next step towards surface states in 3D TIs is to derive the solution for two dimensions. Considering an interface parallel to the y axis, which separates regions with negative $m(x) = -m_1, m_1 > 0$ for $x < 0$ and positive mass $m(x) = m_2, m_2 > 0$ for $x > 0$, again a solution at $x = 0$ and zero energy can be found, see Fig 3 (a). The Dirac Hamiltonian is given for $p_z = 0$ as [8, 49]

$$\mathcal{H}(x) = vp_x\sigma_x \pm vp_y\sigma_y + m(x)v^2\sigma_z. \tag{16}$$

Here, the two solutions are given by the wave functions

$$\psi_+(x, k_y) = \sqrt{\frac{v}{\hbar}\frac{m_1 m_2}{(m_1 + m_2)}} \begin{pmatrix} 1 \\ 0 \\ 0 \\ i \end{pmatrix} e^{ik_y y - |m(x)\, vx|/\hbar}, \tag{17}$$

$$\psi_-(x, k_y) = \sqrt{\frac{v}{\hbar}\frac{m_1 m_2}{(m_1 + m_2)}} \begin{pmatrix} 0 \\ 1 \\ i \\ 0 \end{pmatrix} e^{ik_y y - |m(x)\, vx|/\hbar}$$

The energy dispersion of the bound states is given by $\varepsilon_{k,\pm} = \pm v\hbar k_y$, describing a linear dispersion along k_y, the direction along the interface, see Fig. 3 (b). The bound states form conducting channels along the interface at zero energy and decay exponentially into the bulk.

These bound states are very close to the definition of topological insulators. However, the symmetry in the mass term $m(x)v^2\sigma_z$ makes a distinction

between regions with negative and positive mass impossible. A definition of trivial and non-trivial systems is introduced by defining the vacuum as a benchmark. This is done by adding a quadratic correction to the rest mass term $(mv^2 - Bp^2)$, which allows a distinction of trivial and non-trivial regions. The energy band gap is still given by mv^2, while the additional term Bp^2 breaks symmetry between m and $-m$. An illustrative presentation of this is that a pseudospin is given by the sign of the mass term m at $p = 0$, while at large p it is given by the sign of B. Now, for the product $mB < 0$ the pseudospin is the same for large and small p, while for $mB > 0$ the pseudospin is opposite at $p = 0$ and $p \to \infty$. This makes a topologically difference between both cases. Another way to characterize the topological states is by using the Chern number. Here it is given by $n_\pm = \pm(sgn(m) + sgn(B))/2$. For different signs of m and B the Chern number is zero and the system is classified as topologically trivial. For the case, that m and B have the same signs, the Chern number is $n_\pm = \pm 1$ and the system is classified as topologically non-trivial [8].

As a last step, the three dimensional case together with the quadratic correction in the mass term is derived. For a (xy) interface at $z = 0$, separating again regions with positive and negative mass. The Dirac Hamiltonian is given by [8, 49]

$$\mathcal{H}_{3D} = vp_x\alpha_x + vp_y\alpha_y + B(p_x^2 + p_y^2)\beta. \tag{18}$$

One can find a gapless Dirac equation $\mathcal{H}_{\text{eff}} = v\, sgn(B)(p_x\sigma_x + p_y\sigma_y)$ with a corresponding dispersion relation of

$$\varepsilon_{p,\pm} = \pm v\sqrt{p_x^2 + p_y^2}. \tag{19}$$

This Dirac cone is shown in Fig. 3 (c). Note that for the three-fold symmetry of Bi_2Te_3- and Sb_2Te_3-based 3D TIs an additional hexagonal warping term is added to the effective Hamiltonian [28].

Non-Trivial Topology To conclude, the existence of bound states is found for the modified Dirac Hamiltonian and the condition $mB > 0$. These states are characterized by a linear dispersion. Their momentum is locked to the spin and carriers propagating in opposite direction have opposite spin. Therefore, backscattering is only possible with a spin-flip. These states are protected by time reversal symmetry and fulfil Kramers degeneracy theorem.

After the prediction [21], the existence of 2D surface states with linear dispersion was confirmed by ARPES [28]. Further studies showed the existence of a spin helix [30, 31] or that in these materials at least six quintuple layers are necessary [58]. For thinner films an energy gap opens, due to interlayer coupling.

2.2 Nonlinear Optoelectronic Phenomena

The homogeneous illumination of materials with alternating electric fields can lead under certain conditions to direct electric currents. In this section such currents, namely the photogalvanic [59] and the photon drag current [60], are introduced. Well known since the 1970s, these phenomena are widely studied in bulk materials, as well as in low dimensional systems and provide a basis to understand different microscopic material properties [38, 61]. In this thesis, they are applied to systems characterized by a linear dispersion like graphene or 3D TIs. Both, the photogalvanic and the photon drag effect are discussed on the basis of a phenomenological theory, which is later used for the discussion of the experimental results in Chap. 4 and Chap. 5. The phenomenological description provides a general explanation of the occurring photocurrent, including the current direction and dependence on the radiation's polarization state. These effects were observed in different energy regions [38]: in the semi-classical regime, where the photon energy is much smaller than the Fermi energy and only intraband transitions are possible and in the quantum mechanical regime, where the photon energy becomes comparable to the Fermi energy and interband transitions can take place.

In the following only semi-classical models are discussed since the majority of the experimental results is obtained with small energy terahertz radiation in the meV range. The presented microscopic theories use the carrier distribution function, for example derived with the kinetic Boltzmann equation [62], to calculate the current.

2.2.1 Phenomenological Theory

Directed photocurrents can be induced by high frequent alternating electric fields, provided in this work by terahertz radiation. Phenomenologically the interaction of electric fields with the current density is written as a Taylor

series [38]

$$j_l = \sum_m \sigma^{(1)}_{lm}(\omega = 0) E_m(\omega = 0) + \sum_{mn} \sigma^{(2)}_{lmn}(\omega, \boldsymbol{q}) E_m(\omega) E^*_n(\omega) + ... \tag{20}$$

in which $\boldsymbol{E}$ is the electric field, $\boldsymbol{E}^*(\omega) = \boldsymbol{E}(-\omega)$ is the complex conjugate of $E(\omega)$, σ is the conductivity, and $\boldsymbol{q}$ is the photon momentum. The indices m, n, l run over the Cartesian coordinates x, y, z. The first term in Eq.(20) is Ohm's law, the change of the current density induced by applying a static electric field $\boldsymbol{E}(\omega = 0)$, and described by the conductivity $\sigma^{(1)}(\omega = 0)$. For alternating fields this linear response becomes zero in average. The second term in Eq.(20) is proportional to the squared electric field and is relevant for the experimental results in this thesis. It can be used to describe the photogalvanic and the photon drag effect, which are derived in the following.

The second order conductivity $\sigma^{(2)}_{lmn}(\omega, \boldsymbol{q})$ can be separated into two parts, one depending on the photon momentum and one which is independent of it

$$\sigma^{(2)}_{lmn}(\omega, \boldsymbol{q}) = \sigma^{(2)}_{lmn}(\omega, \boldsymbol{q} = 0) + \sigma^{(2)}_{lmn}(\omega, \boldsymbol{q} \neq 0). \tag{21}$$

The two parts can be redefined as $\sigma^{(2)}_{lmn}(\omega, \boldsymbol{q} = 0) = \chi_{lmn}(\omega)$ and $\sigma^{(2)}_{lmn}(\omega, \boldsymbol{q} \neq 0) = T_{lmno}\, q_o$, where χ_{lmn} and T_{lmno} are third and fourth rank tensors, respectively. With Eq.(21), the second term in Eq.(20) can be rewritten to [38]

$$j_l = \sum_{mn} \chi_{lmn} E_m E^*_n + \sum_{mno} T_{lmno} E_m E^*_n q_o. \tag{22}$$

The first sum of Eq.(22) describes the photogalvanic effect, whereas the second sum depending on $\boldsymbol{q}$ describes called photon drag effect. Both contributions depend on the state of polarization and the orientation of the electric field vector. The product

$$E_m E^*_n = \{E_m E^*_n\} + [E_m E^*_n] \tag{23}$$

can be split into a real[2], symmetric part $\{E_m E^*_n\} = \frac{1}{2}(E_m E^*_n + E_n E^*_m)$ and an imaginary[3], anti-symmetric part $[E_m E^*_n] = \frac{1}{2}(E_m E^*_n - E_n E^*_m)$. The linear

[2] Consider $a = m + in$,$b = u + iv$ being complex matrices and $a^* = m - in$, $b^* = u - iv$ being the complex conjugated ones. Then $\{ab^*\} = \frac{1}{2}(ab^* + ba^*)$ is real since $\frac{1}{2}((m+in)(u-iv) + (u+iv)(m-in)) = mu + nv$.

[3] Analogue to [2], $[ab^*] = \frac{1}{2}(ab^* - ba^*)$ is imaginary.

polarization can be described by both parts. To describe circular polarization, the fourth rank tensor of the anti-symmetric part is reduced with tensor contraction to a second rank pseudotensor γ. For this purpose, the Levi-Civita permutation tensor δ is used to rewrite it as cross product of the electric fields $i\sum_{mn}\chi_{lmn}[E_m E_n^*] = i\sum_l \gamma_{lp}\delta_{pmn}[E_m E_n^*] = i\sum_l \gamma_{lp}(\boldsymbol{E}\times\boldsymbol{E}^*)_p$. The cross product of the electric field can be expressed as $\gamma_{il}\hat{e}_l P_{circ}E^2$ with the unit vector $\hat{e} = \boldsymbol{q}/q$ pointing into the radiation propagation direction and P_{circ} being the degree of circularly polarized radiation. From these considerations follows that both, the photon drag and the photogalvanic effect, can be induced by linearly and circularly polarized radiation. Their polarization dependence and restrictions to material symmetry groups is clarified in the following sections.

2.2.2 The Photogalvanic Effect

The photogalvanic effect [38]

$$j_l = \sum_{mn}\chi_{lmn}E_m E_n^*, \tag{24}$$

is caused by the squared electric field and is restricted to non-centrosymmetric materials. This is because in centrosymmetric materials the current density vector changes its sign at spatial inversion, while the squared electric field vector does not. Consequently, the current is forbidden in such systems. Furthermore, the photogalvanic effect depends on the point group symmetry of the considered material and these symmetry arguments are used to identify the direction and polarization dependence of the current. The photogalvanic effect was observed in a great number of materials, including two and three dimensional semiconductors [38]. Here, GaSb/InAs quantum wells [63–65], are considered as an example [66–68]. They are proposed to be a two dimensional topological insulator and were investigated in the framework of this dissertation, but are not included.

If grown along the [001] direction, zinc-blend type-II quantum wells belong to the point group symmetry C_{2v}: it is described by a two-fold symmetry axis along the growth direction $z||[001]$ and two mirror planes in (xz) and (yz). The coordinates x, y are oriented along $x||[1\bar{1}0]$ and $y||[110]$. Due to carrier confinement the photogalvanic current can only flow in the quantum well plane. For linearly polarized radiation the photogalvanic effect is described by two linearly independent components χ_{xxz} and χ_{yyz}, and Eq.(24) reduces

to [38]

$$\begin{aligned} j_x &= \chi_{xxz}(E_x E_z^* + E_z E_x^*), \\ j_y &= \chi_{yyz}(E_y E_z^* + E_z E_y^*) \end{aligned} \tag{25}$$

for the current flowing in the quantum well plane, probed along the x or y direction. The current is zero for normal incident radiation, since there the E_z component vanishes. For a certain plane of incidence, e.g. the (xz) plane, Eq.(25) is given by

$$\begin{aligned} j_x &= \hat{e}_x E^2 \left[(\chi_{xxz} + \chi_{yyz}) + (\chi_{xxz} - \chi_{yyz})\cos(2\alpha)\right], \\ j_y &= \hat{e}_x E^2 \left[\chi_{xxz}\sin(2\alpha)\right] \end{aligned} \tag{26}$$

where $\hat{e}$ is the unit vector pointing in the direction of radiation propagation and α being the azimuthal angle between the y axis and the electric field direction. Equation (25) shows the dependence of j on the angle of incidence and on the orientation of the electric field vector. For circularly polarized radiation and the C_{2v} point group symmetry, Eq.(24) is given by

$$\begin{aligned} j_x &= \hat{e}_y E^2 \gamma P_{circ}, \\ j_y &= \hat{e}_x E^2 \gamma P_{circ} \end{aligned} \tag{27}$$

in which $\gamma = \gamma_{xy} = \gamma_{yx}$ is the coefficient for the circular photogalvanic effect and P_{circ} is the degree of radiation helicity. A helicity sensitive contribution to the photocurrent is present only in the direction normal to the plane of incidence, e.g. $j_y \propto \hat{e}_x$, and the current along the x direction is zero for the (xz) plane of incidence.

A microscopic model for the photogalvanic effect in asymmetrically grown quantum wells belonging to the C_{2v} class is developed in Refs. [66–68]. A semi-classical approach is used in these works, since the photon energy in the terahertz range is usually much smaller than the Fermi energy ($\hbar\omega \ll \varepsilon_{\mathrm{F}}$), and Drude-like free carrier absorption dominates. The alternating in time THz electric field can be written as

$$\boldsymbol{E}(t) = \boldsymbol{E} e^{-i\omega t} + \boldsymbol{E}^* e^{i\omega t}. \tag{28}$$

The electric field, acting on the free carriers in the QW, can be separated into an in-plane ($E_{||} = E_x, E_y$) and an out-of-plane part (E_z). The in-plane com-

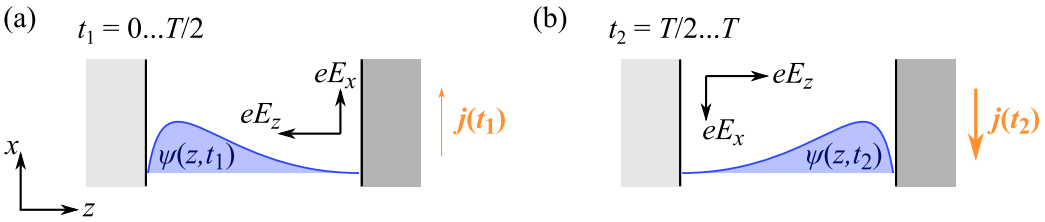

Figure 4: Model for linear photogalvanic effect based on asymmetric scattering probability for an asymmetric quantum well along growth direction z. For first (a) and second (b) half time period currents have opposite directions, but different magnitudes, leading to a net current average over time along x direction. Adapted from Refs. [67, 68].

ponent $E_{||}(t)$ accelerates the carries and drives them back and forth with the radiation frequency ω. The force acting on the carriers is zero if averaged over time and carriers are scattered symmetrically. Therefore, no current exists for normal incident radiation, since there only in-plane electric fields are present. At oblique angles of incidence, however, an out-of-plane component of the electric field $E_z(t)$ exists. This force additionally pushes the wave function $\psi(z,t)$ along the z direction. As the type-II QW is asymmetric in this direction, the scattering rate is different for the two QW layers, i.e., the mobility becomes time dependent and is modulated with the radiation frequency ω. The resulting drift velocity v_{drift} differs from the one generated a half period later. The influence of $E_z(t)$ on the carriers alone does not yet lead to a net current, as in the case of an in-plane electric field. However, the combination of both, $E_{||}(t)$ and $E_z(t)$, results in a current.

This process is illustrated in Fig. 4 for asymmetric quantum wells, e.g. type-II GaSb/InAs, for the two time intervals $t_1 = 0...T/2$ and $t_2 = T/2...T$, where T is the period of the radiation. In the time interval t_1 the electric forces accelerate the carriers upwards and simultaneously push the wave function to the left boundary, see Fig. 4 (a). This results in a current, assuming holes, along the positive x direction. For the time interval t_2 this process reverses and a current flows in the opposite direction. As scattering is different at the left and right boundary an imbalance in mobility leads to a net current. The model is shown for electric fields E_z and E_x, which results in a current in x direction, see Eq.(25). This model based on asymmetric scattering can be applied to other systems, e.g. to QWs with asymmetric doping [67].

The model can be extended to circular polarized radiation. There the in- and out-of-plane electric fields are phase shifted with respect to each other by $\pm\pi/2$. This means that one is always zero, while the other one is maximal.

Therefore, the time average over the electric fields and hence the current is zero in the static limit at $\omega \to 0$. A current formation becomes possible only due to retardation between the electric field direction and the drift velocity at finite frequencies. The drift velocity v_{drift} is delayed by a factor $\arctan(\omega\tau_p)$, where τ_p is the momentum relaxation time, i.e., an accelerated carrier is still moving along a certain direction although the applied force has already changed.

Besides this model, a microscopic theory is developed on the basis of asymmetric scattering and the time dependent drift velocity [66, 67]. Solving the Newton equation for the drift velocity v_{drift}, the total current density $j = v^{(0)}_{\mathrm{drift}} e N_e$ is given as

$$j = -\frac{e^3 \zeta N_e \tau_p^2}{m^*}\left(\frac{E_{||} E_z^*}{1 - i\omega\tau_p} + \frac{E_{||}^* E_z}{1 + i\omega\tau_p}\right) \tag{29}$$

with the electron density N_e, the effective mass $m^* = p_{\mathrm{F}}/v_{\mathrm{F}}$, and the momentum relaxation time τ_p. The scattering asymmetry ζ can be expressed with the polar angles ϕ_k, $\phi_{k'}$ and momentum vectors k, k' before and after the scattering event, respectively. For the (xz) plane of incidence the current density is given as

$$\begin{aligned} j_x = & -\frac{e^3 N_e}{m^*}\frac{\zeta\tau_p^2 E_0^2}{1 + (\omega\tau_p)^2}\, t_p^2 \sin\theta\cos\theta[(1 - \cos(4\varphi))/2], \\ j_y = & \frac{e^3 N_e}{m^*}\frac{\zeta\tau_p^2 E_0^2}{1 + (\omega\tau_p)^2}\, t_p t_s \sin\theta[\sin(4\varphi)/2 + \omega\tau_p \sin(2\varphi)]. \end{aligned} \tag{30}$$

t_s and t_p are the transmission coefficients for s- and p-polarized radiation given by

$$t_s = \frac{2\cos\theta}{\cos\theta + n_\omega \cos\theta'},\ t_p = \frac{2\cos\theta}{n_\omega \cos\theta + \cos\theta'} \tag{31}$$

in which θ' is the refraction angle, with $\sin\theta' = \sin\theta/n_\omega$ related to the refraction index n_ω. The angle φ denotes the experimental rotation of a quarter wave plate. With it the Stokes parameters of linear polarized light are given by $s_1 = -(1 - \cos(4\varphi))/2$ and $s_2 = -\sin(4\varphi)/2$, corresponding to $-\cos(2\alpha)$ and $-\sin(2\alpha)$ in Eq.(26). The degree of helicity is given here by $\sin(2\varphi)$ and corresponds to P_{circ} in Eq.(27). Equation (30) describes well the phenomenological theory and experimental finding, see e.g. Ref. [68].

2.2.3 The Photon Drag Effect

The photon drag effect [38]

$$j_l^{PDE} = \sum_{mno} T_{lmno} E_m E_n^* q_o \tag{32}$$

is due to the additional transfer of the photon momentum $\boldsymbol{q}$, and in contrast to the photogalvanic effect, not restricted to non-centrosymmetric materials. It was observed, like the photogalvanic effect, in many materials and depends on the considered point group symmetry [38]. Symmetry arguments are used to demonstrate in which direction and for which polarization a photocurrent is generated.

This is discussed on the example of graphene [40, 69, 70]. Infinite, free standing graphene belongs to the point group symmetry D_{6h}. It is centrosymmetric and has a six-fold rotational symmetry around the z direction. For real structures the symmetry is preserved if caped with identical layers, e.g. hexagonal Boron Nitride. In this infinite, centrosymmetric system the photon drag effect can be generated, however not the photogalvanic effect. For the D_{6h} point group symmetry the photon drag tensor T has five non-zero, linearly independent entries. Two of the five give rise to effects with out-of-plane components q_z and E_z. They can be neglected, as graphene is strictly one dimensional. The remaining three constants T_1, T_2, and $\tilde{T}$ contain only in-plane components of the electric field $E_{x,y}$ and of the photon momentum $q_{x,y}$. The photon drag current along the orthogonal in-plane directions x and y and for the (xz) plane of incidence is given by [40, 69]

$$\begin{aligned} j_x = &\ T_1 q_x \frac{|E_x|^2 + |E_y|^2}{2} + T_2 q_x \frac{|E_x|^2 - |E_y|^2}{2}, \\ j_y = &\ T_2 q_x \frac{E_x E_y^* + E_x^* E_y}{2} - \tilde{T} q_x \hat{e}_z P_{circ} (|E_x|^2 + |E_y|^2). \end{aligned} \tag{33}$$

The coefficient T_1 corresponds to the longitudinal photon drag effect, T_2 to the linear photon drag effect caused by linearly polarized radiation, and $\tilde{T}$ to the circularly photon drag effect caused by circular polarized radiation. These three contributions are illustrated in Fig. 5. The longitudinal photon drag effect, Fig. 5 (a), is polarization independent and only proportional to the radiation intensity ($|E_x|^2 + |E_y|^2 = E_0^2$) and the in-plane photon momentum. A linear photon drag current, Fig. 5 (b), can flow in any direction. The different magnitudes of the current picked up along the x and y directions depend

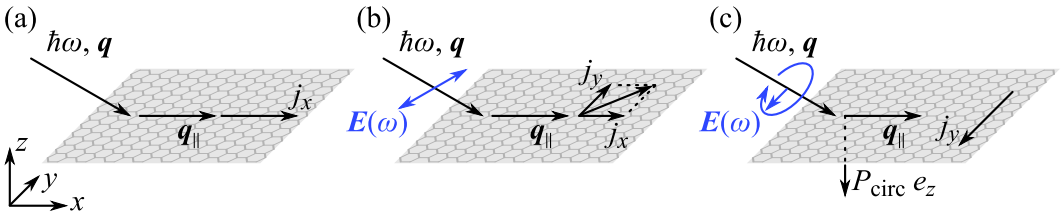

Figure 5: Photon drag currents in graphene: (a) The longitudinal one is proportional to momentum $q_{||}$ and intensity I only and flows in direction of radiation propagation. (b) The linear one is additional sensitive to electric field orientation and can flow in any direction. (c) The circular one is sensitive to radiation helicity P_{circ} and flows always normal to plane of incidence. Adapted from Refs. [40]

on the orientation of the electric field vector, given by $(E_x E_y^* + E_x^* E_y)$ and $(|E_x|^2 - |E_y|^2)$. A circular photon drag current, see Fig. 5 (c), is proportional to the angular photon momentum and flows only normal to the plane of incidence, $j_y \propto q_x$. All three effects are zero at normal incident radiation ($q_x = 0$) and reverse their sign if the angle of incidence is changed from positive to negative. Additionally the circular photon drag effect reverses its sign by changing circular polarized radiation from left to right handed. Neglecting the polarization independent longitudinal photon drag effect, Eq.(33) can be written for elliptically polarized radiation as

$$\begin{aligned} j_x = &\quad -T_2 q_x E^2 (1 + \cos(4\varphi))/4, \\ j_y = &\quad -T_2 q_x E^2 \sin(4\varphi)/4 - \tilde{T} q_x \hat{e}_z E^2 P_{circ}. \end{aligned} \tag{34}$$

The microscopic origin of the photon drag effect in a single graphene layer is derived in Refs. [69, 71]. For the regime in which the photon energy is much smaller than the Fermi energy ($\hbar\omega \ll \varepsilon_{\mathrm{F}}$), intraband transitions via virtual states are relevant and a semi-classical approach can be used. The distribution function is derived with the kinetic Boltzmann equation

$$\frac{\partial f}{\partial \boldsymbol{t}} + v\frac{\partial f}{\partial \boldsymbol{r}} + \frac{e}{\hbar}(\boldsymbol{E} + [\boldsymbol{v} \times \boldsymbol{B}]/c)\frac{\partial f}{\partial \boldsymbol{k}} = Q_{coll}\{f\} \tag{35}$$

with the collision integral $Q_{coll}\{f\}$ and the distribution function

$$f(\boldsymbol{k}, r, t) = f_0(\epsilon_{\boldsymbol{k}}) + f_1(\boldsymbol{k}) e^{i(q\boldsymbol{r} - \omega \boldsymbol{t})} + f_2(\boldsymbol{k}) \tag{36}$$

where f_0 is the equilibrium distribution function, f_1 is the linear response and f_2 is a homogeneous and time-independent second order correction. With the

latter, the current density can be obtained using

$$j = 4e \sum_{\boldsymbol{k}} v_{\boldsymbol{k}} f_2(\boldsymbol{k}) \tag{37}$$

Note that the factor 4 comes for spin and valley degeneracy in graphene. The collision integral is given for the time and space averaged correction f_2 by

$$Q_{coll}\{f_2\} = \frac{2e}{\hbar} Re\Big\{\Big(\boldsymbol{E} + [\boldsymbol{v} \times \boldsymbol{B}]/c\Big)\frac{\partial f_1^*}{\partial \boldsymbol{k}}\Big\} \tag{38}$$

which includes the complex conjugate of the first order correction f_1, the electric force $e\boldsymbol{E}$, and the Lorentz force $e[\boldsymbol{v} \times \boldsymbol{B}]$. Only the latter depends on the momentum. Substituting the solution of Eq.(38) in Eq.(37), all three photon drag coefficients T_1, T_2 and $\tilde{T}$ can be calculated, for details see Ref. [71].

3 Methods

In the following chapter the investigated samples and experimental methods are presented. The first section gives a description of Bi_2Te_3- and Sb_2Te_3-based 3D TIs and graphene, used in the experiments. A feature of this work is that the experiments presented are performed with a wide range of excitation frequencies between $f = 0.6$ and 60 THz. This is possible only by using quite different laser sources, comprising molecular gas lasers in the far infrared (90 - 496 μm), CO_2 lasers in the near infrared (9 - 11 μm) and a quantum cascade laser in the near infrared (5 μm). Additionally, a free-electron laser is used to fill in missing wavelengths. Due to the diversity of the sources in operation mode a short introduction of the lasers and their functionality is given in the second section. The chapter ends with a description of the experimental setup.

3.1 Investigated Samples

3.1.1 Bi_2Te_3- and Sb_2Te_3-based Thin Films

Experiments on 3D TIs are performed on Bi_2Te_3- and Sb_2Te_3-based thin films. Besides the stoichiometric compounds Bi_2Te_3 and Sb_2Te_3, different ternary $(Bi_{1-x}Sb_x)_2Te_3$ films and Bi_2Te_3/Sb_2Te_3 heterostructures are used. All samples were grown by molecular beam epitaxy (MBE) in collaboration with the group of Dr. Gregor Mussler/Prof. Dr. Detlev Grützmacher at the Peter Grünberg Institut, Forschungszentrum Jülich.

The thin films are grown on (111) oriented silicon (Si) substrates, placed on SiO_2/Si wafers. The sample geometry is sketched in Fig. 6 (a). To suppress the influence of dangling bonds from the Si(111) substrate a single amorphous Te layer is deposited. The latter additionally compensates the high lattice mismatch, e.g. 14% for Bi_2Te_3, and van der Waals growth starts [72, 73]. The growth process begins in nucleation centres, crystallographically aligned to the substrate. From these points of nucleation, which are only weakly bound to the substrate, the overgrowth of layers starts as different nucleation centres merge. Scanning tunnelling microscope (STM) measurements reveal that terraces with quintuple layer height of approximately 1 nm are present on the surface. These terraces are often seen in Bi_2Te_3, while they are hardly present in Sb_2Te_3 [74]. To verify the crystal quality, high-resolution high-angle annular dark field (HAADF) spectroscopy is used [75–77]. It is a variation of scanning transmission electron microscopy, where the scattered electrons

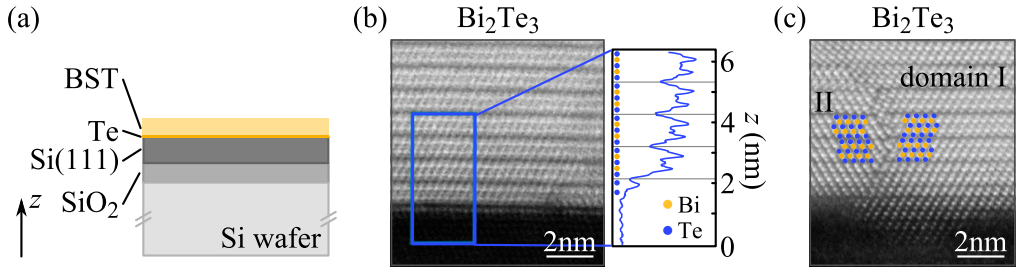

Figure 6: (a) Sample geometry: On a Si/SiO_2 wafer a Si(111) layer is grown, that is important for symmetry. On a one atomic thick amorphous Te layer, Bi_2Te_3- and Sb_2Te_3-based thin films are grown by van der Waals epitaxy. (b) High-resolution high-angle annular dark field images of pure Bi_2Te_3, and (c) formation of two different regions of domain separated by a vertical and a horizontal domain wall. Line scan in (b) shows periodicity of quintuple layers. The position of atoms is schematically shown with coloured dots. Adapted from Ref. [73].

are collected, and the assembly of atoms can be imaged [73]. The atomic resolution in these experiments enables the assignment of single layers. Such a measurement is shown in Fig. 6 (b) for Bi_2Te_3. Due to Coulomb interaction (Rutherford scattering) atoms with higher atomic numbers appear brighter. Here, Bi is a heavier element than Te (nucleon numbers: 209-Bi and 130-Te) and thus scatters more electrons. The formation of quintuple layers with alternating atomic Te-Bi-Te-Bi-Te layers is nicely resolved with a dark Te-Te interface. The amorphous Te layer at the interface to the dark appearing Si substrate is seen as line. A clearer illustration of the atomic layering is provided by plotting the intensity along a line scan. This is shown in Fig. 6 (b) on the right-hand side, for the highlighted area across the interface. It confirms the atomic resolution and the assembly [73]. In Fig. 6 (c) two different domains, being mirror symmetric to each other, can be seen. In the early growth process both domains are present, separated by vertical and horizontal boundaries. As the thickness increases, one domain is often overgrown by the other, leading to a uniform growth. The orientation of domains and the alignment between substrate and film is measured with X-ray diffraction (XRD). Trigonal islands, oriented along the axes of high symmetry and with step heights of quintuple layers, are found in all samples by atomic force microscopy (AFM), but less pronounced in Bi_2Te_3.

Besides pure Bi_2Te_3 and Sb_2Te_3, ternary films $(Bi_{1-x}Sb_x)_2Te_3$ [78, 79] are grown in a similar way. For the Bi_2Te_3/Sb_2Te_3 heterostructures [77, 80], Bi_2Te_3 is used as basic layer since it grows smoother due to a higher mobility and the upper Sb_2Te_3 film adapts the growth properties of Bi_2Te_3. The crystalline

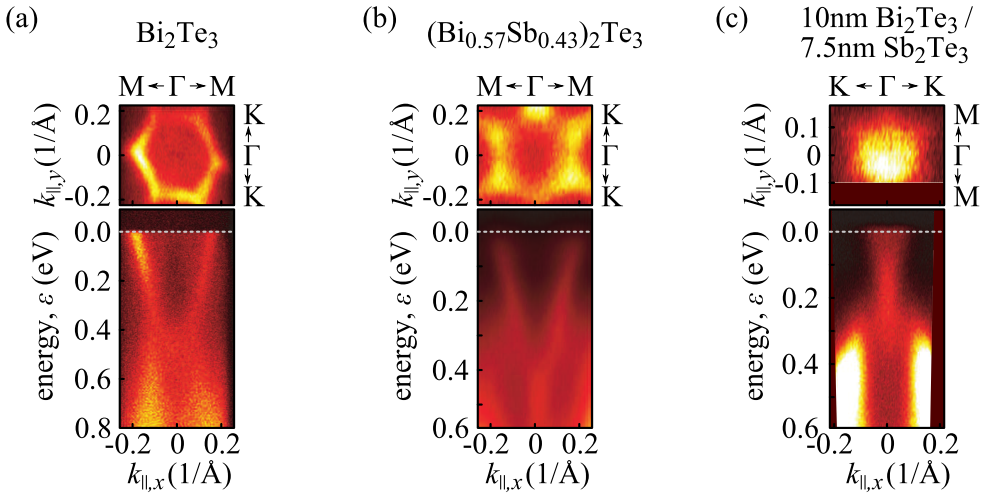

Figure 7: Angle resolved photoemission spectroscopy of (a) Bi_2Te_3, (b) $(Bi_{0.57}Sb_{0.43})_2Te_3$, and (c) 10 nm Bi_2Te_3/7.5 nm Sb_2Te_3 heterostructure. Upper panels show Fermi surface along Γ-M and Γ-K direction. Lower panels show energy dispersion along (a)-(b) Γ-M or (c) Γ-K direction. Adapted from Ref. [47].

quality is checked with HAADF measurements, showing that the interface is only two quintuple layers wide [77].

For photocurrent experiments, the energy dispersion and the position of the Fermi level is of interest in order to understand the origin of the photocurrent formation and possible optical transitions. Therefore thin films with different Fermi level positions are studied. The Fermi level with respect to the Dirac point is controlled by the Sb concentration in the ternary materials $(Bi_{1-x}Sb_x)_2Te_3$ or by the thickness of the Bi_2Te_3/Sb_2Te_3 layers [80]. To control and monitor the position of the Fermi level, angle resolved photoemission spectroscopy (ARPES) measurements are performed in collaboration with the group of Dr. Lukasz Plucinski/Prof. Dr. Claus M. Schneider at the Peter Grünberg Institut, Forschungszentrum Jülich [74, 79–82]. A measurement of pure Bi_2Te_3 is shown in Fig. 7 (a), where the lower panel depicts the energy dispersion along the Γ-M direction for binding energies down to 0.8 eV. The presence of the Dirac cone indicates that Bi_2Te_3 is *n*-type. In the upper panel a measurement of the Fermi surface is shown along the Γ-M and Γ-K direction. Hexagonal warping is typical for this material and reflects the C_{3v} symmetry [28, 83]. In *n*-type Bi_2Te_3 and *p*-type Sb_2Te_3 a large bulk carrier concentration is present. One approach to reduce the influence of the bulk is to grow ternary $(Bi_{1-x}Sb_x)_2Te_3$ systems [78, 79]. From transport measurements a reduced bulk conductivity is found for Sb concentrations of x = 0.35...0.45. ARPES measurements of a $(Bi_{0.57}Sb_{0.43})_2Te_3$ sam-

Sample	ε_F (meV)	v_F (10^5 m/s)
Bi_2Te_3	500	4.3
Sb_2Te_3	- 100	3.1
$(Bi_{0.57}Sb_{0.43})_2Te_3$	500	5.1
$(Bi_{0.06}Sb_{0.94})_2Te_3$	7	3.8
10 nm Bi_2Te_3 / 6.6 nm Sb_2Te_3	145	4.8
10 nm Bi_2Te_3 / 7.5 nm Sb_2Te_3	140	5.2
10 nm Bi_2Te_3 / 15.5 nm Sb_2Te_3	30	2.2
10 nm Bi_2Te_3 / 25 nm Sb_2Te_3	- 35	2.5

Table 1: Bi_2Te_3- and Sb_2Te_3-based TI samples used in experiments with sample composition, distance of Dirac point to Fermi energy, denoted as ε_F, and Fermi velocity v_F of linear dispersion surface state, obtained from *in-situ* ARPES measurements.

ple, presented in Fig. 7 (b), shows that indeed no bulk states are present at zero-energy, which corresponds well with the reduced bulk conductivity from transport measurements. The *n*-type Dirac cone reveals that surface pining bends the dispersion downwards. Further ARPES measurements of ternaries with higher Sb concentrations demonstrate that the Dirac point crosses the zero-energy line at x = 0.94 (data not shown) [78]. Similar results are found by Zhang *et al.* [84], in their materials with the Dirac cone being *n*-type at x = 0.94 and *p*-type at x = 0.96.

To overcome the problem of ternaries materials, which cannot have a reduced bulk carrier concentration and at the same time an intrinsic Dirac cone, heterostructures are grown [77, 80]. With a fixed Bi_2Te_3 and variable Sb_2Te_3 thickness this becomes possible. ARPES measurements performed on heterostructures with a Bi_2Te_3 thickness of 6 nm show that for thick Sb_2Te_3 layers, e.g. 25 nm, bulk states are present near the surface, and the Dirac point lies, as in pure Sb_2Te_3, above the Fermi energy (*p*-type). At a thickness of 15 nm the Dirac point intersects the Fermi energy and no bulk states are present at zero-energy. For thinner layers (6 - 15 nm) a single Dirac cone is visible (*n*-tpye) [80]. The change of the charge carrier type is confirmed by transport measurements, which show a change in the Hall slope between 6 and 17 nm [77]. The band structure is shown by ARPES measurement in Fig. 7 (c) for a 10 nm Bi_2Te_3/7.5 nm Sb_2Te_3 heterostructure.

Table 1 gives an overview of all used samples. Besides the sample composition, the distance between the Dirac point and the Fermi energy, simply de-

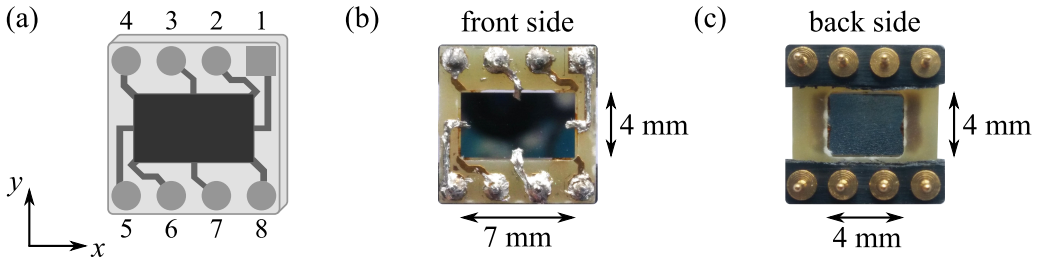

Figure 8: (a) 8 pin sample holder with Cartesian coordinates x, y and contact numbers. (b) Picture of Bi_2Te_3 sample in holder used for electrical measurements. (c) Notch in sample holder enables illumination of back side, e.g. of Bi_2Te_3.

noted as ε_F, is given together with the Fermi velocity v_F of the linear dispersion surface states. Both values are obtained from *in-situ* ARPES measurements.

XRD measurements are performed to determine the axes of high symmetry. The samples are cut along high symmetry direction into pieces of 7×4 mm^2 or along random direction into pieces of 5×5 mm^2. Several samples of the same composition are studied, and are listed under the same name. Finally, the sample pieces are mounted into sample holders and electrically contacted by pure Indium. The corresponding contact numbers together with the Cartesian coordinates used in the experiments are shown in Fig. 8 (a). A picture of a Bi_2Te_3 sample is shown in Fig. 8 (b). Note that for some experiments it is necessary to excite the samples also from the backside, why a notch of 4×4 mm^2 is cut into the holder, see Fig. 8 (c).

3.1.2 Graphene

Besides 3D TIs, high mobility graphene samples are studied. The Hall bar structured samples were produced in collaboration with the group of Dr. Jonathan Eroms/Prof. Dr. Dieter Weiss at the University of Regensburg.

To fabricate high mobility graphene samples, exfoliated graphene flakes are caped by hexagonal boron nitride (h-BN). The latter is an ideal substrate for graphene [85], since it is a dielectric insulating isomorph of graphite, with B and N atoms forming two sublattices, and has only a small lattice mismatch of 1.7%. Due to strong in-plane ionic bonds no surface charge traps or dangling bonds are present. Furthermore, it is atomically planar and graphene does not ripple. To fabricate Hall bar structures, exfoliated graphene flakes are picked up by van der Waals interaction with a h-BN flake and transferred onto a second h-BN flake on a SiO_2 substrate, see Fig. 9 (a). The h-BN/graphene/h-BN stack is annealed and patterned into Hall bar shape by electron beam

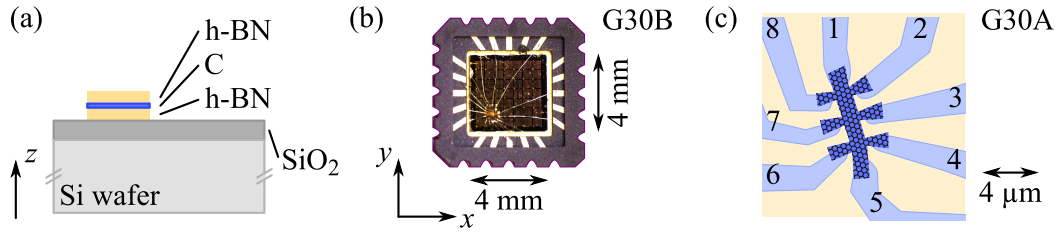

Figure 9: (a) Sample geometry: On a Si wafer followed by SiO_2, h-BN/graphene/h-BN stack is transferred. (b) Picture of graphene sample G30B in 20 pin sample holder used for measurements together with Cartesian coordinates x, y. (c) Hall bar shape of sample G30A together with contact numbers.

lithography and reactive ion etching. Cr/Au contacts are made with electron beam lithography and deposited with thermal evaporation and lift-off. A more detailed description of the procedure can be found in Ref. [86].

The samples are glued into chip carriers (8×8 mm^2, 20 pin) with silver filled epoxy to contact the back-gate and then electrically wire-bonded, see Fig. 9 (b). In panel (b) the orientation within the Cartesian coordinate system of the experimental setup is shown. The contact numbers and the Hall bar shape is shown in Fig. 9 (c).

To characterize the samples, magneto-transport measurements are performed. They revealed that by using h-BN embedded graphene flakes high mobilities μ in the range 35 000 to 99 000 cm^2/Vs are realized. Note that with graphene on SiO_2 substrates only several thousand cm^2/Vs are usually achievable [85]. Additional the carrier density p, the Fermi wave vector k_F, and the Fermi energy ε_F are calculated. The values for the three samples studied (G30A, G30B, and G31A) are shown in Tab. 2. Application of $U_G \approx \pm 4$ V to the back gate, switches the type of carriers from holes to electrons. By varying the back gate voltage the charge neutrality point (CNP) is detected at a voltage of $U_G \approx 1$ V. Since the CNP position U_{CNP} can be shifted slightly by different sample cool-downs, a normalized gate voltage $U_G^{eff} = U_G - U_{CNP}$ is

Sample	p (10^{10} cm^{-2})	k_F (10^6 cm^{-1})	ε_F (meV)	μ (cm^2/Vs)
G30A	8.0	0.5	33	35 000
G30B	4.2	0.36	24	99 000
G31A	4.6	0.38	25	68 000

Table 2: Characteristics of graphene samples G30A, G30B and G31A, obtained at 4.2 K from magneto-transport at zero back gate voltage.

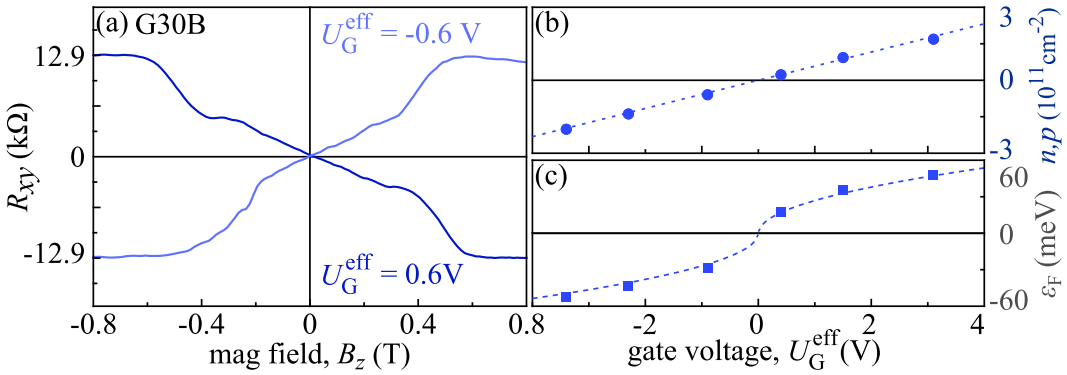

Figure 10: Magneto-transport of sample G30B: (a) Transverse resistance for applied back gate voltage of $U_G^{eff} = \pm 0.6$ V showing plateaus with filling factor 2 ($R_{xy} = h/2e^2 = 12.9$ kΩ) above $B_z \approx 0.5$ T. For negative back gate voltages, the Hall slope is negative (holes), for positive voltages it is positive (electrons). Panel (b) shows carrier densities n, p and panel (c) Fermi level positions ε_F.

used. Figure 10 (a) shows magneto-transport measurements of the transverse resistance in sample G30B for two effective gate voltages corresponding to p and n conductivity, for applied back gate voltages of $U_G^{eff} = \pm 0.6$ V. The data reveal a pronounced quantum Hall effect, in which the $h/2e^2 = 12.9$ kΩ plateau is reached for small carrier densities below $B_z \approx 0.8$ T. For this plateau the Fermi level ε_F lies between the first Landau level and the one at zero-energy. The variation of the carrier density n, p and the Fermi energy ε_F as a function of effective gate voltage is shown in Fig. 10 (b) and (c), respectively.

3.2 Measurement Technique

The lasers, used for exciting the samples, cover a broad frequency range from 0.6 up to 60 THz. To span over such a wide spectral range various radiation sources are used. Their characteristics and properties are described in the first part of this section. In the second part the experimental setup which includes a short description of the photocurrent measurement is explained.

3.2.1 Terahertz/Infrared Laser Radiation

Photocurrent measurements are carried out with different laser sources in the near, mid, and far infrared. Most experiments are performed using THz radiation of a molecular gas laser (90 - 496 μm) and mid infrared radiation of a CO_2 laser (9 - 11 μm). Additionally, a quantum cascade laser (QCL) with a much shorter wavelength (5 μm) and a free-electron laser (FEL), covering the whole infrared range, are used.

The CO_2 Laser Appreciated for its high power, the carbon dioxide (CO_2) laser is widely used in industry for welding and cutting. Its high power, its discrete and tunable wavelength make pulsed CO_2 lasers also good candidates to induce optoelectronic phenomena in condensed matter [38, 87].

The excited a CO_2 molecule, see Fig. 11 (a), has three modes: bending, symmetric and anti-symmetric stretching. Between those levels, radiative transitions can occur, for which lasing can be accomplished. Nitrogen in the laser gas is excited by electron impact and gives its energy to the highest level of the CO_2 molecule, the anti-symmetric stretching mode. From this level radiative transitions occur to the bending mode ($\approx$ 32 THz) or to the symmetric stretching mode ($\approx$ 29 THz). These levels are emptied due to non-radiative relaxation processes. The vibrational modes are further split into rotational ones, therefore radiative transitions are possible in a wide frequency range ($\approx$ 27 to 33 THz). As it can be seen in Fig. 11 (b), optical transitions between split vibrational modes fulfil the selection rules (change of rotational quantum number $\Delta J = \pm 1$). Discrete frequencies are selected by a blazed grating.

In experiments different CO_2 laser systems are applied. Two transversely excited atmospheric (TEA) lasers operating with a repetition rate of 1 Hz in a pulsed regime are used, having an electrical discharge of about 100 kV. The pulse duration is between 100 and 200 ns. Their intensity of about hundreds of kW/cm^2, is measured with photon drag detectors as a voltage drop across a

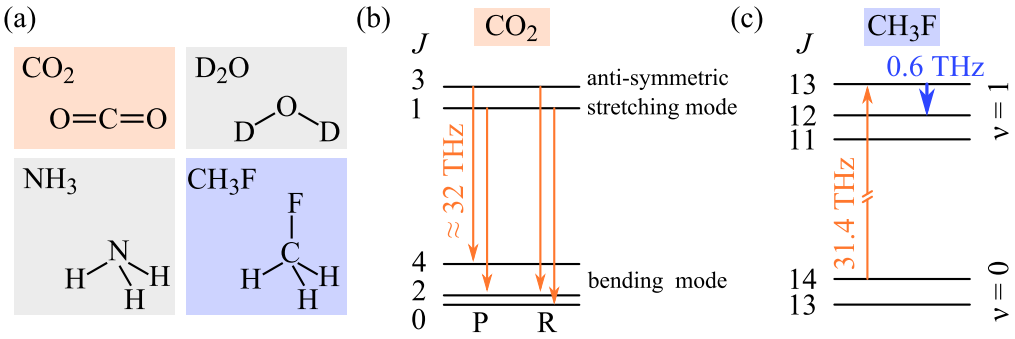

Figure 11: (a) Molecules used for generation of infrared radiation. Structural formula of (clockwise) carbon dioxide CO_2, heavy water D_2O, fluoromethane CH_3F, and ammonia NH_3. (b) Optical transitions between vibrational modes of CO_2 molecule, here from anti-symmetric stretching mode (001) to bending mode (020) with centre frequency of 32 THz. Branches P and R denote change of rotational quantum number $\Delta J = +1$ and -1, respectively. (c) Optical transitions between rotational modes of CH_3F molecule within first excited level $\nu = 1$ at 0.6 THz. Adapted from Ref. [38].

50 Ω load resistor with GHz oscilloscopes. These lasers are additionally used to optically pump the molecular gas laser.

A Q-switched laser is used to obtained stable and low power radiation. For this purpose, a mechanically rotating mirror is mounted in an extended resonator of a continuous wave CO_2 laser. It is operated with 130 to 170 Hz and has a pulse duration of about hundred nanoseconds. Its peak power is measured with Mercury Cadmium Tellurium (MCT) detectors and corresponding intensity at the sample position of tens of mW/cm^2 are recorded with a GHz oscilloscope.

The Molecular Gas Laser For the far infrared range pulsed molecular gas lasers are used [38, 87]. To obtain small photon energies in the terahertz range, transitions between different rotational modes of molecules are used. Typical molecules are ammonia (NH_3), heavy water (D_2O), or fluoromethane (CH_3F), see Fig. 11 (a). The heavier the molecules, the closer the rotational levels are and the photon energies of the optical transitions decrease. That's why with CH_3F molecules a frequency of $f = 0.6$ THz is achieved, with D_2O molecules $f = 0.78$ THz, and with NH_3 molecules different frequencies $f = 1.1$, 2.0, 3.3, and 3.9 THz. Such an optical transition is shown in Fig. 11 (c), where CH_3F is excited with a CO_2 laser line into the first excited level $\nu = 1$. This sketch reveals that not only the laser gas has to be chosen correctly, but also the optical pump frequency of the very fine tunable CO_2 laser. Laser

operation is possible even if the optical pump pulse does not fit exactly to the absorption line, since the THz radiation can be generated due to stimulated Raman scattering.

In experiments pulsed molecular gas lasers are used with a repetition rate of 1 Hz and pulse durations between 100 and 200 ns. The intensity is wavelength dependent and in the range 1-500 kW/cm^2. It is measured with photon drag detectors in the same manner as described for the CO_2 laser.

The Quantum Cascade Laser To investigate photocurrents in the near infrared range a quantum cascade laser is used. It is based on intersubband transitions in a quantum well, whereby multi quantum well structures are used to increase the gain [88].

The lasing process has three stages. First, a static electric field E_S is applied to bend the band structure and thus to drive the electrons through the system. Second, electrons are injected into an excited size quantized subband. From there optical transitions to lower levels, e.g. into the first one, are possible with corresponding photon energies in the near and mid infrared range. Last, the electrons tunnel into the next quantum well and the process starts over. Consequently, one electron *cascades* through the multi quantum well system and emits several photons. Tunnelling is possible if the quantized subbands in the first and the second quantum well are very close in energy. This type of transition is called *resonant* or *intrawell*. If those levels are not in resonance, alternatively optical transitions can take place between two neighbouring quantum wells. These transitions are called *photon-assisted* or *interwell*. Both possibilities are illustrated in Fig. 12 (a). In real structures passive regions are grown in between the lasing region to improve the performance. In those injector regions the electrons are collected. The QCL frequency is tuned by the quantum well thickness and not by the materials band gap.

In the experiments a single line QCL is used operating at a frequency of 58.8 THz. The continuous wave laser is optically chopped at a frequency of about 170 Hz. The peak power is measured with MCT detectors and recorded with lock-in technique. Typical intensities are hundreds of mW/cm^2 range.

The Free-Electron Laser A laser which can cover the whole infrared range is the free-electron laser (FEL) [38, 87]. For its operation relativistic electrons are needed, e.g. provided by a linear accelerator. Together with the large scaling of the FEL itself, it is expensive and only operated by some institutes.

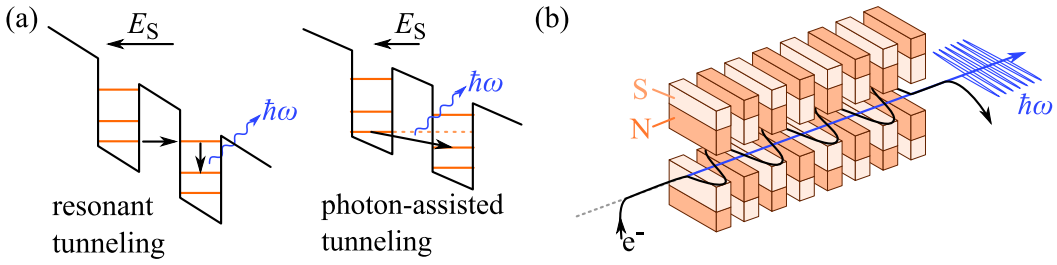

Figure 12: (a) Optical transitions in multi quantum well structures between size quantized subbands. Resonant intrawell transitions on left, photon-assisted interwell transitions on right. (b) Path of relativistic electron beam in a magnet array of a free-electron laser with alternating magnetic field directions, leading to emission of infrared synchrotron radiation. Adapted from Refs. [38, 87].

Therefore, not all measurements are performed with this laser, only in the frequency range not accessible by the lasers described above.

Propagating at constant velocity (fractions of c), electrons are deflected on a sinusoidal path by a periodic array of magnets with alternating field directions, see Fig. 12 (b). In the trajectories the electrons are accelerated radially and emit synchrotron radiation. The emitted spectrum can be continuous (wiggler) or can have discrete frequencies (undulator). Relativistic corrections, namely relativistic reduction, Thomson scattering, and Doppler shift, increase the frequency of the spontaneously emitted radiation. Therefore, the corresponding wavelengths are in the micrometer range and much shorter than the wiggler/undulator distance being in the centimetre range.

The spontaneously emitted synchrotron radiation can interact with the electron beam. For certain conditions, the electrons are further location dependent accelerated or decelerated by the radiation (micro-bunching). If this process is driven slightly out of phase, the electrons can give energy to the radiation. The FEL can operate without an external resonator in a mirror-less regime, where self-amplified spontaneous emission radiation is obtained in a single-pass. To increase the efficiency, systems can be operated in stimulated emission regime with an external resonator.

Experiments are performed at the free-electron lasers (FELBE) at the Helmholtz-Zentrum in Dresden-Rossendorf (HZDR). The used FELs, operated with the undulators U100 and U27, cover the frequency ranges from 1.2 to 16 THz and 12 to 99 THz, respectively. Operating in a quasi-continuous wave regime, optical choppers (170 Hz) are used to modulate the radiation. Peak powers are measured with MCT detectors using lock-in technique and corresponding intensities are in W/cm^2 range.

3.2.2 Experimental Setup

To induce photocurrents in Bi_2Te_3- and Sb_2Te_3- based thin films and graphene the terahertz/infrared radiation, provided by the laser systems described above, is focused by parabolic mirrors onto the samples. The spatial beam profile of the laser radiation is checked with a pyro-electrical camera. All laser sources have an almost fundamental Gaussian beam profile, see Fig. 13 (a) for a frequency of $f = 3.3$ THz, provided by the molecular gas laser and most used in experiments. From these measurements the half widths at half maximum (HWHM) is read out for the x and y direction, and the area factor A_{factor} is calculated, defined as $A_{\text{factor}} = 1/(\pi\,\text{HWHM}_x \times \text{HWHM}_y)$ being in the order of tens of cm^{-2}.

To record the laser power, a reference signal is partially reflected by a beam splitter onto a photon drag or MCT detector. The laser intensity at the sample position is calculated with the area factor A_{factor} and the reference signals using calibration measurements, where the sample is replaced by a second detector. Depending on the laser source, the intensity on the sample has hundreds of kW/cm^2 for the pulsed molecular gas and CO_2 lasers and in the mW/cm^2 range for the (quasi) continuous wave Q-switched CO_2, the QCL, and the FEL lasers. To change the laser intensity at the sample position attenuators are used. Depending on the frequency range, germanium (Ge) or calcium fluoride (CaF_2) plates are used for the near and mid-infrared and teflon for the far infrared [38].

The polarization is controlled by wave plates or Fresnel rhombs. To obtain elliptically polarized radiation, quarter wave plates or quarter wave Fresnel rhombs are used. Their rotation is described by the angle φ. At angles $\varphi = 0, 90°$ and $180°$ the linear polarization remains unchanged. At angles $\varphi = 45°$ and $135°$ the radiation becomes left or respectively right handed circularly polarized. To rotate the linear polarization, a grid wire is rotated behind a quarter wave Fresnel rhomb set to $\varphi = 135°$ or $45°$ to obtain circularly polarized radiation or, if available, half wave plates are used. The rotation of linear polarization is denoted by the angle α. In all experiments the rotational direction of α and φ on the sample is counter clockwise, see Fig. 13 (b).

Just like the measurement of the reference signals, terahertz/infrared radiation induced photocurrents are measured as a voltage drop across load resistors, see Fig. 13 (b), with GHz oscilloscopes or lock-in technique. Preamplifieres with amplification factors of 100 or 200 are used to enhance small

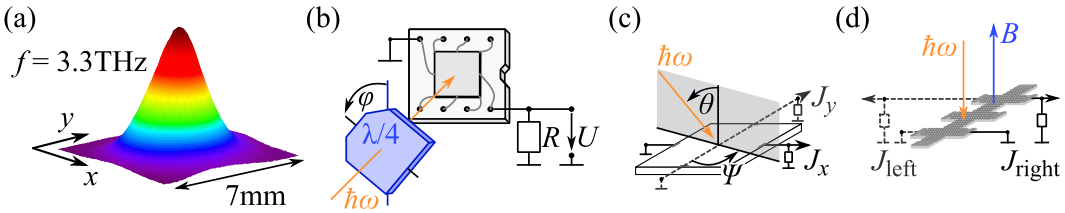

Figure 13: (a) Beam profile measured at 3.3 THz with a pyro-electrical camera. Half width at half maxima both in x and y direction is about 0.25 cm, corresponding to an area factor of 20 cm^{-2}. (b) Experimental setup. Photocurrent signal is measured as voltage drop across load resistor. Radiation polarization is varied with wave plates, here quarter wave plate. Rotation is defined by φ. The rotation of the linear polarization by half wave plates is defined as α. (c) Angle of incidence is defined as θ. Usually the middle of the sample is irradiated. Edges or contacts are not illuminated, unless remarked otherwise. Adapted from Ref. [38].

signals or to measure differentially simultaneously along different directions, e.g. along x and y direction or at opposite edges, denoted as J_{left} and J_{right}. Experiments on Bi_2Te_3- and Sb_2Te_3-based three dimensional topological insulators are performed under several angles of incidence, denoted by θ, whereby $\theta = 0$ corresponds to normal incident. The rotation of the plane of incidence is denoted as Ψ, see Fig. 13 (c). If not further noted, the plane of incidence is lying in the (yz) plane at $\Psi = 0$. Experiments on graphene are performed at normal incidence only.

Several photocurrent measurements are performed on samples at room temperature. For low temperature measurements different optical cryostat systems are used. Radiation is coupled into the cryostats through z-cut quartz windows in the far infrared range and through zinc selenide (ZeSe) windows in the mid infrared. Due to their low helium consumption and easy handling, continuous-flow cryostats are used for temperature dependences at zero magnetic field. For experiments on graphene and magneto-transport measurements optical bath and variable temperature cryostat systems are used. In those cryostats, operated at liquid He temperature $T = 4.2$ K, split coil magnets provide magnetic fields up to ± 5 T. The magnetic field is applied in Faraday geometry, i.e. normal to the sample surface and parallel to the radiation propagation direction, see Fig. 13 (d).

4 Photocurrents in Bi_2Te_3- and Sb_2Te_3-based Three Dimensional Topological Insulators

In this chapter experiments on Bi_2Te_3- and Sb_2Te_3-based three dimensional topological insulators are presented. In the first section photocurrents excited at normal incidence with linearly polarized terahertz radiation are discussed. The second one deals with photocurrents excited at oblique incidence. The photocurrent in these two sections are treated semi-classically, in contrast to the last section, which presents photocurrents excited with the highest frequencies used and with circularly polarized radiation. The results presented are published in Refs. [45–47].

4.1 Photocurrents Excited at Normal Incidence

Before discussing the experimental results, the phenomenological theory for photocurrents in Bi_2Te_3- and Sb_2Te_3-based 3D TIs is addressed. Following Sec. 2.2, two effects scaling quadratically with the radiation electric field, are allowed: the photogalvanic effect, Eq.(24) and the photon drag, Eq.(32). The symmetry analysis explores the macroscopic behaviour of the photocurrents and helps to choose the experimental geometry. While the bulk of Bi_2Te_3 and Sb_2Te_3 belongs to the centrosymmetric D_{3d} point group symmetry, which includes the inversion centre, the surface misses the space inversion and belongs to the point group C_{3v}. Consequently, the photon drag effect is allowed in both, the bulk and the surface states, whereas the photogalvanic effect is only allowed in the surface states. Considering these symmetries, the phenomenological equations, see Eq.(22), are given for currents probed along the crystallographic directions x_0 and y_0, see Fig. 2, at normal incidence as

$$\begin{aligned} j_{x_0} &= (\chi + Tq_z)(|E_{x_0}|^2 - |E_{y_0}|^2) = -(\chi + Tq_z)E_0^2 \cos(2\alpha), \\ j_{y_0} &= -(\chi + Tq_z)(E_{x_0}E_{y_0}^* + E_{y_0}E_{x_0}^*) = (\chi + Tq_z)E_0^2 \sin(2\alpha), \end{aligned} \tag{39}$$

in which χ is the photogalvanic coefficient and T the photon drag coefficient, see Sec. 2.2.2. The Stokes parameters for linearly polarized radiation are given as $s_1 = -\cos(2\alpha)$ and $s_2 = -\sin(2\alpha)$, with the azimuthal angle α denoting the direction of the electric field vector. Equation (39) reveals that the excitation of the surface states by normal incident radiation causes a direct current, which scales quadratically with the radiation electric field and exhibits characteristic

polarization dependencies. The polarization dependencies are identical for the photogalvanic and the photon drag effect. The effects can be distinguished since the photogalvanic effect is solely driven by the in-plane electric field orientation, whereas the photon drag effect is also proportional to the photon momentum. Thus, the photon drag effect changes its sign for front and back illumination in the experiments, while the photogalvanic effect is independent. The above consideration are based on a very general symmetry argument and allows to make a convincing conclusion on the photocurrent origin.

4.1.1 Experimental Results

By irradiating Bi_2Te_3- and Sb_2Te_3-based thin films with normal incident linearly polarized terahertz radiation at room temperature a photocurrent is observed [44–47]. The photocurrent amplitude depends on the orientation of the electric field vector of the incident laser radiation α. This is exemplarily shown for Bi_2Te_3 in Fig. 14 (red dots) for the normalized photocurrents measured along the x, panel (a), and y direction, panel (b). The data are well fitted by

$$\begin{aligned} J_x/I &= -A\cos(2\alpha) + C_x, \\ J_y/I &= A\sin(2\alpha) + C_y \end{aligned} \tag{40}$$

in which $C_{x,y}$ are the fit parameters for the polarization independent offset, A the fit parameter for the polarization dependent contribution, and $s_1 = -\cos(2\alpha)$ and $s_2 = -\sin(2\alpha)$ are the Stokes parameters of light. The polarization dependence corresponds to the one discussed in Eq.(39), the only difference is the small polarization independent offset, which can be caused by local symmetry reduction due to non-perfectly flat surfaces or surface roughness.

This overall behaviour is the same for all samples used, see Tab. 1 in Sec. 3.1.1, and for all radiation frequencies f used. The frequency dependence of the photocurrent is discussed later. The photocurrents observed increase linearly with the increase of the radiation intensity I. This is shown in Fig. 14 (c) for Bi_2Te_3 at an excitation frequency of $f = 2.0$ THz. The radiation intensity I is normalized to the value obtained without attenuators. Also, the photocurrent amplitude J is normalized to the value at maximal intensity. Individual photo-signal pulses, U_{sample}, follow the temporal structure of the excitation pulse, U_{ref}, closely with a response time of picoseconds or less, see

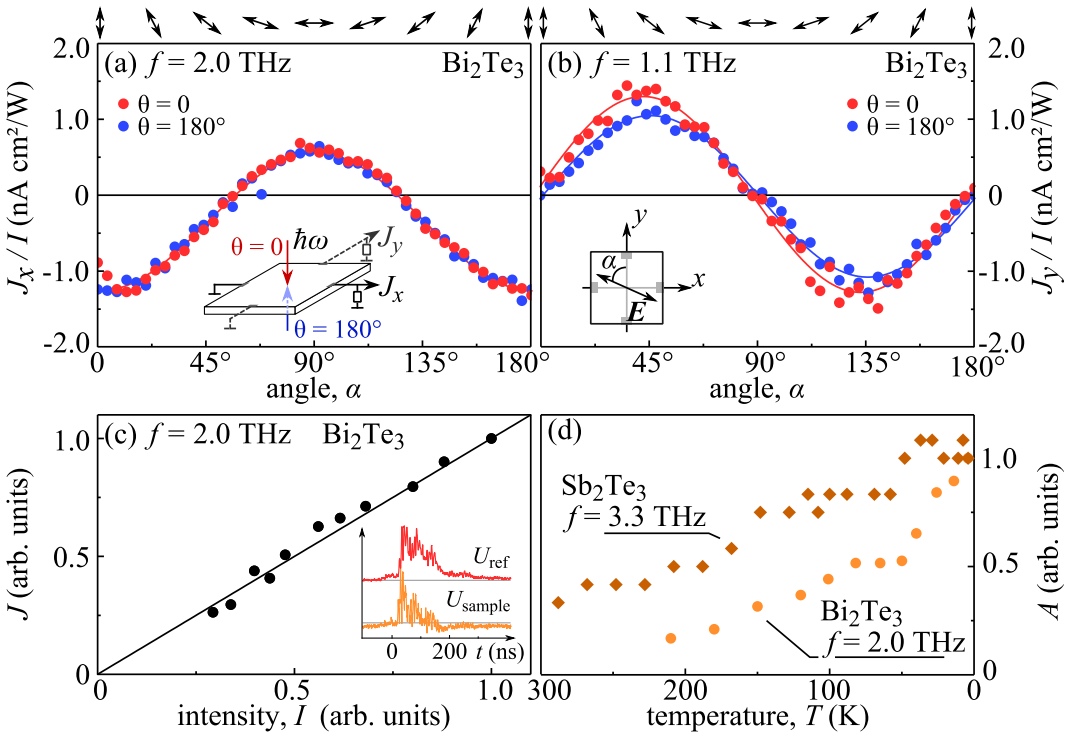

Figure 14: Dependence of normalized photocurrent J/I on orientation of radiation electric field vector, in Bi_2Te_3 measured along (a) x direction with radiation frequency $f = 2.0$ THz and along (b) y direction with radiation frequency $f = 1.1$ THz. Red dots correspond to normal incident radiation, $\theta = 0$, and blue dots to back illumination, $\theta = 180°$. Insets show measurement geometry. Arrows on top of both panels illustrate states of polarization for several angles α. Fits after Eq.(40) and Eq.(39). (c) Normalized dependence of photocurrent J on radiation intensity I. Inset shows temporal structure of photo-signal, U_{sample}, and excitation pulse, U_{ref}. (d) Temperature dependence of polarization dependent contribution to photocurrent in Bi_2Te_3 and Sb_2Te_3, measured at $f = 2.0$ and 3.3 THz, respectively. All data are normalized to value for $T = 4.2$ K. Adapted from Ref. [47].

inset in Fig. 14 (c).

Cooling the samples from room temperature to $T = 4.2$ K increases the normalized photocurrent. This is shown in Fig. 14 (d) for Bi_2Te_3 and Sb_2Te_3 samples, excited at $f = 2.0$ and 3.3 THz, respectively. The amplitude A is normalized on the values at $T = 4.2$ K. The overall behaviour like the temporal pulse shape, intensity or polarization dependencies remains the same.

The photocurrent is observed also by illuminating the sample backside ($\theta = 180°$), shown in Fig. 14 (a) and (b) with blue dots. For back illumination the photocurrent dependence on the polarization does not change and the amplitude A remains the same. For some samples and excitation frequencies, however, the magnitudes of A for front and back illumination differ. An ex-

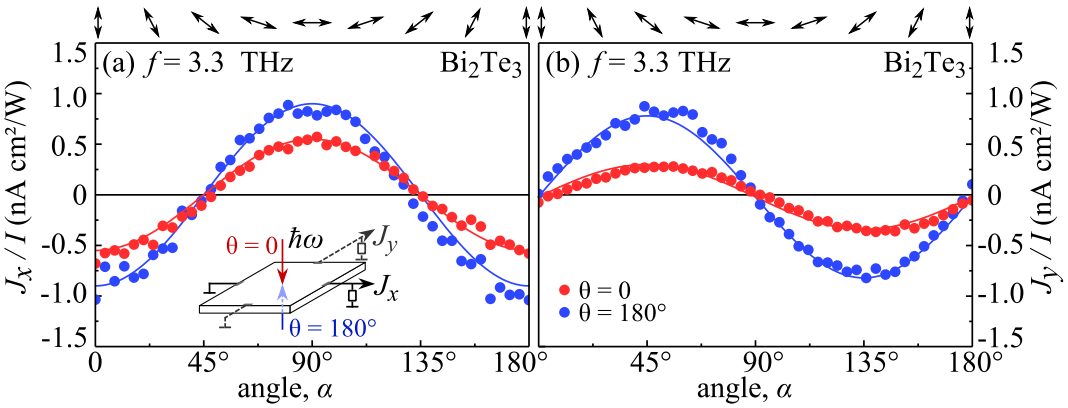

Figure 15: Dependence of normalized photocurrent J/I on orientation of radiation electric field vector in Bi_2Te_3 measured along (a) x and (b) y direction with radiation frequency $f = 3.3$ THz. Red dots correspond to normal incident radiation, $\theta = 0$, and blue dots to back illumination, $\theta = 180°$. Inset shows measurement geometry. Arrows on top of both panels illustrates states of polarization for several angles α. Fits after Eq.(40) and Eq.(39). Adapted from Ref. [47].

ample for an increased amplitude A at $\theta = 180°$ is shown in Fig. 15 for Bi_2Te_3 excited at $f = 3.3$ THz. For both photocurrent directions J_x/I and J_y/I the normalized photocurrent measured at $\theta = 180°$ is almost one third larger then the one for $\theta = 0$.

As it is shown in Eq.(39) and the following discussion, the polarization dependence of the photogalvanic effect is not affected by reversing the radiation propagation direction. The photon drag current, however, changes it sign. This is experimentally examined by measurements using front and back illumination, which indicate that the photogalvanic effect is dominating at normal incidence and that the photon drag effect has only a minor contribution, since the amplitude A never changes sign. This result is not only obtained for Bi_2Te_3, but for all samples studied, see Tab. 1.

Photocurrents at normal incidence are observed in the frequency range studied from $f = 0.6$ to 60 THz. For all samples and all frequencies the overall behaviour, like the dependence on the azimuthal angle α and the linear dependence on the radiation intensity I is the same. Also, the sign of the amplitude is unaffected for front and back illumination.

Now the dependence of the photocurrent amplitude on the excitation frequency is shown. Figure 16 illustrates the variety, but also the similarities of the frequency dependence of the photocurrent, for the selected samples Bi_2Te_3, $(Bi_{0.57}Sb_{0.43})_2Te_3$, $(Bi_{0.06}Sb_{0.94})_2Te_3$, and 10 nm Bi_2Te_3/15 nm Sb_2Te_3

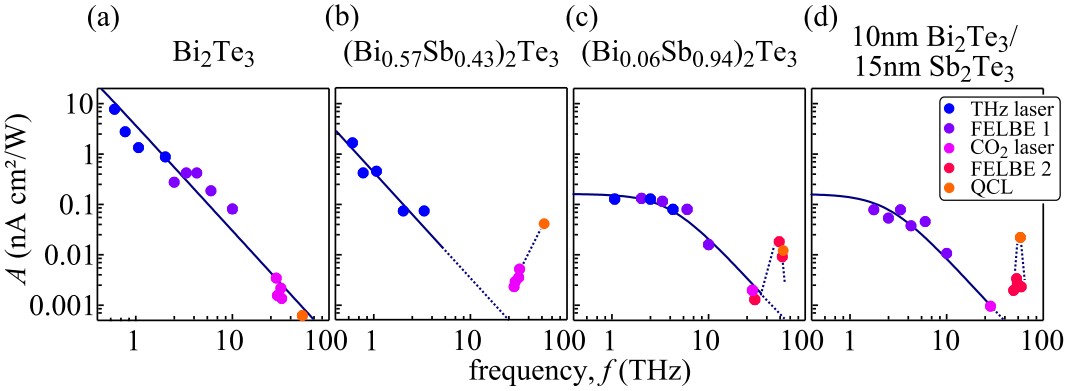

Figure 16: Dependence of A on radiation frequency f for (a) Bi_2Te_3, (b) $(Bi_{0.57}Sb_{0.43})_2Te_3$, (c) $(Bi_{0.06}Sb_{0.94})_2Te_3$, and (d) a 10 nm Bi_2Te_3/ 15 nm Sb_2Te_3 heterostructure. Solid lines show fit after Eq.(41), for theory see Eq.(54). Dots in different colour correspond to different laser sources, see Sec. 3.2.1. The molecular gas laser and the FELs U100/U27 are shortened as THz laser and FELBE 1/2, respectively. Note that deviation from fit is discussed in Sec. 4.3. Dashed lines are guide for eye, demonstrating deviation of photocurrent amplitude from Drude-like behaviour. Adapted from Ref. [45].

heterostructure. The frequency dependence is well fitted by

$$A = t_{\text{exp}}^2/[1 + (2\pi f t_{\text{exp}})^2], \tag{41}$$

where t_{exp} is a fit parameter. In a wide range of frequencies the photocurrent decreases with a frequency increase and scales as power law, fitted by $1/f^2$. This is well described by Eq.(41) for the case $(2\pi f t_{\text{exp}}) \gg 1$, see Fig. 16 (a) and (b). In Fig. 16 (c) and (d) two examples for the exact fit after Eq.(41) are shown.

At higher frequencies a deviation from the frequency dependence, described by Eq.(41), is observed for some samples. The photocurrent in this frequency range can be more than two orders of magnitude larger than that one expected from the fit. In the studied frequency range, the photocurrent increases, see Fig. 16 (b), and for some samples, after reaching a maximum, decrease again, see Fig. 16 (c) and (d). The exact shapes differ from sample to sample and is not resolved accurately due to the use of discrete frequencies available in the experiments. This does not allow to determine the shape or the peak width. This section is focused on the results corresponding to the frequency behaviour described in Eq.(41). The deviation at higher frequencies is discussed in Sec. 4.3.

The measurements show that, the photocurrent direction is determined by

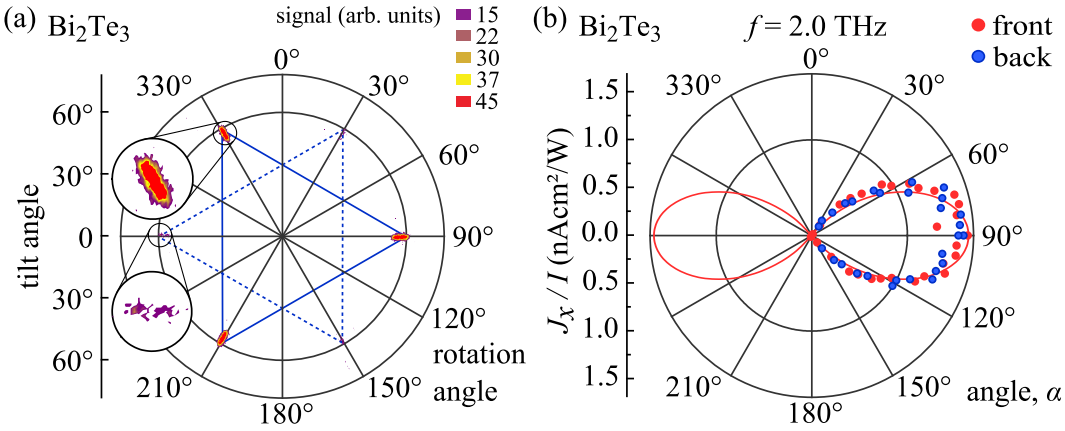

Figure 17: (a) X-ray diffraction pole figure scan of a Bi_2Te_3 sample, showing presence of two domains being mirror symmetric to each other. One domain (highlighted by solid blue line) dominates. The data reveal that crystallographic axes lie parallel to sample edges, i.e. $\Phi = 0$. (b) Normalized photocurrent J_x/I in same Bi_2Te_3 sample, measured for front $\theta = 0$ and back $\theta = 180°$ illumination, in red and blue data points, respectively. Solid lines show fits after Eq.(40). Adapted from Ref. [47].

the orientation of the electric field vector with respect to the x and y directions. However, a more careful analysis shows that also the orientation of the crystallographic axes x_0 and y_0 is of importance. They are shown for Bi_2Te_3- and Sb_2Te_3-based3D TIs in Fig. 2 in Sec. 3.1.1, whereby one lies perpendicular and one along a mirror reflection plane of the C_{3v} point group.

Most samples are first characterized by XRD and then cut along the crystallographic directions x_0 and y_0. The XRD measurements reveal the directions of high reflection and confirm the three-fold symmetry of the material, see Fig. 17 (a) for a Bi_2Te_3 sample. Moreover, the plot shows the presence of two domains. One domain is predominant, highlighted by a blue solid line, and has maximal intensities for angles 90°, 210°, and 330° with respect to the x direction, in which the photocurrent is probed. The suppressed domain is mirror symmetric to the other one and has maxima of intensity for angles 30°, 150°, and 270°. The intensity ratio between the dominant domain and the suppressed one is 3.5. For such samples the photocurrent is fitted by Eq.(40). The maximum photocurrent measured in x direction corresponds to $\alpha = 90°$, which is shown in a polar plot in Fig. 17 (b) for Bi_2Te_3 and a radiation frequency of $f = 2.0$ THz.

For some samples, however, the crystallographic directions x_0 and y_0 do not correspond to the coordinates x and y, along which the current is probed. In samples, that are cut along a random direction from wafers, a misalignment Φ between both is observed. The corresponding XRD measurements for a Sb_2Te_3

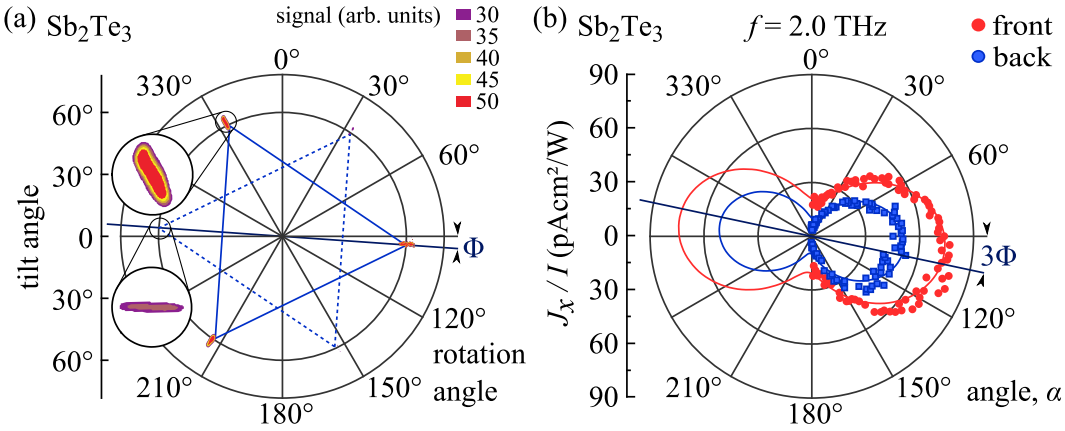

Figure 18: (a) X-ray diffraction pole figure scan of a Sb_2Te_3 sample, showing presence of two domains being mirror symmetric to each other. One domain (highlighted by solid blue line) dominates. The data reveal that crystallographic axes x_0, y_0 are rotated by $\Phi = -4°$ with respect to samples edges oriented along x, y directions. (b) Normalized photocurrent J_x/I in same Sb_2Te_3 sample, measured for front $\theta = 0$ and back $\theta = 180°$ illumination, in red and blue data points, respectively. Solid lines show fits after Eq.(40). The dependencies reveal that photocurrent is shifted by $-12°$. Adapted from Ref. [44].

sample is shown in Fig. 18 (a). The XRD data confirm the three-fold symmetry and presence of twisted domains with an intensity ratio between the dominant and the suppressed domain of 1.6. In this Sb_2Te_3 sample the maximum value of the photocurrent is not measured at $\alpha = 90°$, but at $\alpha = 102°$ and a phase shift in the photocurrent is observed, see Fig. 18 (b).

4.1.2 Discussion

As addressed above, two effects, the photon drag and the photogalvanic, see Eq.(39), can be the cause for the photocurrent. Experiments using front and back illumination are a clear evidence for the photogalvanic effect as the photocurrent origin, since the amplitude A never changes sign for front and back illumination. Indeed, for the reversed radiation propagation direction $z \to -z$, the photon momentum direction $q_z \to -q_z$ changes, while the in-plane electric field components $E_{x,y}$ are unaffected. All experiments performed in the frequency range from 0.6 to 60 THz reveal that the sign of the photocurrent does not change at back illumination and that the photogalvanic effect dominates the current formation. Contributions of the photon drag effect, even being small, cannot be excluded completely, as the amplitude A has under some conditions different values for front and back illumination. This variation may additionally be affected by the unequal photocurrent contributions

excited in the top and interface surfaces separated by the bulk material, e.g., due to different scattering times.

The photogalvanic effect, being dominant at normal incidence, is allowed only in the surface states in centrosymmetric Bi_2Te_3- and Sb_2Te_3-based 3D TIs. Its microscopic origin is discussed in the following by a model and a theory. At the end of the discussion shortly the microscopic theory for the photon drag effect, having only a minor contribution, is given.

Optical transitions are identified by comparison of the photon energy and the Fermi energy ε_F. The latter is obtained from *in-situ* ARPES measurements, examples are shown in Fig. 7 in Sec. 3.1.1. In a wide frequency range, especially in the lower THz range, the photon energy is much smaller than the Fermi energy of the materials studied and the relation $\hbar\omega \ll \varepsilon_F$ yields. For this condition, only intraband transitions are possible and Drude-like free carrier absorption dominates. In this regime, the current formation can be treated with a semi-classically approach.

Microscopic Model of the Photogalvanic Effect High frequency second order effects can be caused by the redistribution of excited, quasi free, carriers in momentum space. The redistribution is treated with a non-equilibrium distribution function, which contains oscillating in time and space contributions, as well as static ones. Consequently, direct as well as alternating currents can be induced by high frequent radiation. A requirement for a direct current is an asymmetric redistribution in momentum space. This can be fulfilled for example with asymmetric scattering processes, as discussed in Sec. 2.2.2 for type-II quantum wells.

For the considered Bi_2Te_3- and Sb_2Te_3-based thin films carriers can scatter for example on phonons or Coulomb impurities. The three-fold symmetry of the material makes this elastic scattering process asymmetric. This scattering anisotropy can be sketched as double point symmetric trigonal pyramid, which has an equilateral triangular base, see Fig. 19 (a). The scattering centres are randomly distributed but identically oriented along the axes of high symmetry x_0, y_0. In the absence of radiation, the anisotropically scattered carriers compensate each other and no current flows, see Fig. 19 (a).

This picture changes, if the system is driven out of equilibrium, e.g. if an alternating electric field acts upon the carriers. Application of linearly polarized THz radiation leads to an alignment of carrier momenta. Consequently, the total number of carriers moving back and forth along the electric field di-

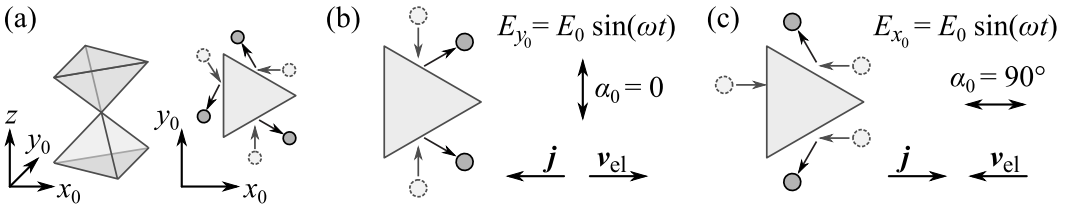

Figure 19: Model of photogalvanic effect for systems with trigonal symmetry, like Bi_2Te_3- and Sb_2Te_3-based topological insulators. (a) For C_{3v} point group symmetry the anisotropy of elastic scattering of carriers is the same as scattering by a double triangular pyramid, sketched in 3D and top view. Current formation due to asymmetrical elastic scattering of carriers for linear polarization along (b) y_0 direction ($\alpha_0 = 0$) and (c) x_0 direction ($\alpha_0 = 90°$). Adapted from Refs. [44, 47].

rection increases, leading to a stationary correction to the carrier distribution function, which scales quadratically in the electric field. The corrections to the distribution function is written as an expansion in electric field. The first order term $f^{(1)}(t) \propto \exp(-i\omega t)$ is oscillating in time whereas the second one $f^{(2)} \propto |\boldsymbol{E}|^2$ is static. The alignment of carrier momenta itself does not lead to a current, but due to asymmetric scattering on wedges the excess of carriers moving along the electric field violates the balance of carrier flow. The current formation due to asymmetric scattering is shown in Fig. 19 (b) and (c). For an alternating electric field oriented along the y_0 direction, i.e. $E_{y_0} = E_0 \sin(\omega t)$, corresponding to $\alpha_0 = 0$, the process is illustrated in Fig. 19 (b). Due to the second order static correction and the resulting increased carrier flux along the electric field vector, more carriers are scattered on the trigonal wedge in x_0 direction, and assuming electrons, an electric current flows in $-x_0$ direction. Rotation of the electric field vector by 90°, i.e. $E_{x_0} = E_0 \sin(\omega t)$, more carriers are scattered in $-x_0$ direction, and the net current flows in x_0 direction, see Fig. 19 (c). Note that for this model, backscattering is not taken into account, because it is forbidden in topological insulators. The model yields that the current along the x_0 axis follows a $\cos(2\alpha)$ dependence, which is in accordance with phenomenological theory and is observed in the experiments. Consequently, the model based on elastic asymmetric scattering describes well the current formation.

As the model reveals, the photocurrent direction is determined by the orientation of the crystallographic axes x_0 and y_0 with respect to the electric field vector. A rotation between the coordinated systems (x_0, y_0) and (x, y), in which the current is probed, is observed in experiments, see Fig. 18. For this Sb_2Te_3 sample a phase shift $\Phi = -4°$ in the XRD data, and $3\Phi = -12°$ in the

photocurrents is observed. The electric field vector rotation is denoted as α in the (x, y) system, while in the (x_0, y_0) frame it is shifted by Φ and denoted as $\alpha_0 = \alpha - \Phi$. Therefore, the photogalvanic current probed along the x_0 and the y_0 direction is then given by

$$\begin{aligned} j_{x_0} &\propto -\cos(2(\alpha - \Phi)), \\ j_{y_0} &\propto \sin(2(\alpha - \Phi)). \end{aligned} \tag{42}$$

The current components measured in experiments compose to $J_x = J_{x_0}\cos\Phi - J_{y_0}\sin\Phi$ and $J_y = J_{y_0}\cos\Phi + J_{x_0}\sin\Phi$. Using trigonometry, one obtains the relation

$$\begin{aligned} J_x/I &\propto -\cos(2\alpha - 3\Phi), \\ J_y/I &\propto \sin(2\alpha - 3\Phi). \end{aligned} \tag{43}$$

This is in agreement with the experimental data.

Microscopic Theory of the Photogalvanic Effect Now the photogalvanic current is derived with a microscopic theory, which was developed in collaboration with Prof. Dr. Leonid E. Golub[4], for details see Refs. [44, 47].

The total current can be calculated after [61]

$$\boldsymbol{j} = e\sum_{\boldsymbol{p}} \boldsymbol{v}_{\boldsymbol{p}} \delta f_{\boldsymbol{p}}. \tag{44}$$

Here, $\boldsymbol{v}_{\boldsymbol{p}} = v_0\,\boldsymbol{p}/p$ is the velocity of carriers with momentum $\boldsymbol{p}$ and v_0 is the Dirac fermion velocity. $\delta f_{\boldsymbol{p}}$ is a correction to the distribution function, which is quadratic in $\boldsymbol{E}$.

To find $\delta f_{\boldsymbol{p}}$, first the carrier distribution function $f_{\boldsymbol{p}}(t)$ is derived from solving the kinetic Boltzmann equation

$$\frac{\partial f_{\boldsymbol{p}}}{\partial t} + e\boldsymbol{E}\cdot\frac{\partial f_{\boldsymbol{p}}}{\partial \boldsymbol{p}} = -\sum_{\boldsymbol{p}'}\left(W_{\boldsymbol{p}'\boldsymbol{p}} f_{\boldsymbol{p}} - W_{\boldsymbol{p}\boldsymbol{p}'} f_{\boldsymbol{p}'}\right), \tag{45}$$

in which $\boldsymbol{E}(t) = E_0\exp(-\mathrm{i}\omega t) + c.c.$ is the electric field, $\boldsymbol{p}$ and $\boldsymbol{p}'$ are the carrier momenta before and after a scattering event, and $W_{\boldsymbol{p}'\boldsymbol{p}}$ is a scattering

[4] Ioffe Institute, St. Petersburg, Russia

probability, which can be written as

$$W_{\boldsymbol{p}'\boldsymbol{p}} = W^{(s)}_{\boldsymbol{p}'\boldsymbol{p}} + W^{(a)}_{\boldsymbol{p}'\boldsymbol{p}} \tag{46}$$

divided into a symmetric part $W^{(s)}_{\boldsymbol{p}'\boldsymbol{p}} = W^{(s)}_{-\boldsymbol{p}'-\boldsymbol{p}}$ and an asymmetric one $W^{(a)}_{\boldsymbol{p}'\boldsymbol{p}} = -W^{(a)}_{-\boldsymbol{p}'-\boldsymbol{p}}$. For the non-centrosymmetric surface the scattering probability is non-zero and asymmetric, even for isotropic scatterers like phonons or impurities. For topological insulators, backscattering is unlikely, which is taken into account in the symmetrical probability as $W^{(s)}_{\boldsymbol{p}'\boldsymbol{p}} \propto \cos^2[(\phi_{\boldsymbol{p}'} - \phi_{\boldsymbol{p}})/2]$, where $\phi_{\boldsymbol{p}}$ and $\phi_{\boldsymbol{p}'}$ are the polar angles of vectors $\boldsymbol{p}$ and $\boldsymbol{p}'$. The distribution function

$$f_{\boldsymbol{p}}(t) = f_0(\varepsilon_{\boldsymbol{p}}) + f^{(1)}_{\boldsymbol{p}}(t) + f^{(2)}_{\boldsymbol{p}}, \tag{47}$$

contains the carrier distribution in equilibrium $f_0(\varepsilon_{\boldsymbol{p}})$, a time dependent oscillating term $f^{(1)}_{\boldsymbol{p}}(t)$, and $f^{(2)}_{\boldsymbol{p}}$, which is static and proportional to the squared electric field $|E|^2$. Considering $eE_0 v_0 \tau_{\rm tr}/\varepsilon_{\rm F} \ll 1$ for linear dispersion surface state and $\tau_{\rm tr}^{-1} = \sum_{\boldsymbol{p}'} W^{(s)}_{\boldsymbol{p}'\boldsymbol{p}}[1 - \cos(\phi_{\boldsymbol{p}'} - \phi_{\boldsymbol{p}})]$ for the transport scattering time $\tau_{\rm tr}$, the total current density is given by

$$j_{x_0,y_0} = \pm s_{1,2}|E_0|^2 e v_0 \sigma(\omega) \left[\frac{1}{\varepsilon_{\rm F}^2}\frac{d(\Xi\tau_2\varepsilon_{\rm F}^2)}{d\varepsilon_{\rm F}} + \frac{1-\omega^2\tau_{\rm tr}\tau_2}{1+(\omega\tau_2)^2}\frac{\Xi\tau_2\varepsilon_{\rm F}}{\tau_{\rm tr}}\frac{d(\tau_{\rm tr}/\varepsilon_{\rm F})}{d\varepsilon_{\rm F}}\right] \tag{48}$$

in which $s_1 = |E_{x_0}|^2 - |E_{y_0}|^2$ and $s_2 = E_{x_0}E^*_{y_0} + E_{y_0}E^*_{x_0}$ are the Stokes parameters for linearly polarized light, τ_2 is in the same order than the scattering time $\tau_{\rm tr}$ and is the time for the relaxation from carrier alignment given by $\tau_2^{-1} = \sum_{\boldsymbol{p}'} W^{(s)}_{\boldsymbol{p}'\boldsymbol{p}}[1 - \cos 2(\phi_{\boldsymbol{p}'} - \phi_{\boldsymbol{p}})]$. The asymmetry of the scattering probability is considered by the factor $\Xi \ll 1$

$$\Xi = \tau_{\rm tr} \sum_{\boldsymbol{p}'} \left\langle 2\cos\phi_{\boldsymbol{p}} \cos 2\phi_{\boldsymbol{p}'}\, W^{(a)}_{\boldsymbol{p}'\boldsymbol{p}} \right\rangle_{\phi_{\boldsymbol{p}}}, \tag{49}$$

where $\langle\rangle$ denotes averaging over all directions of $\boldsymbol{p}$ at the Fermi circle. Estimation of the scattering potential shows that for the considered Dirac fermions the current vanishes for short range scattering ($\Xi = 0$), see supplementary material of Ref. [44] for more details. Only for scattering by Coulomb impurities or phonons, Ξ is finite and a photogalvanic current can be generated. Last, Eq.(48) contains also the high frequency Drude conductivity

$$\sigma(\omega) = e^2\varepsilon_{\rm F}\tau_{\rm tr}/[4\pi\hbar^2(1+\omega^2\tau_{\rm tr}^2)]. \tag{50}$$

Equation (48) described well the experimental findings like the polarization and intensity dependencies via the Stokes parameters $s_{1,2}$ and $|E_0|^2$, respectively.

Microscopic Theory of the Photon Drag Effect The photon drag effect can have under some conditions small contributions to the photocurrent formation. Therefore, the microscopic theory for the photon drag current, caused by q_z-component of the photon wave vector, is also shortly discussed [47]. Treating the photon drag effect in a semi-classical approach, it is convenient to described it in terms of the radiation magnetic field $\boldsymbol{B}$ rather than by the transfer of q_z to free carriers. Using $\boldsymbol{B} = (c/\omega)\boldsymbol{q} \times \boldsymbol{E}$, one can rewrite Eq.(39) for the photon drag effect as

$$\begin{aligned} j_x = &\ Tq_z(|E_x|^2 - |E_y|^2) \propto E_x B_y^* + E_y B_x^* + c.c., \\ j_y = &\ -Tq_z(E_x E_y^* + E_y E_x^*) \propto E_x B_x^* - E_y B_y^* + c.c.. \end{aligned} \tag{51}$$

The microscopic theory then considers the Lorentz force of the radiation magnetic field, acting on the 2D carriers. The kinetic Boltzmann

$$\sum_{\boldsymbol{p}'} \delta W_{\boldsymbol{p}'\boldsymbol{p}}^{(\boldsymbol{B})} \left(f_{\boldsymbol{p}}^{(E)} - f_{\boldsymbol{p}'}^{(E)} \right) = -\tau_{\mathrm{tr}}^{-1}\, \delta f_{\boldsymbol{p}}^{(\boldsymbol{B})}, \tag{52}$$

can be solved with linear in $\boldsymbol{B}$ corrections to the elastic scattering probability $\delta W_{\boldsymbol{p}'\boldsymbol{p}}^{(\boldsymbol{B})}$ and distribution function $\delta f_{\boldsymbol{p}}^{(\boldsymbol{B})}$, and the linear in $E_\parallel$ distribution function $f_{\boldsymbol{p}}^{(E)}(\boldsymbol{r})$. The current density, linear in $E_\parallel$ and $B_\parallel$, is calculated with $\boldsymbol{j} = e\sum_{\boldsymbol{p}} \boldsymbol{v}_{\boldsymbol{p}} \delta f_{\boldsymbol{p}}$ [61]. Finally, the current density has the form

$$j_{x_0,y_0} = \pm s_{1,2} |E_0|^2 \sigma(\omega) q_z \frac{e\beta p_{\mathrm{F}}^2 \varepsilon_{\mathrm{F}}}{4\omega m v_0^2}, \tag{53}$$

in which m is the mass and β is a constant for the anisotropic scattering. The derived photon drag current is in agreement with the phenomenological theory and the experimental findings. It scales linear in intensity, $|E_0|^2$, and it is characterized by the Stokes parameters, $\pm s_{1,2}$.

4.1.3 Method for Characterization

In the following it is shown, that the photogalvanic effect can be used in centrosymmetric Bi_2Te_3- and Sb_2Te_3-based three dimensional topological insulators, as a method for the characterization of the surface states. This section shows that the room temperature scattering times and mobilities can be

estimated from the frequency dependence. Additional, the high frequencies electronic properties and the local domain orientation is probed spatially by scanning the laser spot across the sample.

Estimation of High Frequency Transport Properties The observed dependence of the photocurrent on the excitation frequency, see Eq.(41), shows a similar dependence as the Drude conductivity, see Eq.(50). For elastic scattering by Coulomb impurities, this dependence is also obtained from Eq.(48). For scattering by Coulomb impurities the alignment relaxation time is given by $\tau_2 = \tau_{\rm tr}/3$ and the photogalvanic coefficient in $j_{x_0,y_0} = \pm\chi E_0^2 s_{1,2}$, see Eqs.(39) and (48), scales as

$$\chi = \frac{2e^3 v_0 \Xi \, \tau_{\rm tr}^2}{4\pi\hbar^2(1+(2\pi f\tau_{\rm tr})^2)}. \tag{54}$$

Therefore, the room temperature scattering time $\tau_{\rm tr}$ can be estimated from the fit parameter $t_{\rm exp}$ in Eq.(41). Values can be estimated for samples, when the condition $\omega\tau_{\rm tr} \approx 1$ is fulfilled in the studied frequency range, see for example Fig. 16 (c) and (d). Typical values of the scattering time are in the picosecond range and are given in Tab. 3. In other samples, where the photocurrent scales after $1/f^2$ only a lower limit of the scattering time can be stated.

From the experimental values of the room temperature scattering times the corresponding high frequency mobilities can be calculated after

$$\mu^{\rm HF} = e v_{\rm F}^2 \tau_{\rm tr}/\varepsilon_{\rm F} \tag{55}$$

with Fermi velocity $v_{\rm F}$ and energy $\varepsilon_{\rm F}$. Both values are obtained from *in-situ* ARPES measurements, see Fig. 7 and Tab. 1 in Sec. 3.1.1. Typical values of the room temperature mobilities $\mu^{\rm HF}$ vary from 1000 up to several thou-

Sample	Bi_2Te_3	Bi_2Te_3/Sb_2Te_3			$(Bi_{1-x}Sb_x)_2Te_3$	
		7.5 nm	15 nm	25 nm	x = 0.43	x = 0.94
$\tau_{\rm tr}$ (ps)	> 0.25	0.06	0.06	0.08	> 0.25	0.04
$\mu^{\rm HF}$ (cm^2/Vs)	> 940	1230	1030	1420	> 1330	8210

Table 3: Room temperature scattering times $\tau_{\rm tr}$ and mobilities $\mu^{\rm HF}$ obtained from spectral dependence of photogalvanic effect in different samples. Thicknesses refer to Sb_2Te_3 layer. Adapted from Ref. [45].

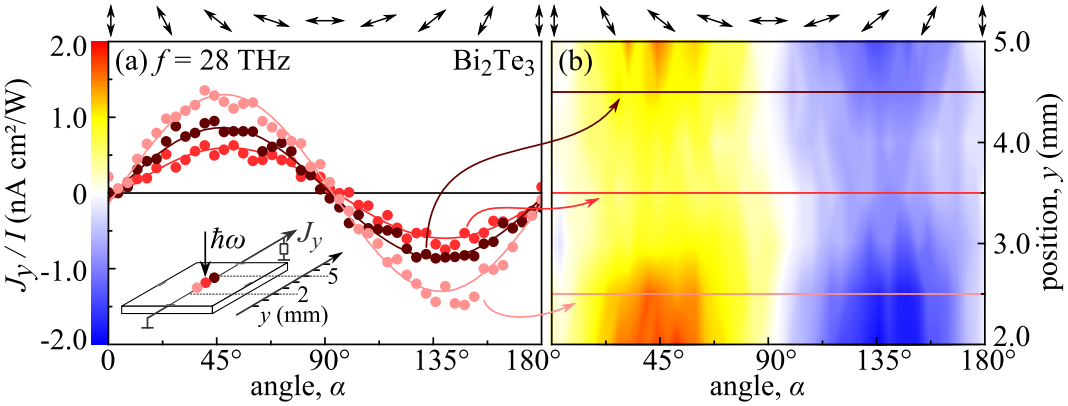

Figure 20: (a) Dependence of photocurrent normalized on radiation intensity J_y/I on α measured in Bi_2Te_3 for three different laser spot positions, see inset, at a radiation frequency of $f = 28$ THz. Solid lines show fit after Eq.(40). (b) Colour-coded normalized photocurrent as a function of α obtained by scanning across sample parallel to y axis with steps of 500 μm. Adapted from Ref. [46].

sand cm^2/Vs and are summarized in Tab. 3. The values are in the same order of magnitude as the ones measured with magneto-transport for low temperature (2-77 K) [25, 78]. Note that the highest mobility is calculated for a $(Bi_{0.06}Te_{0.94})_2Te_3$ sample, where the Fermi energy is close to the Dirac point. The estimation of the v_F and ε_F is in this sample difficult, and can easily lead to an overestimation of μ^{HF}.

Mapping of the Photocurrent As discussed in the model, the photocurrent direction is given by the orientation of the electric field vector with respect to the crystallographic axes x_0 and y_0. This correlation is shown in Fig. 17 and Fig. 18, in which XRD and photocurrent measurements allow to determine the rotation between (x_0, y_0) and (x, y), denoted as Φ. While XRD measurement probe only the global domain orientation, photocurrents probe additional the high frequency transport. Information on the local domain orientation, the presence of twisted domains in certain areas and the homogeneity of the transport properties, can be provided by decreasing the laser spot size from mm to μm and by probing the photocurrent at different positions on the sample by scanning the laser spot. For this purpose, a pulsed CO_2 laser is used, operating at a frequency of 28 THz. The laser radiation is focused down to several tens of μm. Note that the frequency used is in the range where Drude-like free carrier absorption dominates and that in the low terahertz frequency range the laser spot size can be up to 3 mm.

With such small laser spots, the photocurrent is then probed at different

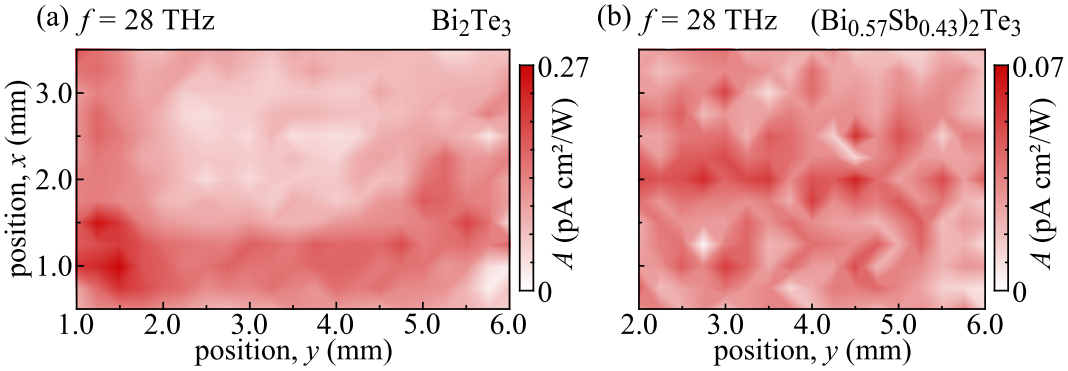

Figure 21: Colour-coded amplitude A as a function of coordinate, obtained for $f = 28$ THz and beam spot of about 30 μm by a two-dimensional scan in (a) Bi_2Te_3 and (b) $(Bi_{0.57}Sb_{0.43})_2Te_3$. The scans are obtained with steps of 250 μm. Adapted from Ref. [46].

positions on the sample, whereby neither contacts nor edges are illuminated. Additional measurements show that illumination of edges does not modify the results. Illumination of contacts, however, produces huge but polarization independent signals, which could be caused by thermal effects.

Figure 20 (a) shows the polarization dependence of the normalized photocurrent J_y/I in Bi_2Te_3, measured at three different positions along the y direction. The data reveal that they are well fitted by Eq.(40). For all three position the amplitude A is positive and no phase shift is observed demonstrating that the current is probed along $x_0||x$ direction. Note that in this figure, the polarization independent offset is subtracted, as it is becoming substantial for laser spot positions close to the contacts. A scan along the y direction is shown in Fig. 20 (b) for the same Bi_2Te_3 sample. The normalized photocurrent J_y/I is colour-coded ranging from -2 nAcm^2/W in blue to 2 nAcm^2/W in red, indicated on the left side of panel (a). The photocurrent has for a fixed angle α always the same sign.

To obtain 2D scans, the laser spot position is additionally moved in x direction. For the 2D scan the polarization dependent amplitude A is extracted and plotted against the laser spot position. Figure 21 presents this for Bi_2Te_3 and $(Bi_{0.57}Sb_{0.43})_2Te_3$ on a large area of 5×3 mm^2 and 4×3 mm^2, respectively. For these measurements a spot size of 30 μm is used with steps of 250 μm. The colour-coded amplitude is positive in the whole area and the phase shift is always zero ($\Phi = 0$). One can conclude, that the crystallographic axes are not tilted and that one domain outnumbers the second one. However, in both samples regions exist with vanishing current (white regions), which

implies the presences of twisted domains within the laser spot. For twisted domains the currents generated in both of them, chancel each other out, $j(\Phi = 0) = -j(\Phi = 180°)$. The photocurrent maps reveal, that $(Bi_{0.57}Sb_{0.43})_2Te_3$ is less homogeneous than Bi_2Te_3. This agrees with STM measurements and the information that Bi_2Te_3 growths smoothest, see Sec. 3.1.1.

To conclude, photogalvanic currents provide information on the average and local domain orientation and spatially resolved measurements allow mapping the photocurrent response. This provides information on the presence of twisted domains and give a topographical idea of the homogeneity of transport properties.

4.2 Photocurrents Excited at Oblique Incidence

All results discussed so far are obtained at normal incident radiation using front and back illumination. For this configuration only the in-plane electric fields $E_{x,y}$ and the out-of plane z component of the photon momentum are present. The following section deals with photocurrents excited at oblique incidence, where additional the out-of plane component of the electric field E_z and the in-plane photon momentum $q_{||}$ is present. It is shown, that these components can change the photocurrent formation.

4.2.1 Experimental Results

Applying linearly polarized radiation at oblique incidence, photocurrents are observed in Bi_2Te_3- and Sb_2Te_3-based thin films. Their main characteristics, like the dependence on the angle α and the linear dependence on the radiation intensity I remain unchanged as compared to the results at normal incidence. However, the polarization dependent amplitude depends now additionally on the angle of incidence θ, as well as on the direction in which the current is examined. Therefore, the fit parameters are denoted in the following as A_x and A_y.

For some excitation frequencies, a photocurrent decreases with increasing θ is observed. This is shown in Fig. 22 (a) for the normalized current J_y/I in $(Bi_{0.57}Sb_{0.43})_2Te_3$ for the (yz) plane of incidence at $\theta = 0$ and $\pm 30°$. The polarization independent offset is subtracted to better visualise the change in amplitude. The data reveal, that Φ does not change and that the signals decrease for negative and positive angles of incidence. The corresponding amplitudes A_x and A_y are shown in Fig. 22 (b) for several angle θ. This even in θ decrease is observed in many samples. Further examples are shown in Fig. 22 (c) and (d) for Bi_2Te_3 and Sb_2Te_3, both excited at $f = 1.1$ THz.

For other excitation frequencies and samples, a strong increase of the photocurrent is observed. This is shown in Fig. 23 (a) for Bi_2Te_3 for $\theta = 0$, 10° and 20°. As for the even decrease, the dependence on α remains unchanged, no phase shift is observed, and the data are fitted well with Eq.(40). The increase in θ happens at positive and negative angles, and the amplitudes A_y and A_x both increase, as it is shown for several angles θ in Fig. 23 (c). Further examples for the even in θ increase are shown in Fig. 23 (b) and (d) for $(Bi_{0.57}Sb_{0.43})_2Te_3$ and Sb_2Te_3 excited at 3.3 and 2.0 THz, respectively.

This even increase of the photocurrent amplitude is observed normal and

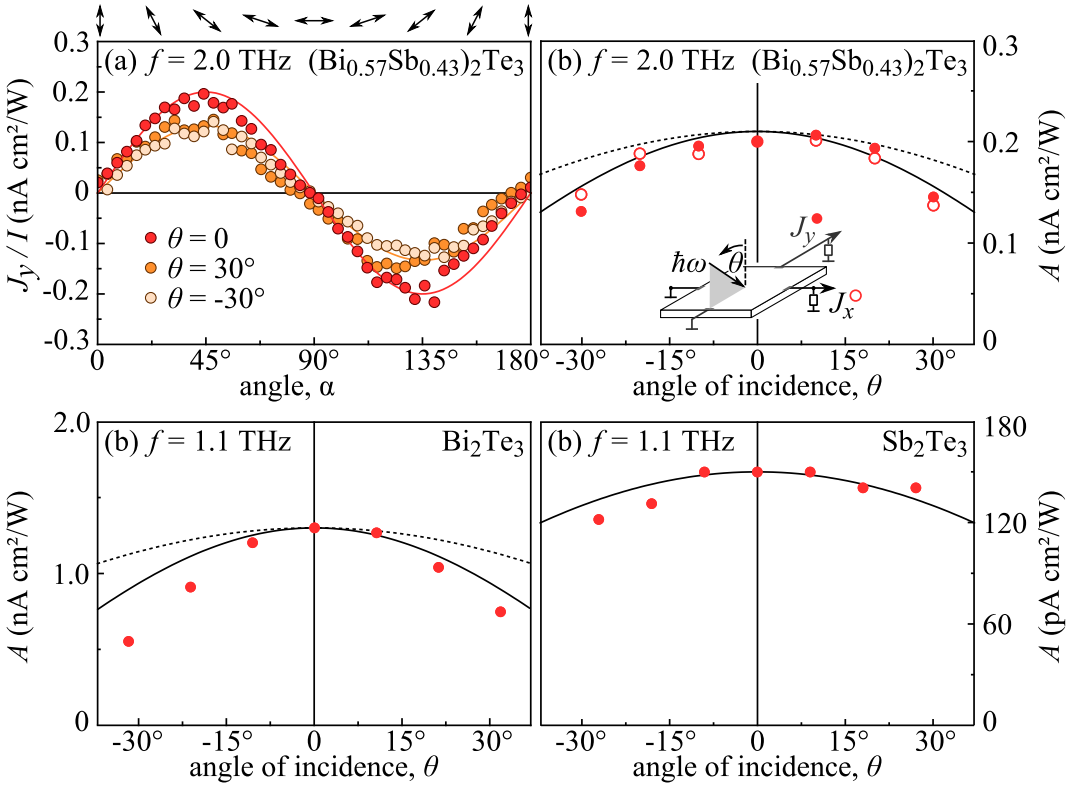

Figure 22: (a) Dependence of photocurrent J_y/I excited at $f = 2.0$ THz in $(Bi_{0.57}Sb_{0.43})_2Te_3$ on α for $\theta = 0$ and $\pm 30°$. Solid lines show fits after Eq.(40). Panel (b) - (d) show A as a function of angle of incidence for (a) $(Bi_{0.57}Te_{0.43})_2Te_3$ excited with radiation frequency $f = 2.0$ THz, (b) Bi_2Te_3 and (c) Sb_2Te_3 both excited with radiation frequency $f = 1.1$ THz. Solid lines are fits after Eq.(57). Inset in panel (b) shows experimental setup for (yz) plane of incidence. Adapted from Ref. [47].

parallel to the plane of incidence. It is also observed for any orientation of the plane of incidence. The rotation of the plane of incidence is denoted by Ψ, and its definition is shown in the inset in Fig. 24 (b). Figure 24 (a) show polarization dependencies of the normalized photocurrent J_y/I for different angles Ψ for Bi_2Te_3 excited at 2.0 THz and $\theta = 20°$. Considering that in this sample $x_0||x$ and hence $\Phi = 0$, the data are well fitted by

$$\begin{aligned} J_x/I &= -A_x \cos(2\alpha - \phi) + C_x, \\ J_y/I &= A_y \sin(2\alpha - \phi) + C_y, \end{aligned} \tag{56}$$

where ϕ is the observed phase shift. The normalized photocurrent depends now on the current direction, the frequency, the angle of incidence θ, but also on Ψ. The observed changes of the amlitude A on Ψ are, however, quite small and cannot be discussed unambiguously, since precise adjustment is difficult

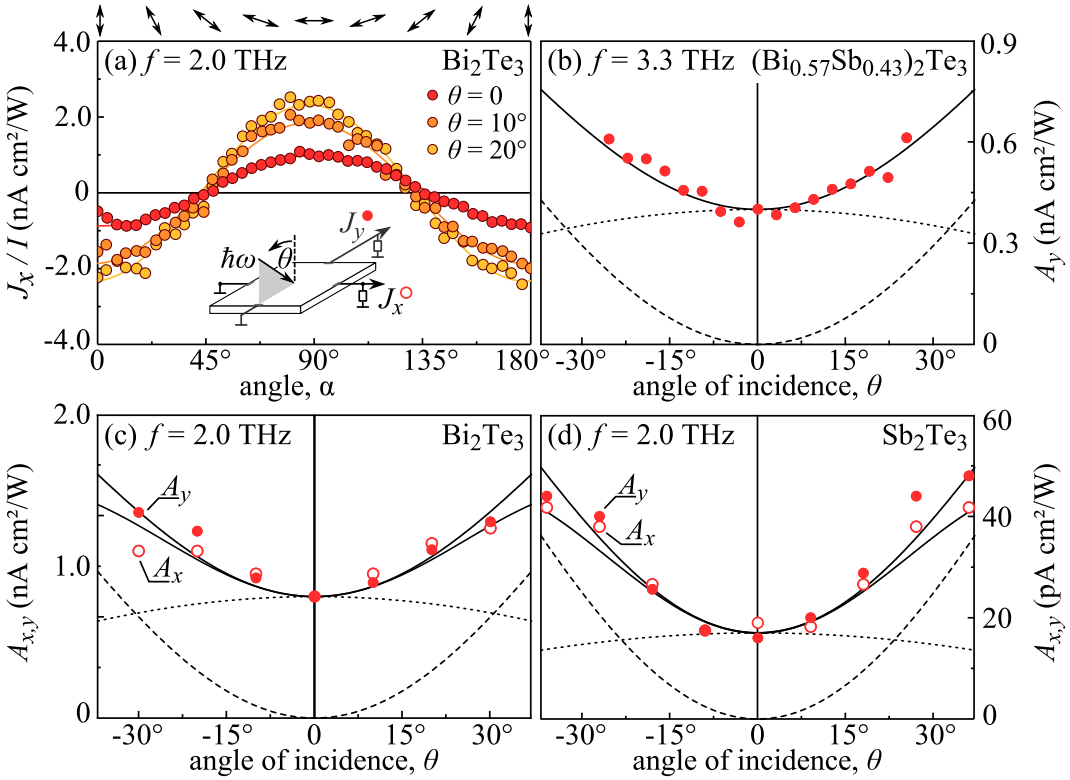

Figure 23: (a) Dependence of photocurrent J_x/I excited at $f = 2.0$ THz in Bi_2Te_3 on α for $\theta = 0$, 10°, and 20°. Solid lines show fits after Eq.(40). Panel (b)-(d) show photocurrent amplitudes A_x and A_y as a function of angle of incidence for (b) $(Bi_{0.57}Sb_{0.43})_2Te_3$ excited with radiation frequency $f = 3.3$ THz, (c) Bi_2Te_3 and (d) Sb_2Te_3 both excited with radiation frequency $f = 2.0$ THz. Solid lines are fits after Eq.(58). Inset in panel (a) shows experimental setup for (yz) plane of incidence. Adapted from Ref. [47].

in this experimental geometry and a movement of the sample spot cannot be excluded. The correlation between the observed phase shift ϕ and Ψ is plotted for both current directions in Fig. 24 (b). The observed phase shift follows $\phi = 2\Psi$.

4.2.2 Discussion

So far, the discussion of possible contributions to the photocurrent is limited to electric field and photon momentum components, which are present at normal incidence and, as it is shown in Sec. 2.2, the photogalvanic and the photon drag effect then are caused by in-plane electric field components $E_{x,y}$ and the out-of-plane z component of the photon momentum. Consequently, both effects decrease at oblique incidence. Considering the (yz) plane of incidence used in most of the experiments, the E_y and the q_z components diminish

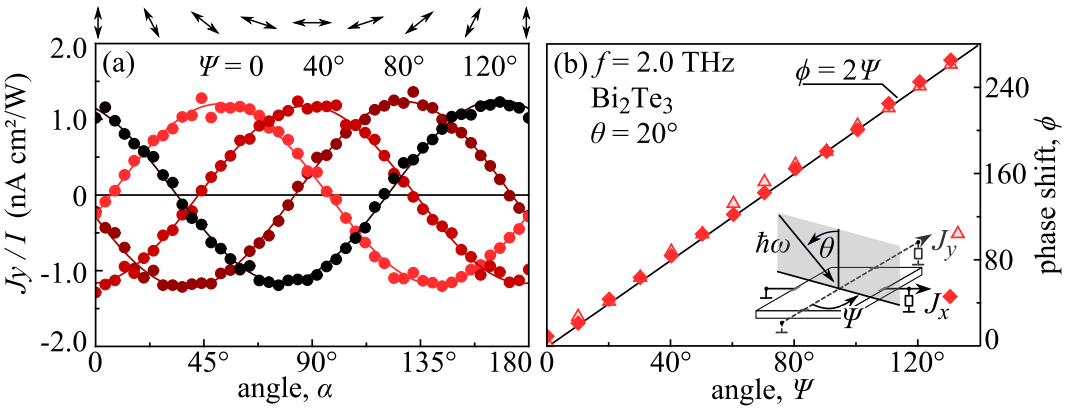

Figure 24: (a) Dependence of normalized photocurrent J_y/I excited at 2.0 THz in Bi_2Te_3 on rotation of linear polarization, obtained at oblique incidence ($\theta = 20°$) and $\Psi = 0$, 40°, 80°, and 120°. Solid lines are fits after Eq.(56). (b) Measured phase shift ϕ as a function of Ψ for J_x/I and J_y/I in Bi_2Te_3. Data are fitted with $\phi = 2\Psi$. Adapted from Ref. [47].

by a factor $\cos\theta$, while E_x remains constant. For oblique incidence, their phenomenological equation, see Eq.(39), can be rewritten to

$$\begin{aligned} j_x = & \; -(\chi - T_z\, q \cos\theta) E_0^2 \, \cos(2\alpha)(t_s^2 + t_p^2 \cos^2\theta), \\ j_y = & \; (\chi - T_z\, q \cos\theta) E_0^2 \, \sin(2\alpha) \cos\theta. \end{aligned} \tag{57}$$

t_s and t_p are the Fresnel transmission coefficients for s and p polarized light. Note that the photon drag effect decrease as $\cos^2\theta$ and consequently faster than the photogalvanic effect and the data in Fig. 22 can be fitted with Eq.(57). In Fig. 22 (b)-(d), the dashed line represents a fit for the photogalvanic effect only, while the solid line is the fit using both contributions. This indicates that, as discussed before, the photon drag effect is for some excitation frequencies or samples not negligible.

Clearly, Eq.(57) does not describe the observed increase, see Fig. 23. Therefore it is necessary to consider other contributions to the photocurrent formation. Several types of photogalvanic and photon drag effects can give rise to currents being odd or even in the angle θ and new roots emerge from the normal to the surface component of the radiation electric field E_z and the in-plane component of the photon momentum $q_\parallel$. One of them, the trigonal photon drag effect, is caused by all of them, in- and out-of plane electric field components and additionally, by the transfer of the in-plane photon momentum. At normal incidence it is not present. At oblique incidence it increases, due to the simultaneous action of all three components, for negative and positive angles

of incidence. While the in-plane components decrease as $\cos\theta$ or remain the same, see discussion above, the out-of-plane electric field component E_z and the in-plane photon momentum $q_\parallel$ increase as $\sin\theta$. The product of the latter components $\sin^2\theta$ makes an even in the angle of incidence increase possible. For the (yz) plane of incidence the trigonal photon drag effect is given by

$$\begin{aligned} j_x = & -T_\parallel q_y E_y E_z = -T_\parallel/2\, E_0^2\, \cos(2\alpha)\, t_p^2\, q \sin^2\theta \cos\theta + j_{\rm off}, \\ j_y = & -T_\parallel q_y E_x E_z = T_\parallel/2\, E_0^2\, \sin(2\alpha)\, t_s t_p\, q \sin^2\theta. \end{aligned} \tag{58}$$

Note that $j_{\rm off}$ is a polarization independent current, which is zero at $\theta = 0$. Equation (58) described well the dependencies of the photocurrent on α observed in experiments, see Fig. 23 (a). The trigonal photon drag effect has the same sign for negative and positive angles of incidence and vanishes at normal incident radiation ($E_z = 0$, $q_\parallel = 0$).

The observed photocurrent increase at oblique incidence has to be treated always as a combination of both, the photogalvanic effect and the trigonal photon drag effect. Figure 23 (b)-(d) shows the contributions of the decreasing photogalvanic effect ($\cos\theta$, dotted line) and of the trigonal photon drag effect ($\sin^2\theta$, dashed line). The solid lines show the sum of both contributions. Also, the different dependencies on θ for x and y direction is described well since the trigonal photon drag current increases faster in y than in x direction, see Fig. 23 (c) and (d). This difference is caused by the different combinations of q_y and $E_{x,y,z}$. For the (yz) plane of incidence, q_y and E_z increase as $\sin\theta$, E_x is constant and E_y decreases as $\cos\theta$. Consequently, it scales in x direction as $\sin^2\theta\cos\theta$ and in y direction as $\sin^2\theta$.

Strikingly, the trigonal photon drag current is observed in the direction parallel, but also normal to the plane of incidence. This is a noticeable result, since it is caused by the photon momentum $q_\parallel$ along the plane of incidence. The influence of the photon momentum $q_\parallel$ in respect to the crystallographic axes is probed by the rotation of the plane of incidence by Ψ changes also the relative orientation of the electric field and the crystallographic axes. Taking into account that for the experiments described above the trigonal photon drag effect is dominating the current formation, $T_\parallel q_y \gg (\chi + T_z q_z)$, and using small angles of incidence only $t = t_s = t_p$, the current density, see Eqs.(57) and (58),

is given by

$$\begin{aligned} j_x &\approx -\cos(2\alpha - 2\psi)\,(\chi - T_z q + T_\parallel\, q\,\theta^2/2)\, t^2 E_0^2, \\ j_y &\approx \sin(2\alpha - 2\psi)\,(\chi - T_z q + T_\parallel\, q\,\theta^2/2)\, t^2 E_0^2. \end{aligned} \tag{59}$$

Note that here the offset is neglected. Equation (59) describes well the phase shift observed in the polarization dependencies of the photocurrent, see Fig. 24 (a). The in the experiments observed phase shift $\phi = 2\Psi$ is also in agreement with theory, see Fig. 24 (b). Equation (59) is obtained for the C_{3v} point group symmetry of the non-centrosymmetric surface states. The same behaviour of the photon drag current on the variation of radiation polarization and rotation of plane of incidence, can be found for the D_{3d} point group symmetry for centrosymmetric bulk. An attribution to the surface state is therefore not possible and the current can be generated by bulk states, too.

Microscopic Model of the Trigonal Photon Drag Effect The trigonal photon drag effect is studied in the frequency range where Drude-like free carrier absorption dominates and the photon energies used are much smaller than the Fermi energy. Therefore, the model and the theory are developed on a semi-classical basis.

The model for the trigonal photon drag effect is based on asymmetric scattering. In contrast to the one for the photogalvanic effect, caused by a stationary correction in the distribution function, here the *dynamical* alignment of carrier momenta is additionally considered. A net current is generated due to the different scattering probabilities for different half time periods of the radiation. The process is illustrated for a current generated parallel to the (xz) plane of incidence in Fig. 25 (a).

Similar to the photogalvanic model, the scattering centres are sketched as pyramids (wedges in top view), which are randomly distributed but identically oriented along the axes of high symmetry, see Fig. 25 (b). The double pyramid reflects the symmetry of a quintuple layer and in the absence of radiation, the thermal flow of scattered carriers compensates each other. This changes, if the system is driven out of equilibrium, e.g. if oblique incident THz radiation is applied. The in-plane electric field E_x acts upon the carriers with the electric force $e\boldsymbol{E}_\parallel e^{iq\boldsymbol{r}-i\omega t} = e\,iq_\parallel \boldsymbol{r}\boldsymbol{E}_\parallel e^{-i\omega t}$. This force depends for the (xz) plane of incidence on the coordinate x and accelerates the carriers along the positive or negative x direction. As a result, the carrier flow increases by $\delta i_x^\pm$. Due

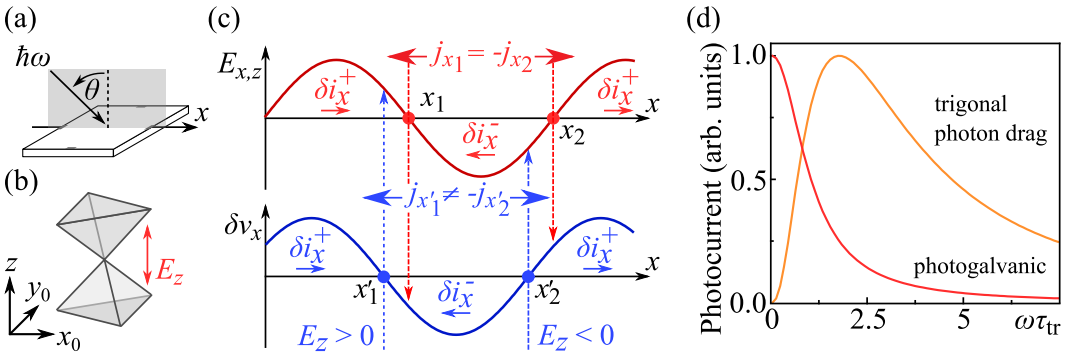

Figure 25: (a) Excitation of carriers at oblique radiation with (xz) plane of incidence. (b) For C_{3v} point group symmetry the anisotropy of elastic scattering of carriers is the same as for scattering by a double triangular pyramid. (c) Model of trigonal photon drag effect caused by *in-plane* photon momentum $q_\parallel$. Current formation due to the action of in- and out-of plane electric field components $E_{x,z}$ and retardation between the electric field and the instant velocity of charge carrier. (d) Dependence of photogalvanic and trigonal photon drag current on $\omega\tau_{\rm tr}$. Data are normalized to maximum value. Trigonal photon drag current is maximal at $\omega\tau_{\rm tr} \approx 2$. The photogalvanic current decreases after ω^{-2}. Adapted from Ref. [47].

to this *dynamical* alignment, the balance of carriers scattered locally changes and causes counter propagating currents $j_{x_{1,2}}$, see Fig. 25 (c). These local currents compensate each other and the net current remains zero. Only due to the additional action of the out-of plane electric field component E_z and retardation between the electric field and the instant velocity of the carrier, a direct current flows. Then scattering is different for different half time periods as the carriers are pushed along the z direction to the top and bottom part of the double pyramids. This asymmetry along z direction is present in the non-centrosymmetric C_{3v} group of the surface states. The retardation is shown in Fig. 25 (c) with shifted nodes from positions $x_{1,2}$ to $x'_{1,2}$, where the carriers are sensitive to the non-zero out-of plane electric fields $E_z(x'_{1,2})$. As pointed out above, the positive or negative fields $E_z(x'_{1,2})$ push the carrier up or downwards along the z direction, where they are scattered on pyramids. The resulting disbalance by different scattering probabilities leads to a current.

Microscopic Theory of the Trigonal Photon Drag Effect A corresponding theory was developed in collaboration with Prof. Dr. Leonid E. Golub[5], see Ref. [47]. The photocurrent origin is discussed with a semi-classical approach, as the photon energy is small in the frequency range (0.6 to 3.9 THz) and indirect intraband transitions appear, see Fig. 7 in Sec. 3.1.1.

[5] Ioffe Institute, St. Petersburg, Russia

For $\hbar\omega \ll \varepsilon_{\mathrm{F}}$ the photocurrent can be derived with Eq.(44) with the correction to the distribution function $\delta f_{\boldsymbol{p}}$ [61]. The latter is derived by solving the kinetic Boltzmann equation

$$\boldsymbol{v}_{\boldsymbol{p}} \cdot \frac{\partial f_{\boldsymbol{p}}(\boldsymbol{r})}{\partial \boldsymbol{r}} + \frac{\partial f_{\boldsymbol{p}}(\boldsymbol{r})}{\partial t} + e\boldsymbol{E}(\boldsymbol{r},t) \cdot \frac{\partial f_{\boldsymbol{p}}(\boldsymbol{r})}{\partial \boldsymbol{p}} = -\sum_{\boldsymbol{p}'} \left(W_{\boldsymbol{p}'\boldsymbol{p}} f_{\boldsymbol{p}} - W_{\boldsymbol{p}\boldsymbol{p}'} f_{\boldsymbol{p}'} \right), \quad (60)$$

for the coordinate dependent carrier distribution function $f_{\boldsymbol{p}}(\boldsymbol{r})$ and $W_{\boldsymbol{p}'\boldsymbol{p}} = W^{(0)}_{\boldsymbol{p}'\boldsymbol{p}} + \delta W_{\boldsymbol{p}'\boldsymbol{p}}$, where $W^{(0)}_{\boldsymbol{p}'\boldsymbol{p}}$ is the independent part and $\delta W_{\boldsymbol{p}'\boldsymbol{p}}$ the linear in E_z correction. For the asymmetric scattering probability $W^{(a)}_{\boldsymbol{p}'\boldsymbol{p}}$, linear dispersion surface states and their hexagonal warping, see Fig. 7 for ARPES measurements and Ref. [83], are taken into account. Furthermore, $\boldsymbol{v}_{\boldsymbol{p}} = v_0 \boldsymbol{p}/p$ is the velocity of surface charge carriers with a momentum $\boldsymbol{p}$ and v_0 is the Dirac fermion velocity. Additionally the changes of the wave function along the z direction due to the perturbation by the THz electric field E_z, is included. For details see Ref. [47]. The photocurrent can then be calculated with Eq.(44) for the (xz) plane of incidence as

$$\begin{aligned} j_x &= T_{\parallel} q_x E_x E_z = \frac{e\beta\lambda^w p_{\mathrm{F}}^2\, \omega\tau_2(\tau_{\mathrm{tr}} + \tau_2)}{4(1+\omega^2\tau_2^2)} \sigma(\omega) q_x E_x E_z, \\ j_y &= -T_{\parallel} q_x E_y E_z, \end{aligned} \quad (61)$$

in which λ^w is a constant for hexagonal warping of the Fermi surface, τ_{tr} is the transport scattering time given by $\tau_{\mathrm{tr}}^{-1} = \sum_{\boldsymbol{p}'} W^{(0)}_{\boldsymbol{p}'\boldsymbol{p}} [1 - \cos(\phi_{\boldsymbol{p}'} - \phi_{\boldsymbol{p}})]$, and τ_2 being in the same order is the time for the alignment relaxation given by $\tau_2^{-1} = \sum_{\boldsymbol{p}'} W^{(0)}_{\boldsymbol{p}'\boldsymbol{p}} [1 - \cos 2(\phi_{\boldsymbol{p}'} - \phi_{\boldsymbol{p}})]$. The anisotropic scattering constant, which is non-zero in the C_{3v} symmetry group, is given by

$$\beta = \frac{\sum\limits_n \langle \mathrm{Im}\left(V_{sn} z_{ns} V^*_{ss}\right) \rangle / \varepsilon_n}{\langle |V(\boldsymbol{p}' - \boldsymbol{p})|^2 \sin^2(\phi_{\boldsymbol{p}'} - \phi_{\boldsymbol{p}}) \rangle}, \quad (62)$$

where $\langle\rangle$ means averaging over both scatterer positions and the scattering angle $(\phi_{\boldsymbol{p}'} - \phi_{\boldsymbol{p}})$. The index s labels bulk orbitals from which the surface states are formed and n enumerates other energy bands of the bulk crystal. V_{sn} and V_{ss} are the inter- and intra band matrix elements of the scattering potential in coordinate z. Equation (61) describes well the experimental findings like the dependence on the orientation of the electric field vector. It also describes the increase of the photocurrent for oblique incidence.

The frequency dependencies of the trigonal photon drag current is shown in

Fig. 25 (d), together with the one of the photogalvanic currents. The photogalvanic current drops monotonously with the frequency increase. The trigonal photon drag current has a maximum at $\omega\tau_{\rm tr} \approx 2$. At high frequencies, both trigonal photon drag and photogalvanic currents decrease as ω^{-2}. The difference between the dependencies can be the cause for the observed variation of the ratio between photon drag and photogalvanic currents. For elastic scattering by Coulomb impurities, the relaxation times are related as $\tau_2 = \tau_{\rm tr}/3$, and the trigonal photon drag to photogalvanic ration can be estimated as

$$\frac{T_\parallel q}{\chi} \sim \frac{\lambda^w\, p_{\rm F}^2}{v_0}\, \frac{\beta\, q\, \varepsilon_{\rm F}}{\Xi}. \tag{63}$$

The first factor is a dimensionless degree of warping. For the cases, where the trigonal photon drag current at oblique incidence is larger than the photogalvanic one, the interband scattering parameter β can be estimated for the studied samples $\beta > 10$ Å/eV.

The ratio between the in- and out-of-plane photon drag effect is given by

$$\frac{T_z}{T_\parallel} \sim \frac{1 + (\omega\tau_{\rm tr})^2}{(\omega\tau_{\rm tr})^2}\, \frac{\varepsilon_{\rm F}}{m\, v_0^2}, \tag{64}$$

Since $m v_0^2 \sim 10$ eV, the factor $\varepsilon_{\rm F}/m v_0^2$ is in the order of 10^{-1} to 10^{-2} for our samples. This estimation explains why in the experiments $T_\parallel \gg T_z$. A detection of the out-of-plane photon drag effect is possible only due to the vanishing in-plane photon momentum at normal incidence. The T_z constant has a different frequency dependence than $T_\parallel$ and the role of the out-of-plane photon drag current is enhanced at small frequencies $\omega\tau_{\rm tr} \ll 1$.

4.3 Photocurrents Excited at High Frequencies

In this last section the non-monotonic increase of the polarization dependent photocurrent, which is observed at high frequencies, is discussed. Besides these enhanced signals, obtained with linearly polarized radiation, helicity sensitive contributions to the photocurrent are observed at oblique incidence in the same range of frequencies.

4.3.1 Experimental Results

The dependencies of the photocurrent on the excitation frequency in Sec. 4.1 reveal that at high frequencies an increased photocurrent is observed. This photocurrents do not follow the frequency dependence, typical for Drude-like free carrier absorption. In the examples shown in Fig. 16 (b)-(d), the photocurrent amplitude can be orders of magnitudes larger than the one expected from the semi-classical approach. Figure 26 (a) shows another example, for a Bi_2Te_3/Sb_2Te_3 heterostructure with an antimony thickness of 7.5 nm. In the lower THz range, the data are fitted by Eq.(41) and are described by Drude-like free carrier absorption. At high excitation frequencies the polarization dependent part of the photocurrent has much higher values as excepted from the fit. The exact shape and photocurrent maximum is again not resolved accurately due to discrete frequencies available in the experiments. Although the photocurrent amplitude shows a different dependence on the excitation

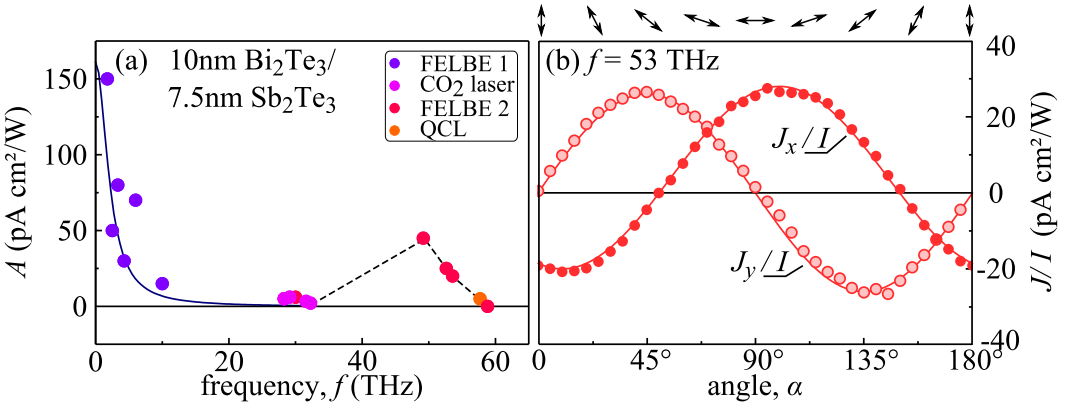

Figure 26: (a) Dependence of photogalvanic coefficient A on radiation frequency f for a 10 nm Bi_2Te_3/7.5 nm Sb_2Te_3 heterostructure. Solid line shows fit after Eq.(41), for theory see Eq.(54). Dots in different colour correspond to different laser sources. (b) Dependence of normalized photocurrent J_x/I and J_y/I on orientation of radiation electric field vector, in 10 nm Bi_2Te_3/7.5 nm Sb_2Te_3 heterostructure with radiation frequency $f = 53$ THz. Adapted from Ref. [45].

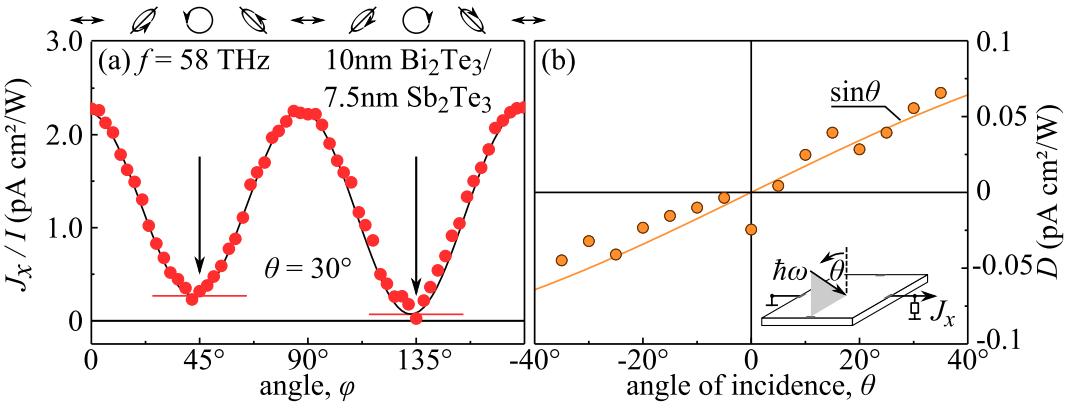

Figure 27: (a) Dependence of normalized photocurrent J_x/I on angle φ measured in a 10 nm Bi_2Te_3/7.5 nm Sb_2Te_3 heterostructure at $\theta = 30°$ and radiation frequency $f = 58$ THz. Solid line shows fit after Eq.(65), for theory see Eq.(66). Dashed horizontal lines and downwards pointing arrows indicate photocurrent for circularly polarized radiation. (b) Dependence of D on angle of incidence θ. Data are fitted by $\sin\theta$. Insets shows experimental setup. Adapted from Ref. [45].

frequency above 40 THz, its overall behaviour as compared to the ones excited at lower frequencies, remains unchanged. Figure 26 (b) shows the polarization dependence for the photocurrent measured along x and y direction in the Bi_2Te_3/Sb_2Te_3 heterostructure excited with a radiation frequency of $f = 53$ THz. The dependencies are well fitted by Eq.(40). Measurements using front and back illumination reveal that the photogalvanic effect dominates the current formation also in the high frequency range. Small contributions from the photon drag effect, however, are not excluded.

Besides linearly, also elliptically and circular polarized radiation is used to excite photocurrents. Illumination Bi_2Te_3- and Sb_2Te_3-based 3D TIs with elliptically polarization radiation modifies the photocurrent dependence, see Fig. 27 (a). The normalized photocurrent J_x/I is measured in the direction normal to the plane of incidence, $\theta = 30°$. The data are well fitted by

$$J_x/I = -A(1 + \cos(4\varphi))/2 + D\sin(2\varphi) + C_x, \tag{65}$$

where C_x and A are fit parameters for the polarization independent and dependent current caused by linearly polarized radiation, see Eq.(40). The Stokes parameter $s_1 = -(1 + \cos(4\varphi))/2$ describes the degree of linearly polarized radiation and corresponds to $\cos(2\alpha)$. Additional, the photocurrent is sensitive to the radiation helicity and shows a small, but clearly pronounced difference

at angles $\varphi = 45°$ and $\varphi = 135°$. This is described by the Stokes parameter $s_3 = \sin(2\varphi)$. This helicity sensitive contribution is fitted with the parameter D, which increases for increasing angles of incidence. This is shown in Fig. 27 (b) for different angle of incidence θ. The part of the photocurrent, which is caused by the radiation helicity, has opposite sign of negative and positive angles θ and varies as $\sin\theta$.

4.3.2 Discussion

The photocurrents observed in the high frequency range and excited at normal incidence with linearly polarized radiation, are described by Eq.(39). The analysis reveals that the photogalvanic effect, caused by the in-plane electric field components, dominates the current formation.

The helicity sensitive contribution to the photocurrent is, however, not describes by Eq.(39). For oblique incidence and the C_{3v} point group symmetry, the current density measured along the direction normal to the (yz) plane of incidence is given by

$$\begin{aligned} j_x^{circ} &= \gamma\, t_p t_s\, E_0^2\, n \sin\theta P_{circ}, \\ j_y^{circ} &= 0. \end{aligned} \tag{66}$$

γ is the circular photogalvanic coefficient, t_s and t_p are the Fresnel transmission coefficients for s and p polarized light, and n is the refraction index. Note that for the direction parallel to the plane of incidence, the circular photogalvanic current is not present. Equation (66) describes well the helicity sensitive contribution to the total photocurrent, which scales as $\sin\theta$ and is present only in the direction normal to the plane of incidence.

Microscopically, Drude-like free carrier absorption is very unlikely to be the origin for the photocurrent, as the deviation from the frequency dependence shows. As the photon energy and the Fermi energy are comparable in this high frequency range, direct optical transitions must also be considered. Such direct optical transitions can also give rise to photocurrents. They can be caused by the shift of electron wave packets in the real space (shift contribution) or due to asymmetric relaxation of the excited carriers [61].

Possible direct optical transitions can take place within the Dirac cone (*interband*) or from the Dirac cone to bulk states (*photoionization*). The first ones are unlikely as they have a constant probability, which is contradictory to the resonant like enhanced photocurrent signal observed in experiments, see

Fig. 16 and Fig. 26. Photoionization is more likely, since it is caused by the depopulation of the Dirac states, which takes place only in a certain range of photon energies. The photon energy must fit between the occupied states in the Dirac cone and the empty states in the bulk band ($\hbar\omega < \varepsilon_{\mathrm{CB}} - \varepsilon_{\mathrm{F}}$). Therefore, the related photocurrent must show a non-monotonic resonant-like frequency dependence, see Fig. 16 (b)-(d) and Fig. 26 (a). Note that such criteria are not as straight forward as shown here, since the band structure in real systems is complicated. Band structure calculations and ARPES measurements show that this condition is fulfilled in all Bi_2Te_3/Sb_2Te_3 heterostructures used and in $(Bi_{0.06}Sb_{0.94})_2Te_3$ and therefore relevant. In $(Bi_{0.57}Sb_{0.43})_2Te_3$ the Fermi level lies in the conduction band, which results in the hybridization of the surface states and exclude photoionization. The observed resonance in this sample could be attributed to surface photocurrents served by bulk carriers. This explains why in Bi_2Te_3 no deviation from the Drude-like behaviour is observed. In this samples the Fermi energies of 500 meV makes direct optical transitions unlikely in the whole range of photon energies.

The microscopic origin of the helicity sensitive contribution to the photocurrent can be attributed to photoionization, the excitation of spin polarized Dirac fermions into bulk states. In contrast to the ones discussed above, the selective excitation of spin branches by circularly polarized radiation, which follows from the selection rules, must be considered. Such processes have been previously considered for 3D TIs excited with near infrared radiation [41, 89–91] and for 2D TIs excitation of electrons from helical edge states to bulk conduction band states [92, 93]. For Bi_2Te_3- and Sb_2Te_3-based thin films Rashba-Dresselhaus spin split states can also contribute to the photogalvanic current.

5 Edge Photocurrents in Graphene in the Quantum Hall Regime

In this chapter edge photocurrents in high mobility graphene are presented. In the first section results in the semi-classical regime at zero magnetic field are discussed. The second section deals with edge current excited in the quantum Hall regime. After discussing the experimental results, the photocurrent origin is analysed based on a microscopic model and theory.

5.1 Edge Photocurrents at Zero Magnetic Field

5.1.1 Experimental Results

By irradiating high mobility graphene with normal incident radiation, a photocurrent is observed. The photocurrent is measured between contact pairs along the sample edge. Figure 28 (a) shows a typical dependence of the normalized photocurrent on the rotation of the electric field vector. The data are obtained in sample G30A at normal incident with an excitation frequency of $f = 3.3$ THz, the experimental geometry is shown in the inset in panel (b). Photocurrents measured at the left and right edge have consistently opposite direction and are well fitted by

$$J/I = A\sin(2\alpha + \Phi) + C, \tag{67}$$

where A and C are the fit parameters for the polarization dependent photocurrent amplitude and the polarization independent offset, respectively, and Φ is a phase shift. The Stokes parameter for linear polarized radiation is given by $s_2 = -\sin(2\alpha)$. Note that the offset is much smaller than the polarization dependent amplitude and the current direction is determined by α. Also, the phase shift is small for the samples studied. The overall behaviour is the same for all samples used and for different contact pairs along the edge.

Illumination the graphene sample with elliptically polarization radiation at the same experimental conditions, modifies the photocurrent dependence, see Fig. 28 (b). Nevertheless, the photocurrent has still opposite direction at the left and the right edge. It is fitted by

$$J/I = A\sin(4\varphi + \Phi)/2 + D\sin(2\varphi) + C. \tag{68}$$

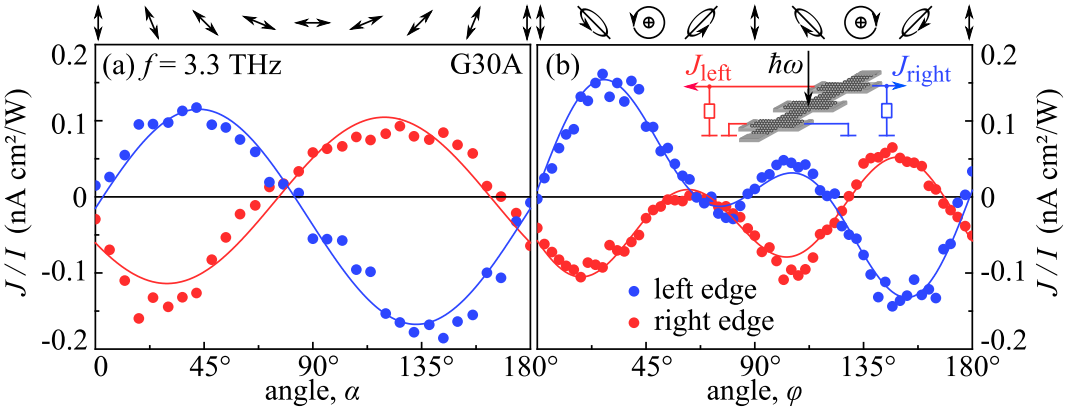

Figure 28: Normalized photocurrent J/I measured at opposite edges (right edge, contact pair 2-4, and left edge, contact pair 8-6) at zero magnetic field for (a) linearly and (b) elliptically polarized radiation. Solid lines show fits after Eq.(67), panel (a), and Eq.(68), panel (b). Inset shows experimental setup. Arrows and ellipses on top of both panels illustrates states of polarization for several angles α and φ.

A the fit parameter for the part depending on the linear polarization, C is the one for the polarization independent part, and Φ is a phase shift. The Stokes parameter for linear polarized radiation has here the form $s_2 = -\sin(4\varphi)/2$. Additionally, a photocurrent contribution depending on the radiation helicity is detected and described by $\sin(2\varphi)$. This part is fitted with the parameter D. The helicity sensitive current has opposite sign for left and right handed circularly polarized radiation and reverses its direction at opposite edges.

The photocurrent scales linear with the radiation intensity. This is shown in Fig. 29 (b) for sample G31A excited at $f = 3.3$ THz. The radiation intensity I is normalized to the maximum value obtained without attenuators. The photocurrent J is also normalized to the value obtained at maximal intensity. Individual photo-signal pulses, U_{sample}, follow the temporal structure of the excitation pulse, U_{ref}, closely with a responds time of picoseconds or less, see inset in Fig. 29 (b). The results shown so far are obtained at $T = 4.2$ K. Photocurrent are also detected at room temperature and are larger but have the same overall behaviour. This is shown for sample G30A in Fig. 29 (a) for currents measured at the left edge.

5.1.2 Discussion

In general, two effects, the photon drag and the photogalvanic, can be the cause for the photocurrent [38], see Eq.(22). As discussed in Sec. 2.2.3, at normal incidence the photon drag effect is very unlikely, and according to

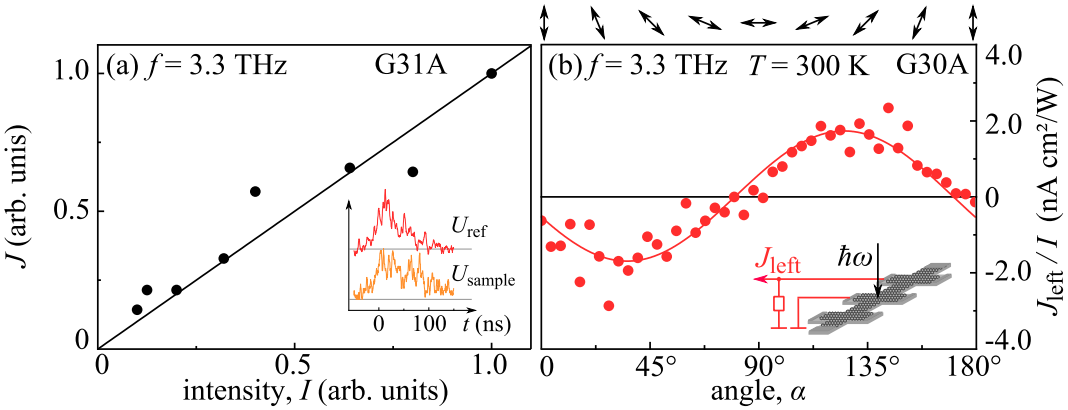

Figure 29: (a) Dependence of photocurrent J on radiation intensity I. Both values are normalized on ones for highest intensity. (b) Normalized photocurrent J/I measured at room temperature, $T = 300$ K. Data are obtained at left edge, (contact pair 7-6) at zero magnetic field for linearly polarized radiation in sample G30A. Solid lines show fits after Eq.(67). Inset shows experimental setup. The solid line through origin shows linear dependence.

symmetry arguments the photogalvanic effect is forbidden in infinite graphene. In micrometre sized Hall bar structures, as used in the experiments, however, graphene is finite. For this condition edges are illuminated, since the spot size of the THz laser is in the millimetre range. At the edges the symmetry is locally reduced and inversion symmetry is broken. Therefore, their illumination can give rise to photocurrents formed within the vicinity of edges.

Phenomenologically the current density along the edge oriented along the y direction is given for semi-infinite graphene ($x > 0$) by

$$j_{\text{edge}} = \chi(E_x E_y^* + E_y E_x^*) + \gamma i[\boldsymbol{E} \times \boldsymbol{E}^*]_z \tag{69}$$

with the linear photogalvanic coefficient χ and the circular photogalvanic coefficient γ. For the counted clockwise rotation of the linear polarization by α the term in the curved brackets is given by the Stokes parameter $s_2 = -\sin(2\alpha)$. As described in Sec. 2.2.1 the cross product of the electric field $i[\boldsymbol{E} \times \boldsymbol{E}^*]_z$ gives the degree of circularly polarized radiation $P_{circ} e_z E^2$, where $P_{circ} = \sin(2\varphi)$ is the Stokes parameter s_3. Equation (69) describes well the experimental findings. The phase Φ, observed in experiments, is not present in the phenomenological theory. It can be explained by misalignment, so are for some samples the edges not oriented along the y direction, Fig. 9 in Sec. 3.1.2. Consequently, the direction in which the current is examined does not correspond to the y direction.

To discuss the microscopic photocurrent origin, it is relevant to find possible optical transitions. Comparing the photon energy used, $\hbar\omega \approx 13.7$ meV, and typical Fermi energies known from magneto-transport measurements, $\varepsilon_F \approx 20...30$ meV reveals that only *indirect intraband* transitions are possible since the condition $\varepsilon_F \geq \hbar\omega$ is fulfilled. Other types transitions like *direct* or *indirect interband* with the conditions $\hbar\omega \geq 2\varepsilon_F$ and $2\varepsilon_F \geq \hbar\omega \geq \varepsilon_F$, respectively, are not present. *Indirect intraband* transitions are phonon or impurity assisted, and take place via different intermediate virtual states. They are also referred to as Drude-like free carrier absorption. In the following a semi-classical approach is used for the microscopic model based on scattering at the sample edge. The microscopic theoretical approaches is based on the modulation of the carrier density at the edge.

Microscopic Model The microscopic process [40, 94] responsible of the edge photocurrent formation is shown in Fig. 30. For the model p-type graphene is assumed, with a boundary along the y direction for semi-infinite graphene ($x > 0$). Linearly polarized radiation acts on the free carriers and drives them forth and back with the radiation frequency for the condition $\omega\tau > 1$. In infinite graphene, this movement of the carriers driven by the *ac* electric field does not lead to a current. The formation of a direct current arises only for carriers residing within the mean free path l away from the edge and for electric field orientations not oriented parallel or normal to the edge. For one half time period the carriers move away from the edge, while they are accelerated towards the edge for the second one. At the edge they can scatter by edge roughness. The scattered carriers moving away from the edge have then random velocities along the boundary. This diffuse scattering together with the time dependent motion of the carriers results in average in a direct current flow along the edge, see Fig. 30 (a). This current is sensitive to the electric field orientation. Considering holes, it is positive for $\alpha = 45°$ and negative for $\alpha = 135°$. At $\alpha = 0, 180°$ scattering on the edge is not present or at $\alpha = 90°$ it does not lead to an imbalance. As a consequence, no current is generated at these angles. The model for the photocurrent formation is in accordance with experiments, see Fig. 28, and phenomenological theory, see Eq.(69), both showing a $\sin(2\alpha)$ dependence.

The model can also be extended to circularly polarized radiation. In this case the retardation between the drift velocity of the carrier and the electric field lead to a curved trajectory. At the edge the carriers can scatter diffuse and

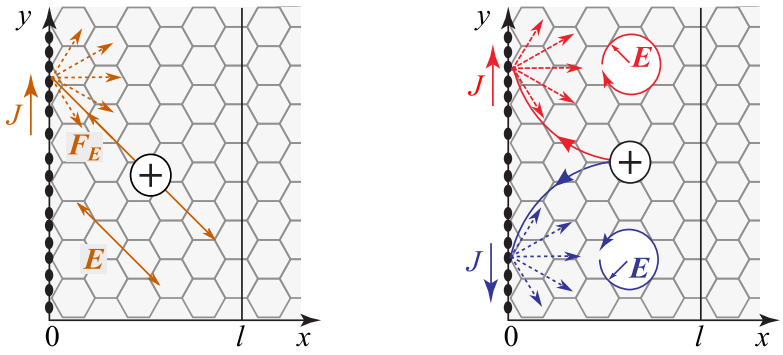

Figure 30: Sketch illustrating microscopic process of edge photocurrent generation by (a) linearly and (b) circularly polarized radiation. Motion of carriers, here holes, towards edge is shown by arrows. Their diffuse scattering is sketched by randomly oriented dashed arrows. Current formation within mean free path along edge results in linear or circular photogalvanic current. Adapted from Refs. [40, 94].

with the time dependent motion of the carriers, the edge current is generated, see Fig. 30 (b). The current reverses its sign when switching from right to left handed circular polarization. This circular photogalvanic current is also observed in the experiments, see Fig. 28 (b), and described by the second term in Eq.(69).

Microscopic Theory A microscopic theory for the edge current formation was developed in collaboration with the Ioffe Institute, St. Petersburg [40, 94].

The edge currents can be described by the variation of the current density N near the edge. It is caused by the component of the electric field vector, which is perpendicular to the edge. For an edge oriented along the y axis and considering the classical frequency range ($\hbar\omega \geq \varepsilon_\mathrm{F}$), the continuity equation is given by [40]

$$\frac{\partial \delta N}{\partial t} + \frac{\partial i_x}{\partial x} = 0, \tag{70}$$

with the electron flux density $\boldsymbol{i} = \boldsymbol{j}/e$, the current density $\boldsymbol{j}$, and the change in the electron density δN. The latter depends on the coordinate x, perpendicular to the edge, and time t and is given by $\delta N(x,t) = N(x,t) - N_0$. N_0 is the unperturbed electron density. The electron flux density $\boldsymbol{i}$ can contain a diffusive and a drift contribution. This can be expressed as

$$i_x = -\mathcal{D}\frac{\partial \delta N}{\partial t} + \frac{\sigma(\omega)}{e} E_x. \tag{71}$$

It includes a coefficient for diffusion $\mathcal{D}$, the electric field perpendicular to the edge E_x and the frequency dependent conductivity

$$\sigma(\omega) = \frac{e^2\varepsilon_{\rm F}}{\pi\hbar^2}\ \frac{\tau}{1-i\omega\tau}. \tag{72}$$

It depends on the unperturbed electron density via $\varepsilon_{\rm F} = \hbar v\sqrt{\pi N_0}$. Using boundary conditions $i_x(x=0)=0$ the change in the electron density is given as

$$\delta N(x) = \delta N_0\, e^{-(1-i)x/l_{\rm eff}}. \tag{73}$$

Here $l = v\tau$ is the mean free path, and $l_{\rm eff} = \sqrt{2\mathcal{D}/\omega} = l/\sqrt{\omega\tau}$ an effective length. The electron density variation is given by

$$\Delta N = \int_0^\infty \delta N dx = \frac{\sigma(\omega)E_x}{i\omega e} \tag{74}$$

Considering additionally the linear response in E_y, the total current along the edge can be formed by the change of the current density along x and is given by

$$J_y = 2\,Re[\frac{\partial\sigma(0)}{\partial N_0}\Delta N E_y^*] = \frac{e^3\tau^2}{(\pi\hbar)^2}\ \frac{\partial\varepsilon_{\rm F}^2}{\partial N_0}\ Re[\frac{E_x E_y^*}{i\omega(1-i\omega\tau)}]. \tag{75}$$

This contains linear and circular components of the photocurrent.

5.2 Edge Photocurrents in Quantum Hall Regime

This section presents results on edge photocurrents observed in the presence of an external magnetic field. After discussing the experimental results, the microscopic origin is clarified with a model and a theory.

5.2.1 Experimental Results

Application of an external magnetic field applied normal to the sample surface and parallel to the THz radiation modifies the photocurrent behaviour. By fixing the linear polarization to certain values α, the normalized photocurrent is measured as a function of the magnetic field up to $B_z = \pm 2$ T. This is shown in Fig. 31 for three polarizations states $\alpha = 36°$, 76° and 126° and for photocurrents measured at the left, panel (a), and the right edge, panel (b). The angles α are chosen is a way that they correspond approximately to minimal or maximal photocurrents for zero magnetic field. Thereby $\alpha = 36°$ and 126° correspond to maximal photocurrent measured at zero magnetic field, while 76° corresponds to an almost vanishing current.

While at $B_z = 0$ the photocurrent is sign alternating, in the presence of a magnetic field it becomes unidirectional. The photocurrent measured at the left edge, see Fig. 31 (a), shows a similar behaviour for all three angle α. By applying for example negative magnetic fields, the current becomes positive. This rectification of the current direction happens within 0.1 T and is independent from α. The photocurrent increases until it reaches a maximum at approximately $B_z = 0.5$ T. For higher magnetic fields, it starts to decrease with a smaller slope.

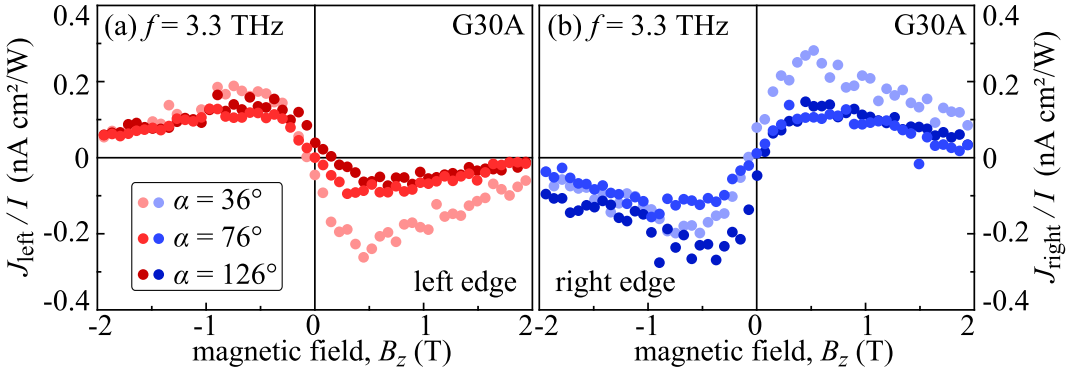

Figure 31: Normalized photocurrent J/I measured at (a) left edge, contact pair 8-6, and (b) right edge, contact pair 2-4, in dependence on an external magnetic field applied normal to sample surface and parallel to incident radiation of $f = 3.3$ THz for three polarizations states $\alpha = 36°$, 76° and 126°.

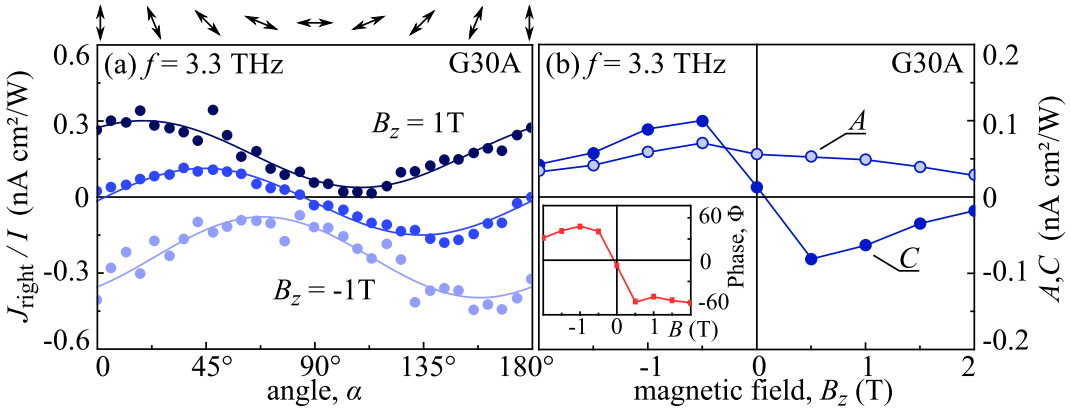

Figure 32: (a) Normalized photocurrent J/I measured at right edge, contact pair 2-4, at $B_z = \pm 1$ T and zero magnetic field for linearly polarized radiation with $f = 3.3$ THz. Solid lines show fits after Eq.(67). Arrows on top of both panels illustrates states of polarization for several angles α. (b) Magnetic field dependence of A and C. Inset shows magnetic field dependence of phase Φ.

By switching from negative to positive magnetic fields, the current changes its sign showing the same behaviour including a maximum at same absolute value of B_z. The current measured at the right edge, see Fig. 31 (b), has just the opposite behaviour compared to the left edge. Importantly, the photocurrent has consistently opposite direction at opposite edges, revealing that edge currents are generated. This behaviour is the same for all studied samples and all values α.

For a more detailed analysis of the photocurrent behaviour in the magnetic field, polarization dependencies are measured at fixed B_z field values. Figure 32 (a) shows that in contrast to the sign alternating photocurrent observed at zero magnetic field, the photocurrent direction is now determined by the sign of B_z. For a positive magnetic field, here $B_z = 1$ T, the normalized photocurrent measured at the right edge, is shifted to positive values. The dependence on α qualitatively changes, but can still be fitted with Eq.(67). The fit reveals that the polarization independent part C becomes larger than the dependent part A, which decreases only slightly. Also, the phase Φ changes drastically and the normalized photocurrent is almost described by a $\cos(2\alpha)$ behaviour. The normalized photocurrent measured at $B_z = -1$ T behaves just opposite and shifts to negative values.

The fit parameters A and C for different values of B_z are shown in Fig. 32 (b). The figure reveals the different behaviour of the photocurrent in the presence of a magnetic field. Its direction is determined by the sign of B_z, indicated by the fact that the parameter C becomes larger than A. The observed change

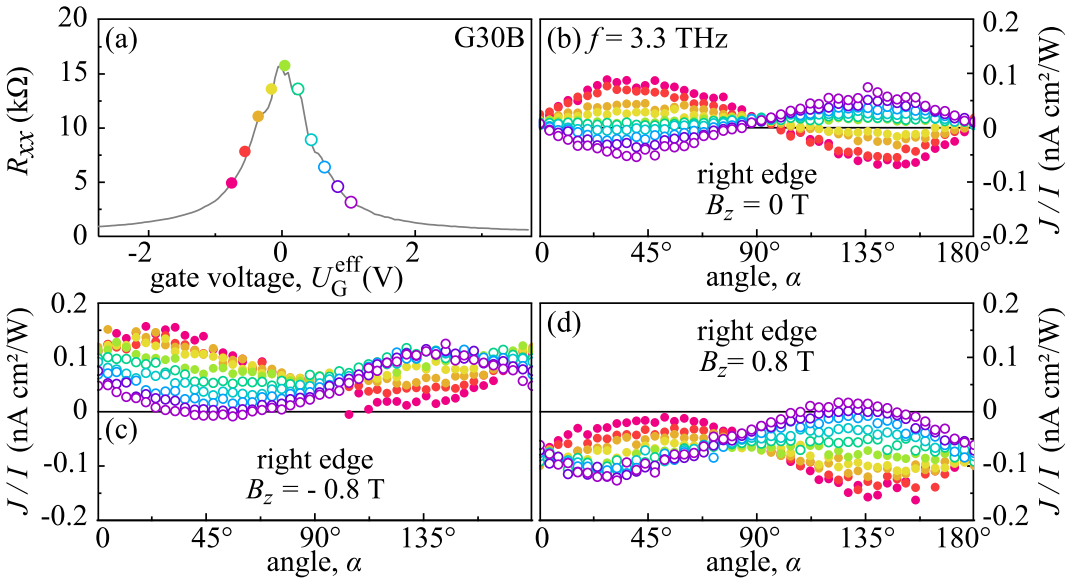

Figure 33: (a) Longitudinal resistance R_{xx} as function of effective gate voltage U_G^{eff}. Colour dots indicate gate voltages used in photocurrent measurements. (b)-(d) Dependence of normalized photocurrent J/I on orientation of radiation electric field vector for gate voltages $U_G^{eff} = -0.8$ to 1.0 V. Data are obtained for (b) $B_z = 0$ T, (c) $B_z = -0.8$ T, and (d) $B_z = -0.8$ T. Open and solid circles correspond to electrons and holes, respectively.

in the phase Φ is shown in the inset. It increases from almost zero at $B_z = 0$ to $\pm 60°$.

By applying a back gate voltage, the photocurrent is studied for different carrier densities n (positive effective gate voltages) and p (negative effective gate voltages). The carrier densities are obtained from Hall slops, see e.g. Fig. 10 in Sec. 3.1.2. The longitudinal resistance in dependence on the effective gate voltage is shown in Fig. 33 (a), in which the voltages used for the photocurrent measurements are highlighted with coloured dots. For these voltages, the photocurrent dependence on α is shown in Fig. 33 (b) at zero magnetic field measured at the right edge. The current direction is determined by the electric field vector and reverses when changing the carrier densities from n (electrons, circles) to p (holes, dots). The photocurrent dependencies on α are fitted well with Eq.(67). Figures 33 (c) and (d) show the photocurrent behaviour for magnetic fields of $B_z = \pm 0.8$ T. Now the direction of the edge photocurrent remains the same for electrons and holes. It is not determined by the carrier type, but only by the sign of B_z. Although it still depends on the direction of the electric field vector, it almost does not changes its sign.

By irradiating the samples with elliptically polarized radiation the depen-

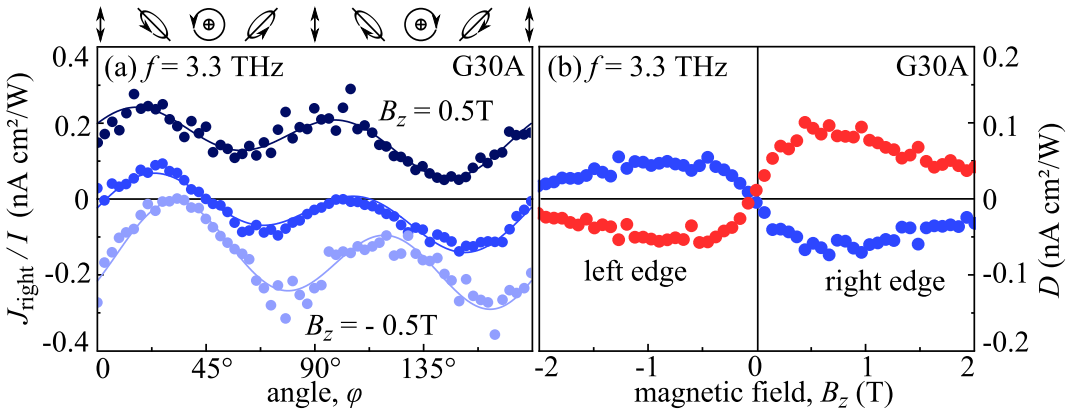

Figure 34: (a) Normalized photocurrent J/I measured at right edge, contact pair 2-4 at $B_z = \pm 1$ T and zero magnetic field for circularly polarized radiation with $f = 3.3$ THz. Solid lines show fits after Eq.(68). Ellipses on top of both panels illustrates states of polarization for several angles φ. (b) Magnetic field dependence of fitted helicity sensitive contribution D for left and right edge.

dence is modified but the overall behaviour is the same. Figure 34 (a) reveals that the sign alternating photocurrent at $B_z = 0$ becomes unidirectional in the presence of a magnetic field. For $B_z = 0.5$ T the normalized photocurrent is shifted to positive values, and for $B_z = -0.5$ T to negative values. Fitting the data with Eq.(68) reveals that again the polarization independent part C becomes larger than polarization dependent part A. Besides the phase shift, also the helicity sensitive current increases. For a more detailed analysis of the helicity dependent contribution, the magnetic field is swept between ± 2 T and the photocurrent is measured for left and right handed circularly polarized radiation. For these measurements D can be calculated with

$$D = [J/I(\varphi = 45°) - J/I(\varphi = 135°)]/2. \tag{76}$$

Its dependence on the magnetic field is shown in Fig. 34 (b) for the left and the right edge. The helicity sensitive current has consistently opposite direction for left and right edge and behaves odd in the magnetic field.

5.2.2 Discussion

To understand the origin of possible microscopic processes causing the observed modification of the photocurrent, first the role of the magnetic field on the electronic dispersion is considered. Then a microscopic model and theory, developed in collaboration with Prof. Dr. Sergey A. Tarasenko[6], is used to

[6] Ioffe Institute, St. Petersburg, Russia

illustrate the current origin.

When suspended to a perpendicular external magnetic field B_z the energy spectrum of graphene changes. The magnetic field leads to quantized Landau levels [3, 95]

$$\varepsilon_n = \mathrm{sgn}(n)\, v_\mathrm{F} \sqrt{2e\hbar B_z\, |n|} \tag{77}$$

in which n is the integer number, which denotes the Landau level number. A special feature of graphene is the presence of a zero-energy ($n = 0$) Landau level, which is shared by both, electrons and holes. The derived spectrum is shown in Fig. 35 for $B_z = 1$ T in the energy range between ± 50 meV. The dispersion is plotted against the reciprocal magnetic length l_B. The Landau levels of the bulk carriers ($\boldsymbol{k} l_B \gg 1$) are two-fold degenerate by the valley index. This degeneracy is lifted at the boundary ($\boldsymbol{k} l_B \sim 1$). Being independent in the bulk, the Weyl Hamiltonians are coupled at the edge and symmetric and anti-symmetric combinations of the valley states are formed. Here, the symmetric states are denoted as n^-, the anti-symmetric ones as n^+, see Fig. 35 for Landau levels up to $n = \pm 2$. While in the bulk the energy of the carriers is $\boldsymbol{k}$ independent, it depends on $\boldsymbol{k}$ at the boundary. This $\boldsymbol{k}$ dependence results in a non-zero edge velocity being opposite for electrons and holes [95].

The spin degeneracy is lifted in the magnetic field due to Zeeman splitting. In graphene it is given by $\varepsilon_\mathrm{Z} = g\mu_\mathrm{B} B_z$, where μ_B is the Bohr magneton, and $g = 2$ is the g-factor. At $B_z = 1$ T the splitting is only $\varepsilon_\mathrm{Z} = 0.12$ meV, which is negligible when compared to the Landau level splitting [3].

In this quantized energy dispersion, direct optical transitions are possible if the energy distance between Landau levels below and above ε_F and the incident photon energy match. For the photocurrent measurements a radiation frequency of $f = 3.3$ THz is used, with photons having a energy of $\hbar\omega \approx 13.7$ meV. Magneto-transport measurements, see Sec. 3.1.2, reveal that for the samples studied the Fermi levels are in the range of $\varepsilon_\mathrm{F} \approx 20 - 30$ meV. Thus, for magnetic fields above $B_z \approx 0.5 - 1.1$ T, the corresponding Fermi level lies between the $n = 0$ and $n = 1$ bulk Landau levels. For these conditions optical transitions are forbidden between bulk Landau levels and only possible within the edge channels.

Microscopic Model Microscopically, the incident photons are absorbed by carriers localized in the edge channels. This is illustrated in Fig. 35 (a). Having

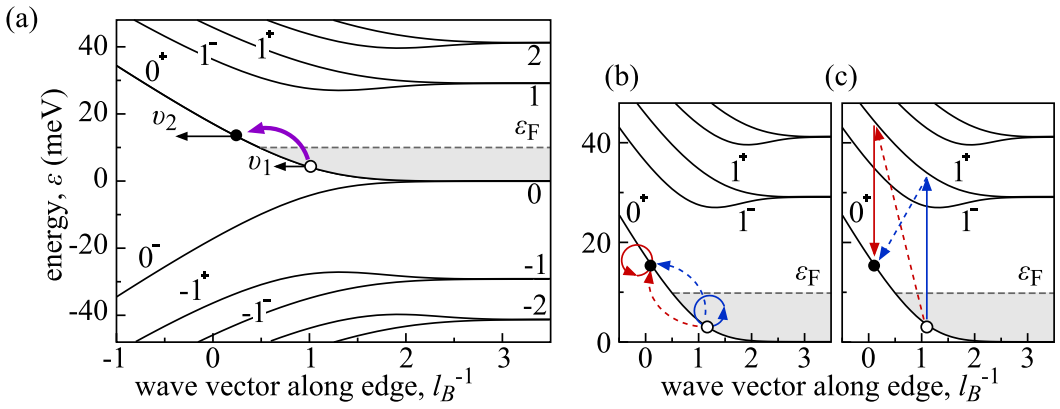

Figure 35: Schematic illustration of terahertz radiation induced edge current in graphene quantum Hall insulator. (a) Calculated spectrum of Landau levels in graphene with an armchair edge for $B_z = 1$ T, dashed line illustrates position of Fermi level in n-type sample. The photocurrent emerges because of electron transition between states with different velocities under absorption of a photon (thick arrow). The zoom of electron dispersion with illustration of possible mechanisms of intraband photon absorption through intermediate states belonging to (b) same or (c) another Landau level. The solid lines illustrate interaction with electro-magnetic field, whereas dashed lines stand for scattering on static impurities or phonons.

the initial average velocity v_1, the edge carriers make an optical transition to states within the same chiral edge channel. In the final state they have an average velocity v_2. This difference in the initial and final velocities v_1 and v_2 can result in formation of a direct electric current along the edge.

The intraband photon absorption within the edge channels is a second order process, which takes place only through intermediate states either belonging to the same or another Landau level [66]. Both processes are illustrated in Fig. 35 (b) and (c). The absorption process requires the interaction with the electro-magnetic field, solid line, and scattering, dashed line. The carriers can scatter, e.g., with static impurities or phonons.

Microscopic Theory The edge photocurrent density is given by

$$j_{\rm edge} = e\frac{4\pi}{\hbar}\sum_{\boldsymbol{k},\boldsymbol{k}'}[\tau^*(\varepsilon_{\boldsymbol{k}'})v_{\boldsymbol{k}'} - \tau^*(\varepsilon_{\boldsymbol{k}})v_{\boldsymbol{k}}]\times \\ \times|M_{\boldsymbol{k}'\boldsymbol{k}}|^2(f_{0,\boldsymbol{k}} - f_{0,\boldsymbol{k}'})\delta(\varepsilon_{\boldsymbol{k}'} - \varepsilon_{\boldsymbol{k}} - \hbar\omega), \tag{78}$$

where $\boldsymbol{k}$ and $\boldsymbol{k}'$ denote the wave vectors of the initial and final state, $\varepsilon_{\boldsymbol{k}}$ is their energy, $v_{\boldsymbol{k}}$ is the average velocity of the electron with wave vector $\boldsymbol{k}$, and $M_{\boldsymbol{k}'\boldsymbol{k}}$ is the matrix element for intraband transitions. Electrons excited within the edge channels relax with the time τ^*. Edge photocurrent occurs only if the

product $v\tau^*$ is different for initial and final states. The equilibrium distribution function $f_{0,\boldsymbol{k}}$ is obtained by solving the kinetic Boltzmann equation.

In the regime $\hbar\omega \ll \varepsilon_\mathrm{F}$ the edge photocurrent density is proportional to the one-dimensional absorption coefficient η [66]

$$j_\mathrm{edge} = e\left[\frac{\partial\tau^*}{\partial\varepsilon}v_\mathrm{F} + \tau^*\frac{\partial v}{\partial\varepsilon}\right]\eta I\ . \tag{79}$$

Here v_F is the Fermi velocity, I is the radiation intensity, and ηI is the power absorbed by an edge length unit.

Equation (79) can be further simplified by assuming that the relaxation time is independent of ε_F and hence $\partial\tau^*/\partial\varepsilon = 0$. Than the current density is derived as

$$j_\mathrm{edge} = 8\sqrt{2}\,\Lambda(\varepsilon_\mathrm{F}, \boldsymbol{E})\,\frac{\alpha' e}{n_\omega}\left(\frac{\tau^*}{\tau_0}\right)\frac{l_B^2}{\hbar v_0\sqrt{N}}I. \tag{80}$$

Here α' is the fine structure constant, n_ω the refractive index, v_0 the electron velocity in the bulk of graphene, N the carrier concentration, and Λ a dimensionless coefficient determined by the structure of electron states. The parameter τ_0 is the momentum relaxation time of carriers near the graphene edge at $B_z = 0$.

Model and theory describes well the experimental findings: The observed photocurrent is a pure edge current, since it has opposite sign at opposite edges, see Figs. 31. Furthermore, its direction is only defined by the sign of B_z. Even chancing the carrier density from n to p does not affect the current direction, see Fig. 33. This experimental observation is in accordance with theory. When calculating the hole photocurrent using Eq.(79), e is replaced by $-e$. From the dispersion of Landau levels follows that v is replaced by $-v$. Hence the sign of j_edge does not change.

Comparing theory with the amplitude of j_edge obtained from experiments, see Fig. 31, yields that the life time of the excited carrier τ^* is two orders of magnitude larger than the momentum relaxation time of carriers near the graphene edge τ_0. The ration between both is $\tau^*/\tau_0 \approx 100 - 200$.

In experiments also a dependence of the edge photocurrent on the electric field orientation is observed. While the photocurrent at $B_z = 0$ is maximal at $\alpha = 45°$ and 135°, see Sec. 5.1 for details, the behaviour changes at $B_z \neq 0$. The photocurrent is maximal at $\alpha \approx 0$ and 180° and minimal at $\alpha \approx 90°$, see Fig. 32 (a), which is seen in the change of Φ in Fig. 32 (b). This can

be explained when considering that the absorption η depends on the electric field vector. For intermediate states in the same Landau level the absorption is sensitive only to the component of electric field that is parallel to the edge. For intermediate states in another Landau level the absorption is possible for electric field components parallel and normal to the edge. For an edge being parallel to the y axis the absorption coefficient η can be written as

$$\eta(\boldsymbol{E}) = \eta_{yy}|E_y|^2 + \eta_{xx}|E_x|^2 - \eta_{\mathrm{circ}}P_{\mathrm{circ}} \,. \tag{81}$$

with $\boldsymbol{E}$ being the electric field vector, and $P_{\mathrm{circ}} = i(E_x E_y^* - E_x^* E_y)$ being the degree of circular polarization. This describes well the experimental findings, that the photocurrent is maximal if the electric field vector is oriented along the edge and that a photocurrent observed in the quantum Hall regime is sensitive to the radiation helicity.

6 Conclusion

Within this thesis it was demonstrated that the excitation of systems, which are characterized by a linear dispersion, with polarized terahertz radiation results in the generation of optoelectronic phenomena. In three dimensional topological insulators several nonlinear effects were observed, among these are the linear photogalvanic and photon drag effect [44], the circular photogalvanic effect [45], and the trigonal photon drag effect [47]. In high mobility graphene edge photogalvanic effects were verified in two different regimes, the semi-classical and the quantum Hall one. All experimental results and their discussion were shown in two chapters.

In Chap. 4, results on Bi_2Te_3- and Sb_2Te_3-based 3D TIs were presented, studied at room temperature and for a wide range of excitation frequencies. Due to symmetry filtration between the centrosymmetric bulk and the non-centrosymmetric surface, a photogalvanic current is excited in the surface states [44]. It was verified, that the role of a competing photon drag current, being allowed in the bulk states too, is excluded by measurements using front and back illumination. It was shown, that the photocurrents give insight in the high frequency transport properties of the materials and allow an estimation of scattering times and mobilities [45]. Moreover, it was stated that the photogalvanic effect can be applied to characterized the materials and provides information on the local domain orientation and uniformity of the high frequency transport [46]. Furthermore, photocurrents were generated in two excitation regimes: In the lower THz range, where Drude-like free carrier absorption dominates and the current formation was treated semi-classically, and in the higher THz range, where direct optical transitions, possibly from the Dirac cone into bulk bands, dominate. For the second case, a helicity sensitive contribution to the current is observed [45]. Changing the experimental geometry allowed the observation of the trigonal photon drag effect, which is caused by the additional transfer of the in-plane photon momentum [47]. All experimental findings are supported by models and microscopic theories, which were developed in collaboration with the Ioffe Institute St. Petersburg and which describe all characteristics features.

For future investigations of these systems especially the higher frequency range is of particular interest and to study in this range not only the direct optical transitions but also the crossover between semi-classical and quantum mechanical regime. The photocurrent origin, caused by direct optical transi-

tions is in these materials not yet understood completely, and requires a more careful investigation. Possible approaches could be a more detailed frequency dependence [45] or tuning the Fermi energy by top gate structures, as it was shown most recently [91, 96].

In Chap. 5, results on edge photocurrents in high mobility graphene were presented. It was shown that the current at zero magnetic field stems from scattering in the vicinity of the edge and is formed in a narrow strip given by the mean free path. The discussion revealed that in this case the edge photocurrent direction is determined by the polarization and the carrier type. Strikingly and in contrast to this, the results further revealed that for graphene being in the quantum Hall regime, the observed edge currents are determined solely by the sign of the magnetic field. The study demonstrated, that they are generated by optical transitions within the chiral edge channels. All these findings are supported by a microscopic theory, also developed in collaboration with the Ioffe Institute St. Petersburg.

This new approach to study chiral edge currents by terahertz excitation can be a starting point for further investigations, e.g. of other materials. In graphene experiments on edge currents for higher Fermi levels, i.e. near or between Landau levels, are of particular interest, since, e.g., theory predicts different polarization dependencies of the absorption for these cases. Also, the condition when the photon energy is comparable to the cyclotron gap is of interest, since there cyclotron resonance in the quantized bulk states can contribute to the current formation [97, 98].

References

[1] K. S. Novoselov, A. K. Geim, S. V. Morozov, D. Jiang, Y. Zhang, S. V. Dubonos, I. V. Grigorieva, and A. A. Firsov, *Electric Field Effect in Atomically Thin Carbon Films*, Science **306**, 666 (2004).

[2] A. H. Castro Neto, F. Guinea, N. M. R. Peres, K. S. Novoselov, and A. K. Geim, *The electronic properties of graphene*, Rev. Mod. Phys. **81**, 109 (2009).

[3] S. Das Sarma, S. Adam, E. H. Hwang, and E. Rossi, *Electronic transport in two-dimensional graphene*, Rev. Mod. Phys. **83**, 407 (2011).

[4] X. Song, J. Hu, and H. Zeng, *Two-dimensional semiconductors: recent progress and future perspectives*, J. Mater. Chem. C **1**, 2952 (2013).

[5] C. L. Kane and E. J. Mele, *Quantum Spin Hall Effect in Graphene*, Phys. Rev. Lett. **95**, 226801 (2005).

[6] M. Z. Hasan and C. L. Kane, *Colloquium: Topological insulators*, Rev. Mod. Phys. **82**, 3045 (2010).

[7] X.-L. Qi and S.-C. Zhang, *The quantum spin Hall effect and topological insulators*, Phys. Today **63**, 33 (2010).

[8] S.-Q. Shen, *Topological Insulators: Dirac Equation in Condensed Matters* (Springer, Berlin Heidelberg, 2012).

[9] Y. Ando, *Topological Insulator Materials*, J. Phys. Soc. Jpn. **82**, 102001 (2013).

[10] F. D. M. Haldane, *Model for a Quantum Hall Effect without Landau Levels: Condensed-Matter Realization of the "Parity Anomaly"*, Phys. Rev. Lett. **61**, 2015 (1988).

[11] K. v. Klitzing, G. Dorda, and M. Pepper, *New Method for High-Accuracy Determination of the Fine-Structure Constant Based on Quantized Hall Resistance*, Phys. Rev. Lett. **45**, 494 (1980).

[12] B. I. Halperin, *Quantized Hall conductance, current-carrying edge states, and the existence of extended states in a two-dimensional disordered potential*, Phys. Rev. B **25**, 2185 (1982).

[13] C. L. Kane and E. J. Mele, Z_2 *Topological Order and the Quantum Spin Hall Effect*, Phys. Rev. Lett. **95**, 146802 (2005).

[14] B. A. Bernevig and S.-C. Zhang, *Quantum Spin Hall Effect*, Phys. Rev. Lett. **96**, 106802 (2006).

[15] R. Jackiw and C. Rebbi, *Solitons with fermion number 1/2*, Phys. Rev. D **13**, 3398 (1976).

[16] B. A. Bernevig, T. L. Hughes, and S.-C. Zhang, *Quantum Spin Hall Effect and Topological Phase Transition in HgTe Quantum Wells*, Science **314**, 1757 (2006).

[17] M. König, S. Wiedmann, C. Brüne, A. Roth, H. Buhmann, L. Molenkamp, X.-L. Qi, and S.-C. Zhang, *Quantum Spin Hall Insulator State in HgTe Quantum Wells*, Science **318**, 766 (2007).

[18] L. Fu, C. L. Kane, and E. J. Mele, *Topological Insulators in Three Dimensions*, Phys. Rev. Lett. **98**, 106803 (2007).

[19] J. E. Moore, *The birth of topological insulators*, Nature **464**, 194 (2010).

[20] L. Fu and C. L. Kane, *Topological insulators with inversion symmetry*, Phys. Rev. B **76**, 045302 (2007).

[21] H. Zhang, C.-X. Liu, X.-L. Qi, X. Dai, Z. Fang, and S.-C. Zhang, *Topological insulators in Bi_2Se_3, Bi_2Te_3 and Sb_2Te_3 with a single Dirac cone on the surface*, Nature Phys. **5**, 438 (2009).

[22] P. A. M. Dirac, *The quantum theory of the electron*, Proc. R. Soc. B **117**, 610 (1928).

[23] K. Novoselov, A. Geim, S. Morozov, D. Jiang, M. I. Katsnelson, I. Grigorieva, S. Dubonos, and A. Firsov, *Two-dimensional gas of massless Dirac fermions in graphene*, Nature **438**, 197 (2005).

[24] D.-X. Qu, Y. S. Hor, J. Xiong, R. J. Cava, and N. P. Ong, *Quantum Oscillations and Hall Anomaly of Surface States in the Topological Insulator Bi_2Te_3*, Science **329**, 821 (2010).

[25] T. Ginley, Y. Wang, and S. Law, *Topological Insulator Film Growth by Molecular Beam Epitaxy: A Review*, Crystals **6**, 154 (2016).

[26] J. H. Bardarson and J. E. Moore, *Quantum interference and Aharonov-Bohm oscillations in topological insulators*, Rep. Prog. Phys. **76**, 056501 (2013).

[27] J. Ziegler, R. Kozlovsky, C. Gorini, M.-H. Liu, S. Weishäupl, H. Maier, R. Fischer, D. A. Kozlov, Z. D. Kvon, N. Mikhailov, S. A. Dvoretsky, K. Richter, and D. Weiss, *Probing spin helical surface states in topological HgTe nanowires*, Phys. Rev. B **97**, 035157 (2018).

[28] Y. Chen, J. Analytis, J.-H. Chu, Z. Liu, S.-K. Mo, X. Qi, H. Zhang, D. Lu, X. Dai, Z. Fang, S. Zhang, I. Fisher, Z. Hussain, and Z.-X. Shen, *Experimental Realization of a Three-Dimensional Topological Insulator, Bi_2Se_3*, Science **325**, 5937 (2009).

[29] D. Hsieh, D. Qian, L. Wray, Y. Xia, Y. Hor, R. Cava, and M. Hasan, *A topological Dirac insulator in a quantum spin Hall phase*, Nature **452**, 970 (2008).

[30] D. Hsieh, Y. Xia, D. Qian, L. Wray, F. Meier, J. H. Dil, J. Osterwalder, L. Patthey, A. V. Fedorov, H. Lin, A. Bansil, D. Grauer, Y. S. Hor, R. J. Cava, and M. Z. Hasan, *Observation of Time-Reversal-Protected Single-Dirac-Cone Topological-Insulator States in Bi_2Te_3 and Sb_2Te_3*, Phys. Rev. Lett. **103**, 146401 (2009).

[31] D. Hsieh, Y. Xia, D. Qian, L. Wray, J. H. Dil, F. Meier, J. Osterwalder, L. Patthey, J. G. Checkelsky, N. P. Ong, A. V. Fedorov, H. Lin, A. Bansil, D. Grauer, Y. S. Hor, R. J. Cava, and M. Z. Hasan, *A tunable topological insulator in the spin helical Dirac transport regime*, Nature **460**, 1101 (2009).

[32] Y. Xia, D. Qian, D. Hsieh, L. Wray, A. Pal, H. Lin, A. Bansil, D. Grauer, Y. Hor, R. Cava, and M. Hasan, *Observation of a large-gap topological insulator class with a single Dirac cone on the surface*, Nature Phys. **5**, 398 (2009).

[33] J. C. Johannsen, S. Ulstrup, F. Cilento, A. Crepaldi, M. Zacchigna, C. Cacho, I. C. E. Turcu, E. Springate, F. Fromm, C. Raidel, T. Seyller, F. Parmigiani, M. Grioni, and P. Hofmann, *Direct View of Hot Carrier Dynamics in Graphene*, Phys. Rev. Lett. **111**, 027403 (2013).

[34] S. Ulstrup, J. C. Johannsen, A. Crepaldi, F. Cilento, M. Zacchigna, C. Cacho, R. T. Chapman, E. Springate, F. Fromm, C. Raidel, T. Seyller, F. Parmigiani, M. Grioni, and P. Hofmann, *Ultrafast electron dynamics in epitaxial graphene investigated with time- and angle-resolved photoemission spectroscopy*, Jour. Phys.: Cond. Matt. **27**, 164206 (2015).

[35] K. Kuroda, J. Reimann, J. Güdde, and U. Höfer, *Generation of Transient Photocurrents in the Topological Surface State of Sb_2Te_3 by Direct Optical Excitation with Midinfrared Pulses*, Phys. Rev. Lett. **116**, 076801 (2016).

[36] K. Kuroda, J. Reimann, K. A. Kokh, O. E. Tereshchenko, A. Kimura, J. Güdde, and U. Höfer, *Ultrafast energy- and momentum-resolved surface Dirac photocurrents in the topological insulator Sb_2Te_3*, Phys. Rev. B **95**, 081103 (2017).

[37] D. Panna, R. Marjieh, E. Sabag, L. Rybak, A. Ribak, A. Kanigel, and A. Hayat, *Linear-optical access to topological insulator surface states*, Appl. Phys. Lett. **110**, 212103 (2017).

[38] S. Ganichev and W. Prettl, *Intense Terahertz Excitation of Semiconductors* (Oxford Univ. Press, Oxford, 2006).

[39] E. L. Ivchenko and S. D. Ganichev, *Spin-Photogalvanics*, edited by M. I. Dyakonov (Springer, Berlin Heidelberg, 2017).

[40] M. Glazov and S. Ganichev, *High frequency electric field induced nonlinear effects in graphene*, Phys. Rep. **535**, 101 (2014).

[41] J. McIver, D. Hsieh, H. Steinberg, P. Jarillo-Herrero, and N. Gedik, *Control over topological insulator photocurrents with light polarization*, Nature Nanotech. **7**, 96 (2012).

[42] C. Kastl, T. Guan, X. Y. He, K. H. Wu, Y. Q. Li, and A. W. Holleitner, *Local photocurrent generation in thin films of the topological insulator Bi_2Se_3*, Appl. Phys. Lett. **101**, 251110 (2012).

[43] L. Braun, G. Mussler, A. Hruban, M. Konczykowski, T. Schumann, M. Wolf, M. Münzenberg, L. Perfetti, and T. Kampfrath, *Ultrafast photocurrents at the surface of the three-dimensional topological insulator Bi_2Se_3*, Nature Comm. **7**, 13259 (2016).

[44] P. Olbrich, L. E. Golub, T. Herrmann, S. N. Danilov, H. Plank, V. V. Bel'kov, G. Mussler, C. Weyrich, C. M. Schneider, J. Kampmeier, D. Grützmacher, L. Plucinski, M. Eschbach, and S. D. Ganichev, *Room-Temperature High-Frequency Transport of Dirac Fermions in Epitaxially Grown Sb_2Te_3- and Bi_2Te_3-Based Topological Insulators*, Phys. Rev. Lett. **113**, 096601 (2014).

[45] H. Plank, J. Pernul, S. Gebert, S. N. Danilov, J. König-Otto, S. Winnerl, M. Lanius, J. Kampmeier, G. Mussler, I. Aguilera, D. Grützmacher, and S. D. Ganichev, *Infrared/Terahertz Spectra of the Photogalvanic Effect in (Bi,Sb)Te based Three-Dimensional Topological Insulators*, Phys. Rev. Materials **2**, 024202 (2018).

[46] H. Plank, S. N. Danilov, V. V. Bel'kov, V. A. Shalygin, J. Kampmeier, M. Lanius, G. Mussler, D. Grützmacher, and S. D. Ganichev, *Opto-electronic Characterization of Three Dimensional Topological Insulators*, J. Appl. Phys. **120**, 165301 (2016).

[47] H. Plank, L. E. Golub, S. Bauer, V. V. Bel'kov, T. Herrmann, P. Olbrich, M. Eschbach, L. Plucinski, C. M. Schneider, J. Kampmeier, M. Lanius, G. Mussler, D. Grützmacher, and S. D. Ganichev, *Photon Drag Effect in* $(Bi_{1-x}Sb_x)_2Te_3$ *Three-Dimensional Topological Insulators*, Phys. Rev. B **93**, 125434 (2016).

[48] V. G. Bagrov and D. Gitman, *The Dirac equation and its solutions*, Vol. 4 (De Gruyter, Berlin, Germany, 2014).

[49] S.-Q. Shen, W.-Y. Shan, and H.-Z. Lu, *Topological insulator and the Dirac equation*, SPIN **01**, 33 (2011).

[50] C. D. Anderson, *The Positive Electron*, Phys. Rev. **43**, 491 (1933).

[51] H. Weyl, *Elektron und Gravitation. I*, Zeitschrift für Physik **56**, 330 (1929).

[52] P. R. Wallace, *The Band Theory of Graphite*, Phys. Rev. **71**, 622 (1947).

[53] R. Saito, G. Dresselhaus, and M. S. Dresselhaus, *Physical properties of carbon nanotubes* (Imperial College Press, London, 2007).

[54] M. B. Smith and J. March, *March's advanced organic chemistry*, 6th ed. (Wiley, New York, United States, 2007).

[55] E. Malic and A. Knorr, *Graphene and Carbon Nanotubes: Ultrafast Relaxation Dynamics and Optics* (Wiley-VCH, 2013).

[56] S. Reich, J. Maultzsch, C. Thomsen, and P. Ordejon, *Tight-binding description of graphene*, Phys. Rev. B **66**, 035412 (2002).

[57] P. M. Lee and L Pincherle, *The Electronic Band Structure of Bismuth Telluride*, Proc. R. Soc. **81**, 461 (1963).

[58] Y. Zhang, K. He, C.-Z. Chang, C.-L. Song, L.-L. Wang, X. Chen, J.-F. Jia, Z. Fang, X. Dai, W.-Y. Shan, S.-Q. Shen, Q. Niu, X.-L. Qi, S.-C. Zhang, X.-C. Ma, and Q.-K. Xue, *Crossover of the three-dimensional topological insulator Bi_2Se_3 to the two-dimensional limit*, Nature Phys. **6**, 584 (2010).

[59] V. I. Belinicher and B. I. Sturman, *The photogalvanic effect in media lacking a center of symmetry*, Sov. Phys. Usp. **23**, 199 (1980).

[60] A. F. Gibson, M. F. Kimmitt, and A. C. Walker, *Photon drag in germanium*, Appl. Phys. Lett. **17**, 75 (1970).

[61] E. L. Ivchenko, *Optical Spectroscopy of Semiconductor Nanostructures* (Alpha Science International Ltd, Harrow, UK, 2005).

[62] L. Boltzmann, *Lectures on Gas Theory* (Univ. of California Press, Berkeley, 1964).

[63] C. Liu, T. L. Hughes, X.-L. Qi, K. Wang, and S.-C. Zhang, *Quantum Spin Hall Effect in Inverted Type-II Semiconductors*, Phys. Rev. Lett. **100**, 236601 (2008).

[64] I. Knez, R.-R. Du, and G. Sullivan, *Evidence for Helical Edge Modes in Inverted* InAs/GaSb *Quantum Wells*, Phys. Rev. Lett. **107**, 136603 (2011).

[65] S. Mueller, A. N. Pal, M. Karalic, T. Tschirky, C. Charpentier, W. Wegscheider, K. Ensslin, and T. Ihn, *Nonlocal transport via edge states in InAs/GaSb coupled quantum wells*, Phys. Rev. B **92**, 081303 (2015).

[66] S. A. Tarasenko, *Orbital mechanism of the circular photogalvanic effect in quantum wells*, JETP Lett. **85**, 182 (2007).

[67] S. A. Tarasenko, *Direct current driven by ac electric field in quantum wells*, Phys. Rev. B **83**, 035313 (2011).

[68] H. Plank, S. A. Tarasenko, T. Hummel, G. Knebl, R. Pfeffer, M. Kamp, S. Höfling, and S. D. Ganichev, *Circular and linear photogalvanic effects in type-II GaSb/InAs quantum well structures in the inverted regime*, Physica E **85**, 193 (2017).

[69] J. Karch, P. Olbrich, M. Schmalzbauer, C. Zoth, C. Brinsteiner, M. Fehrenbacher, U. Wurstbauer, M. M. Glazov, S. A. Tarasenko, E. L. Ivchenko, D. Weiss, J. Eroms, R. Yakimova, S. Lara-Avila, S. Kubatkin, and S. D. Ganichev, *Dynamic Hall Effect Driven by Circularly Polarized Light in a Graphene Layer*, Phys. Rev. Lett. **105**, 227402 (2010).

[70] C. Jiang, V. A. Shalygin, V. Y. Panevin, S. N. Danilov, M. M. Glazov, R. Yakimova, S. Lara-Avila, S. Kubatkin, and S. D. Ganichev, *Helicity dependent photocurrents in graphene layers excited by midinfrared radiation of a CO_2 laser*, Phys. Rev. B **84**, 125429 (2011).

[71] J. Karch, P. Olbrich, M. Schmalzbauer, C. Brinsteiner, U. Wurstbauer, M. Glazov, S. Tarasenko, E. Ivchenko, D. Weiss, J. Eroms, and S. Ganichev, *Photon helicity driven electric currents in graphene*, arXiv:1002.1047v1 (2010).

[72] J. Krumrain, G. Mussler, S. Borisova, T. Stoica, L. Plucinski, C. Schneider, and D. Grützmacher, *MBE growth optimization of topological insulator Bi_2Te_3 films*, J. Crystal Growth **324**, 115 (2011).

[73] S. Borisova, J. Krumrain, M. Luysberg, G. Mussler, and D. Grützmacher, *Mode of Growth of Ultrathin Topological Insulator Bi_2Te_3 Films on Si(111) Substrates*, Cryst. Growth Des. **12**, 6098 (2012).

[74] L. Plucinski, A. Herdt, S. Fahrendorf, G. Bihlmayer, G. Mussler, S. Döring, J. Kampmeier, F. Matthes, D. E. Bürgler, D. Grützmacher, S. Blügel, and C. M. Schneider, *Electronic structure, surface morphology, and topologically protected surface states of Sb_2Te_3 thin films grown on Si(111)*, J. Appl. Phys. **113**, 053706 (2013).

[75] G. Zhang, H. Qin, J. Teng, J. Guo, Q. Guo, X. Dai, Z. Fang, and K. Wu, *Quintuple-layer epitaxy of thin films of topological insulator Bi_2Se_3*, Appl. Phys. Lett. **95**, 053114 (2009).

[76] A. Richardella, A. Kandala, J. S. Lee, and N. Samarth, *Characterizing the structure of topological insulator thin films*, APL Materials **3**, 083303 (2015).

[77] M. Lanius, J. Kampmeier, C. Weyrich, S. Kölling, M. Schall, P. Schüffelgen, E. Neumann, M. Luysberg, G. Mussler, P. M. Könraad, T. Schäpers, and D. Grützmacher, *P-N Junctions in Ultrathin Topological Insulator Sb_2Te_3/Bi_2Te_3 Heterostructures Grown by Molecular Beam Epitaxy*, Cryst. Growth Des. **16**, 2057 (2016).

[78] C. Weyrich, M. Drögeler, J. Kampmeier, M. Eschbach, G. Mussler, T. Merzenich, T. Stoica, I. E. Batov, J. Schubert, L. Plucinski, B. Beschoten, C. M. Schneider, C. Stampfer, D. Grützmacher, and T. Schäpers, *Growth, characterization, and transport properties of ternary $(Bi_{1-x}Sb_x)_2Te_3$ topological insulator layers*, J. Phys. Cond. Matt. **28**, 495501 (2016).

[79] J. Kellner, M. Eschbach, J. Kampmeier, M. Lanius, E. Młyńczak, G. Mussler, B. Holländer, L. Plucinski, M. Liebmann, D. Grützmacher, C. M. Schneider, and M. Morgenstern, *Tuning the Dirac point to the Fermi level in the ternary topological insulator* $(Bi_{1-x}Sb_x)_2Te_3$, Appl. Phys. Lett. **107**, 251603 (2015).

[80] M. Eschbach, E. Młyńczak, J. Kellner, J. Kampmeier, M. Lanius, E. Neumann, C. Weyrich, M. Gehlmann, P. Gospodarivc, S. Döring, G. Mussler, N. Demarina, M. Luysberg, G. Bihlmayer, T. Schäpers, L. Plucinski, S. Blügel, M. Morgenstern, C. M. Schneider, and D. Grützmacher, *Realization of a vertical topological p-n junction in epitaxial* Sb_2Te_3/Bi_2Te_3 *heterostructures*, Nature Comm. **6**, 9816 (2015).

[81] L. Plucinski, G. Mussler, J. Krumrain, A. Herdt, S. Suga, D. Grützmacher, and C. M. Schneider, *Robust surface electronic properties of topological insulators:* Bi_2Te_3 *films grown by molecular beam epitaxy*, Appl. Phys. Lett. **98**, 222503 (2011).

[82] A. Herdt, L. Plucinski, G. Bihlmayer, G. Mussler, S. Döring, J. Krumrain, D. Grützmacher, S. Blügel, and C. M. Schneider, *Spin-polarization limit in* Bi_2Te_3 *Dirac cone studied by angle- and spin-resolved photoemission experiments and ab initio calculations*, Phys. Rev. B **87**, 035127 (2013).

[83] L. Fu, *Hexagonal Warping Effects in the Surface States of the Topological Insulator* Bi_2Te_3, Phys. Rev. Lett. **103**, 266801 (2009).

[84] J. Zhang, C.-Z. Chang, Z. Zhang, J. Wen, X. Feng, K. Li, M. Liu, K. He, L. Wang, X. Chen, Q.-K. Xue, X. Ma, and Y. Wang, *Band structure engineering in* $(Bi_{1-x}Sb_x)_2Te_3$ *ternary topological insulators*, Nature Comm. **2**, 574 (2011).

[85] C. R. Dean, A. F. Young, I. Meric, C. Lee, L. Wang, S. Sorgenfrei, K. Watanabe, T. Taniguchi, P. Kim, K. L. Shepard, and J. Hone, *Boron nitride substrates for high-quality graphene electronics*, Nature Nanotech. **5**, 722 (2010).

[86] A. Sandner, T. Preis, C. Schell, P. Giudici, K. Watanabe, T. Taniguchi, D. Weiss, and J. Eroms, *Ballistic Transport in Graphene Antidot Lattices*, Nano Letters **15**, 8402 (2015).

[87] K. Renk, *Basics of Laser Physics* (Springer, Berlin Heidelberg, 2012).

[88] J. Faist, F. Capasso, D. L. Sivco, C. Sirtori, A. L. Hutchinson, and A. Y. Cho, *Quantum Cascade Laser*, Science **264**, 553 (1994).

[89] J. Duan, N. Tang, X. He, Y. Yan, S. Zhang, X. Qin, X. Wang, X. Yang, F. Xu, Y. Chen, W. Ge, and B. Shen, *Identification of Helicity-Dependent Photocurrents from Topological Surface States in Bi_2Se_3 Gated by Ionic Liquid*, Scient. Rep. **4**, 4889 (2014).

[90] C. Kastl, C. Karnetzky, H. Karl, and A. W. Holleitner, *Ultrafast helicity control of surface currents in topological insulators with near-unity fidelity*, Nature Comm. **6**, 7617 (2015).

[91] K. N. Okada, N. Ogawa, R. Yoshimi, A. Tsukazaki, K. S. Takahashi, M. Kawasaki, and Y. Tokura, *Enhanced photogalvanic current in topological insulators via Fermi energy tuning*, Phys. Rev. B **93**, 081403 (2016).

[92] K.-M. Dantscher, D. A. Kozlov, M. T. Scherr, S. Gebert, J. Bärenfänger, M. V. Durnev, S. A. Tarasenko, V. V. Bel'kov, N. N. Mikhailov, S. A. Dvoretsky, Z. D. Kvon, J. Ziegler, D. Weiss, and S. D. Ganichev, *Photogalvanic probing of helical edge channels in two-dimensional HgTe topological insulators*, Phys. Rev. B **95**, 201103 (2017).

[93] L. Magarill and M. Entin, *Circular Photogalvanic Effect Caused by the Transitions between Edge and 2D States in a 2D Topological Insulator*, JETP Lett. **104**, 771 (2016).

[94] J. Karch, C. Drexler, P. Olbrich, M. Fehrenbacher, M. Hirmer, M. M. Glazov, S. A. Tarasenko, E. L. Ivchenko, B. Birkner, J. Eroms, D. Weiss, R. Yakimova, S. Lara-Avila, S. Kubatkin, M. Ostler, T. Seyller, and S. D. Ganichev, *Terahertz Radiation Driven Chiral Edge Currents in Graphene*, Phys. Rev. Lett. **107**, 276601 (2011).

[95] D. A. Abanin, P. A. Lee, and L. S. Levitov, *Charge and spin transport at the quantum Hall edge of graphene*, Solid State Comm. **143**, 77 (2007).

[96] Y. Pan, Q.-Z. Wang, A. L. Yeats, T. Pillsbury, T. C. Flanagan, A. Richardella, H. Zhang, D. D. Awschalom, C.-X. Liu, and N. Samarth, *Helicity dependent photocurrent in electrically gated $(Bi_{1-x}Sb_x)_2Te_3$ thin films*, Nature Comm. **8**, 1037 (2017).

[97] K.-M. Dantscher, D. A. Kozlov, P. Olbrich, C. Zoth, P. Faltermeier, M. Lindner, G. V. Budkin, S. A. Tarasenko, V. V. Bel'kov, Z. D. Kvon, N. N. Mikhailov, S. A. Dvoretsky, D. Weiss, B. Jenichen, and S. D. Ganichev, *Cyclotron-resonance-assisted photocurrents in surface states of a three-dimensional topological insulator based on a strained high-mobility HgTe film*, Phys. Rev. B **92**, 165314 (2015).

[98] M. Orlita, I. Crassee, C. Faugeras, A. B. Kuzmenko, F. Fromm, M. Ostler, T. Seyller, G. Martinez, M. Polini, and M. Potemski, *Classical to quantum crossover of the cyclotron resonance in graphene: a study of the strength of intraband absorption*, New Jour. Phys. **14**, 095008 (2012).

Acknowledgements

Finally, I would like to thank everyone who helped me in one way or another to reach this point.

My biggest thanks go to Sergey. Not only did you give me the fantastic opportunity to do my dissertation, you also encouraged me when I needed it and gave me confidence. You have manage to create a great working atmosphere that allows discussions, questions and also enough space for development. I am deeply grateful for the last few years in your group.

For the enlightening discussions my thank goes to Sergey Tarasenko, Vasily Bel'kov, Lenoid Golub, and Yakov Terent'ev from the Ioffe Institue St. Petersburg. Thank you all for taking the time for answering my questions. Representing all other group members my thank goes to Gregor Mussler, Martin Lanius, Lukaz Plucinsk and Markus Eschbach from the Forschungszentrum Jülich for the Bi_2Te_3- and Sb_2Te_3-based 3D TI samples, the ARPES measurements and for the fantastic collaboration. For high mobility graphene samples, I'd like to thank Jonathan Eroms and Andreas Sandner, for GaSb/InAs samples Sven Höfling and Georg Knebl from the Technical University Würzburg, and Werner Wegschneider from the ETH Zürich. For sharing her knowledge on the GaSb/InAs samples with me I'd like to thank Suanne Müller from the ETH Zürich. For his support at the FELBE my thank goes to Stephan Winnerl from the Helmholtz Zentrum Dresden. I'd like to thank Dmitry Khokhlov and Alexandra Galeeva from the Lomonosov Moscow State University, and Vadim Shalygin from the Polytechnic University St. Petersburg for the cooperation and the great time we spend in the lab together.

For the technical and scientific support in our labs, I'd like to thank Peter Olbrich, Sergey Danilov and our technicians Toni Humbs and Christian Schneider. Representing all secretaries, my thank goes to Claudia Moser for her administrative help, that made my life so much easier.

Thank you Tobi, Kathrin and Philipp for the fantastic years, your valuable discussions, and fun we had on road trips, in wine cellars or on other cultural occasions. For the great time my thanks also go to Stefan, Max, Susi and Sebastian, to all alumni, especially my bachelor and master students Johanna, Stefan, Tanja, Yashawi and Erwin, and to our regular visiting guests, particularly Dima and Vasily.

For proofreading this work and their critical comments, I would like to thank Vasily, Felix and Tobi.

Last, a special thank goes to my family, to my mum for always finding the right words to cheer me up, your courage and warmness, to my dad for your unlimited help, to my sister for your energy and dynamism, and to my granny for your open-mindedness. You all are my source of inspiration for what one can achieve and for everything I do. My boyfriend Philipp is most important to me. Thank you for accepting me as I am, tolerating my moods, especially in the last couple of months, and for your patience. Also, I am deeply thankful for your alert and careful proofreading.